

**Development of Novel Microwave and Millimetre-wave
Sensors for Liquid Characterisation**

Evans Silavwe

Submitted in accordance with the requirements for the degree of
Doctor of Philosophy

The University of Leeds
School of Electrical and Electronic Engineering

July, 2017

Declaration and Authorisation

The candidate confirms that the work submitted is his own, except where work which has formed part of jointly-authored publications has been included. The contribution of the candidate and the other authors to this work has been explicitly indicated below. The candidate confirms that appropriate credit has been given within the thesis where reference has been made to the work of others.

The work presented in this thesis is co-authored with Dr. Nutapong Somjit and Professor Ian Robertson. The candidate is responsible for the work presented in Chapter 3, 4 and 5. The design in chapter 5 was done together with Mr. Nonchanutt Chudpooti, who was a visiting researcher from Thailand. The free space material characterisation in chapter 5 was done by Mr Binbin Hong, while Viktor Doychinov assisted with some of the simulations during the modelling stages of the work in Chapter 5. The candidate did all the analysis in Chapter 5.

This copy has been supplied on the understanding that it is copyright material and that no quotation from the thesis may be published without proper acknowledgement.

Acknowledgements

I would like to thank Professor Ian Robertson for accepting to be my main supervisor for this project and offering valuable insight throughout the research work , especially during the formative period of the work. Special gratitude goes to Dr. Nutapong Somjit, my second supervisor, who went far and beyond in making himself available for consultations, discussions and correction. It was a pleasure to work with you both, I can only say I have learnt a lot that will come in handy in my future engagements as a result.

I would also like to thank other researchers in Professor Robertson's team that I have had the pleasure to work with and share information and skills. These include Razak, Sunday, Lukui, Binbin, Isibor and in the recent past, Viktor. I appreciated some of the discussions we had and the invaluable knowledge shared. I am also indebted to the greater group of the Institute of Microwave and Photonics staff for the support offered throughout and the willingness to help when asked. Special mention goes to Mr. Roland Clarke for ever being available and ready to help, as well as Dr. Paul Steenson for offering to help at the time when the research work was at cross roads.

I furthermore would like to acknowledge and thank the Commonwealth Scholarship Commission for the financial support.

I lastly would like to thank my wife (Hilda), my son (Lukundo) and daughter (Suwila) for ever being available to support and make the research burden lighter by showing me love and care.

Abstract

This research investigates the characterisation of liquids using primarily substrate integrated waveguides and extending this to other interesting conventional transmission lines. Focus is drawn to liquid mixture quantification, which is significant in the distinction of the quantity of one biological or chemical liquid from another. This work identified and confirmed that microwave resonance methods are best suited to perform mixture quantification due to their high sensing accuracy and inherent single point detection. The tracking of the resonant frequency change with either the corresponding return loss or insertion loss (depending on the type of resonant structure) gives a good solution in this regard. On the other hand, it was affirmed that transmission line methods are best suited for general broadband characterisation of a particular liquid. Three major outputs were achieved in this research work, namely: (i) In-SIW millimetre wave sensor; (ii) SIW slot antenna microlitre sensor and (iii) Sub-terahertz CSRR sensor for solid dielectric characterisation. Using the SIW slot antenna sensor, microlitre liquid volumes of $7 \mu\text{l}$ were characterised and binary mixtures quantified with an overall accuracy of better than 3 % when compared with results from a commercial sensor. The In-SIW millimetre wave sensor showed proof of concept through simulation results of the characterisation of $15 \mu\text{l}$ liquid volume results when compared to 100 ml liquid volume measurement done using the Keysight dielectric probe. The sub-terahertz CSRR sensor was used to characterise solid dielectrics using its multifunctionality capability of performing both resonant measurements and transmission line measurements.

Table of Contents

Declaration and Authorisation	ii
Acknowledgements	iii
Abstract	iv
List of Tables	viii
List of Figures	ix
Chapter 1 Introduction.....	1
1.1 Electromagnetic fields and materials	1
1. 1.2 Thesis objectives.....	7
1.2.1 Overall thesis objective.....	7
1.2.2 Research goals	8
1.2.3 Research merit.....	8
2. 1.3 Thesis outline	10
Chapter 2 Microwave Characterisation Methods for Materials	12
2.1 Open-ended coaxial probe method	14
2.1.1 Open-ended coaxial probe models.....	16
2.1.2.1 Capacitive model.....	16
2.1.2.2 Antenna or radiation model.....	20
2.1.2.3 Rational function model	21
2.1.2.4 Virtual line model.....	23
2.2 Waveguide transmission and reflection method	25
2.2.1 Working principle of the transmission and reflection method.....	26
2.2.2 Nicholson-Ross-Weir method.....	30
2.2.3 De-embedding and reference plane transformation.....	32
2.2.4 Air gaps correction	35
2.3 Resonant method.....	37
2.3.1 Resonant perturbation method	37
2.3.2 Resonance sensing using dielectric resonators	40
2. 2.4 Free space method	43
2.5 Criteria for choosing appropriate technique for material characterisation.....	45
2.6 Summary.....	46
Chapter 3 In-Waveguide SIW Sensor	48
3.1 Introduction	48
3.2 Sensor design	49

3.2.1 Analysis of the permittivity of the fluid.....	54
3.2.2 Keysight dielectric probe kit.....	60
3.2.2.1 Performance probe.....	61
3.2.2.2 High temperature probe.....	62
3.2.2.3 Slim form probe.....	63
3.2.3 Dielectric probe measurement results.....	65
3.2.3.1 Measurements done with Probe immersed at 25mm and 50mm.....	66
3.3 Simulation results.....	67
3.3.1 Deionised water simulation results.....	68
3.4 Comparison of In-SIW sensor results with dielectric probe kit measurement results.....	70
3.5 Summary.....	73
Chapter 4 Microfluidic-Integrated SIW Lab-on-Substrate Sensor for Microlitre Liquid Characterisation.....	75
4.1 Introduction.....	75
4.2 Working principle and sensor design.....	78
4.3 Model analysis.....	84
4.4 Measurement results.....	91
4.4.1 Measurement setup, sensor calibration and standard measurement.....	91
4.4.2 Quantification measurement of liquid mixture.....	93
4.4.3 Relative permittivity measurement.....	95
4.4.4 Sensor sensitivity.....	97
4.5 Summary.....	99
Chapter 5 Sub-millimetre Wave Sensor for Dielectric Material Characterisation.....	100
5.1 Introduction.....	100
5.2 Sensor design and fabrication.....	102
5.3 Complex permittivity extraction model.....	107
5.3.1 Resonant method material permittivity extraction.....	107
5.3.2 Transmission method material permittivity extraction.....	112
5.3.2.1 Keysight free-space material characterization measurement setup.....	114
5.4 Measurement results.....	116
5.4.1 Resonant method results.....	116
5.4.2 Resonance Technique-Tuning Capability.....	120

5.4.3 Transmission method results	121
5.5 Summary.....	123
Chapter 6 Conclusion and Future Work	124
6.1 General summary.....	124
6.2 Contributions	126
6.3 Advantages of designs in this thesis.....	127
6.4 Prospects for further research	127
List of Publications	129
List of References	130
Appendix A Matlab codes used in the extraction of material permittivity using the In-SIW transmission line sensor of chapter 3	138
A.1 Main Matlab code for complex permittivity extraction	138
A.1.1 Matlab function called by the code in A.1	139
Appendix B Matlab codes used for the extraction of relative permittivity for the liquid in chapter 4	140
B.1 Main matlab code for permittivity extraction	140
B.1.1 Matlab function called by the code in B.1	141

List of Tables

Table 2.1 Material characterisation methods	13
Table 4.1 Summary of the design parameters	80
Table 4.2 Deionised water-methanol mixture measurement.....	94
Table 4.3 Relative permittivity measurement of methanol/DI-water mixture using SIW slot antenna and the Keysight dielectric probe	96
Table 4.4 Key parameter comparison of measurement of this work and other work	98
Table 5.1 Summary of the design parameters	104
Table 5.2 Calculation of R_1 and R_3 values.....	110
Table 5.3 Calculation of R_2 and R_4 values.....	110
Table 5.4 Complex permittivity results – Resonant method.....	119
Table 5.5 Complex permittivity with sliding short tuned at 10.78 mm from port 2	121

List of Figures

Figure 1.1 Dielectric response of water in the presence of an external electric field.....	5
Figure 1.2 Dielectric mechanisms response	6
Figure 2.1 Open ended dielectric probe for permittivity measurements.	15
Figure 2.2 Capacitive model equivalent circuit	16
Figure 2.3 Antenna model equivalent circuit.....	20
Figure 2.4 Rational function model.....	22
Figure 2.5 Virtual line model.....	23
Figure 2.6 Typical transmission and reflection method.....	27
Figure 2.7 Schematic of the transmission and reflection method.....	27
Figure 2.8 Schematic for liquid characterisation in a transmission line	33
Figure 2.9 Rectangular waveguide showing gap left by SUT.....	36
Figure 2.10 Rectangular waveguide cavity with feed through the broad wall	38
Figure 2.11 Rectangular waveguide cavity with liquid channel fed through the side walls	39
Figure 2.12 A quarter wavelength resonator built into central conductor of a coplanar waveguide to create a sensor	42
Figure 2.13 Illustration of free space method for material characterisation.....	43
Figure 2.14 Encapsulation illustration for free space liquid characterisation.....	44
Figure 3.1 Top layer of the 3-layer structure.....	50
Figure 3.2 Liquid holder layer (middle layer)	51
Figure 3.3 Bottom layer of the structure	51
Figure 3.4 Assembly of the structure, middle and bottom layer are cofired together	52
Figure 3.5 Network analyser illustration of the full setup.....	53
Figure 3.6 Cross section of the entire assembly or line assembly	56
Figure 3.7 Cross section of the through standard.....	56
Figure 3.8 (a) Performance Probe (b) Calibration short [37].....	62
Figure 3.9 High Temperature Probe Kit [37].....	63
Figure 3.10 Three Slim Form Probes with the short standard and other accessories [37].	64

Figure 3.11 ECal module in use with Slim Form Probe also showing the flexible cable connecting to the Network Analyser [37]	65
Figure 3.12 Deionised water relative permittivity measurement results at 25mm and 50mm probe depth	66
Figure 3.13 Loss factor measurement results at 25mm and 50mm probe depth immersed in deionised water	66
Figure 3.14 Deionised water loss tangent measurement at 25mm and 50mm probe depth	67
Figure 3.15 S_{11} and S_{21} plots for through standard	68
Figure 3.16 S_{11} and S_{21} Simulation results for Deionised water using the in-waveguide sensor	69
Figure 3.17 Extracted real and imaginary part of the complex permittivity of deionised water	70
Figure 3.18 Relative permittivity result for Deionised water when measured using the Keysight dielectric probe and LTCC in-waveguide sensor simulation result	71
Figure 3.19 Loss factor of Deionised water when measured using the Keysight dielectric probe and the LTCC In-waveguide simulation result	72
Figure 3.20 Relative permittivity of Methanol when measured using the Keysight dielectric probe and the simulation result of the LTCC in-waveguide sensor	72
Figure 3.21 Loss factor of Methanol when measured using the Keysight dielectric probe and the simulation result when using the designed in-waveguide sensor	73
Figure 4.1 3D drawing of SIW waveguide integrated with a single slot antenna and microfluidic subsystem	80
Figure 4.2 Precisely cut Microfluidic subsystem layers aligned at the edges	82
Figure 4.3 Fabricated prototype, before (top) and after (bottom) mounting the microfluidic subsystem	83
Figure 4.4 SIW Sensor radiating area equivalent 2-D circuit	86
Figure 4.5 Equivalent model of the feed network	89
Figure 4.6 S_{11} plot for simulated and measured Air, Methanol and DI water samples	92
Figure 4.7 Measured S_{11} plot for Methanol and DI water mixtures	93
Figure 4.8 Measured resonant frequency against Methanol fractional volume	95
Figure 4.9 Sensor sensitivity simulations	97
Figure 5.1 (a) CSRR schematic in the broad-wall of a rectangular waveguide (b) CSRR equivalent lumped element model	103

Figure 5.2 Fabricated prototype, showing assembled structure and the components of the structure	105
Figure 5.3 Contacting sliding short	106
Figure 5.4 Measurement setup (a) with sensor working as a resonant sensor (b) resonant setup with MUT (c) transmission method setup	107
Figure 5.5 3D plot of resonant frequency against relative permittivity with loss tangent kept constant through values 0, 0.0005, 0.005 and 0.01	110
Figure 5.6 3D plot of S11 against loss tangent with relative permittivity kept constant through the values 1, 2, 3, 4, and 5.	111
Figure 5.7 3D fitted curve to S21 measurement standard	113
Figure 5.8 Keysight free space material characterisation setup.....	115
Figure 5.9 Measured and simulated S11 response for Air, PTFE, PMMA and HDPE samples.	117
Figure 5.10 Measured S11 with the sliding short inserted at 10.78 mm from port 2	120
Figure 5.11 S21 plot for measured Air, PTFE and PMMA samples.	121
Figure 5.12 Transmission method extracted relative permittivity for PTFE and PMMA	122

Chapter 1

Introduction

1.1 Electromagnetic fields and materials

Electromagnetic material characterisation to a great degree deals with the interactions of electromagnetic fields with dielectric materials. Dielectrics include a vast number of materials from biological tissues/fluids, substrate material in integrated circuits, food substances, building materials and agricultural products. From the knowledge of dielectric properties, it is possible to infer how a particular material stores or dissipates energy in the presence of electromagnetic fields and equally how the material would affect the electromagnetic field. Once the measured dielectric properties of a particular material have been established, they form what is termed as the material electromagnetic response within a particular measurement frequency band. Any changes in the dielectric properties from the expected response in the presence of an electromagnetic field, tends to indicate that the material's dielectric properties are in a different state and hence gives reason for further investigation. This kind of analysis has been used to diagnose malignant tissues in humans [1].

Some dielectric material measurement approaches have found significant application in the characterisation of biological materials because they offer quick and accurate results without alteration of the sample as opposed to most optical and chemical detection techniques [2]. Because of their non-

destructive nature and increasing compactness, some of the electromagnetic techniques have been used to characterise samples of varying volumes from microlitre down to picolitre and have proved not to be wasteful by using small samples and environmentally friendly by providing an ease way of sample disposal.

The measurement techniques of dielectric properties of any material depend on the nature of the dielectric material, the frequency of interest and the accuracy requirements. The nature of the material impacts how the electromagnetic energy propagates in that material. The electromagnetic characteristics of any material will in principle determine the velocity of propagation of the electromagnetic energy, which is given by:

$$v = \frac{1}{\sqrt{\mu\epsilon}} \quad (1.1)$$

where μ is the magnetic permeability and ϵ is the electric permittivity of the material under test (MUT).

For free space propagation this becomes:

$$v = \frac{1}{\sqrt{\mu_0\epsilon_0}} \quad (1.2)$$

where μ_0 and ϵ_0 are the permeability and permittivity of free space respectively. Most liquids are nonmagnetic and have permeability equal to that of free space ($\mu = \mu_0$). The relative permeability of the liquids measured in this work was taken as 1 since they are nonmagnetic materials.

It is well known that a material's dielectric properties are obtained from the measured complex relative permittivity, which has no units as it is a relative quantity. Relative complex permittivity is expressed as

$$\epsilon_r^* = \frac{\epsilon}{\epsilon_0} = \epsilon'_r - j\epsilon''_r \quad (1.3)$$

The real part of the relative complex permittivity, ϵ'_r , gives a measure of how much energy is stored in the material from an oscillating external electric field or a measure of the charge displacement (the real part of complex permittivity is in most cases referred to only as the relative permittivity). The imaginary part, ϵ''_r , on the other hand, gives a measure of how much energy is dissipated by the material upon application of an oscillating external electric field and is usually called the loss factor.

The material interaction with electromagnetic fields is sufficiently described by Maxwell's equations. Equations (1.4) and (1.5) below show Maxwell's constitutive equations [3]:

$$\mathbf{D} = \epsilon \mathbf{E} = (\epsilon'_r - j\epsilon''_r)\epsilon_0 \mathbf{E} \quad (1.4)$$

$$\mathbf{B} = \mu \mathbf{H} = (\mu'_r - \mu''_r)\mu_0 \mathbf{H} \quad (1.5)$$

where \mathbf{E} is the electric field strength vector, \mathbf{D} is the electric displacement vector, \mathbf{H} is the magnetic field strength vector and \mathbf{B} is the magnetic flux density.

Another important term is the loss tangent, which is a term used to describe the relative loss of a material and is defined as the ratio of the energy lost per cycle to the energy stored per cycle.

$$\tan \delta = \frac{\epsilon''_r}{\epsilon'_r} = \frac{\text{energy lost per cycle}}{\text{energy stored per cycle}} = \frac{1}{Q_d} \quad (1.6)$$

where Q_d is defined as the quality factor of the material.

In a similar way the complex relative permeability is defined by the following expression:

$$\mu_r^* = \frac{\mu}{\mu_0} = \mu'_r - j\mu''_r \quad (1.7)$$

The real part of the relative complex permeability, μ'_r , gives a measure of the magnetic energy stored while the imaginary part, μ''_r , gives a measure of how much magnetic energy is lost in a magnetic material in the presence of an external magnetic field.

In most cases therefore, materials are sufficiently described in terms of their complex permittivity, complex permeability and the loss tangent.

Materials tend to have different dielectric properties due to the different measure by which the atoms, molecules, free charges and defects are repositioned in the presence of an external electromagnetic field. This repositioning brings about electric polarisation which is defined through three mechanisms [4]:

- *Dipole or Orientation Polarisation*

This is pronounced in materials that possess permanent dipoles that are randomly oriented in the absence of an applied field. When subjected to an electric field, the dipoles tend to align with the applied field. Materials that exhibit this behaviour are called polar materials and water is such a material.

- *Ionic or Molecular Polarisation*

This form of polarisation is found in materials that have positive and negative ions that tend to displace themselves when an electric field is applied, for example Sodium Chloride.

- *Electronic Polarisation*

This type of polarisation takes place when an applied electric field displaces the electric cloud centre of an atom relative to the centre of the nucleus and takes place in most materials.

Fig. 1.1 shows the dielectric response of deionised (DI) water in the presence of an external electric field.

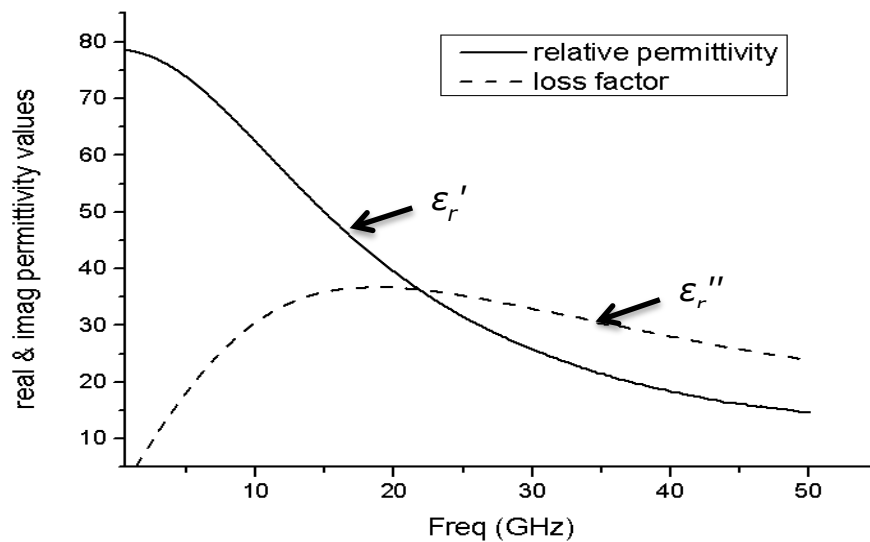


Figure 1.1 Dielectric response of water in the presence of an external electric field

Below 22 GHz, the dipole polarisation mechanism and the ionic conduction mechanism are dominant as the water molecules respond to the external electric field. The relative permittivity, ϵ_r' , decreases with increased frequency due to the phase lag between the dipole alignment and the electric field. At the same time the loss factor, ϵ_r'' , increases with frequency due to the rotational friction of the water molecules. The time required for the displaced molecules (dipoles) to be oriented in an electric field is called the relaxation time, τ . The behaviour illustrated in Fig. 1.1 is observed in polar liquids.

In solids, the electronic and atomic polarisation are the dominant mechanism that influence the dielectric properties. Fig. 1.2 shows all the mentioned mechanisms and their frequency response.

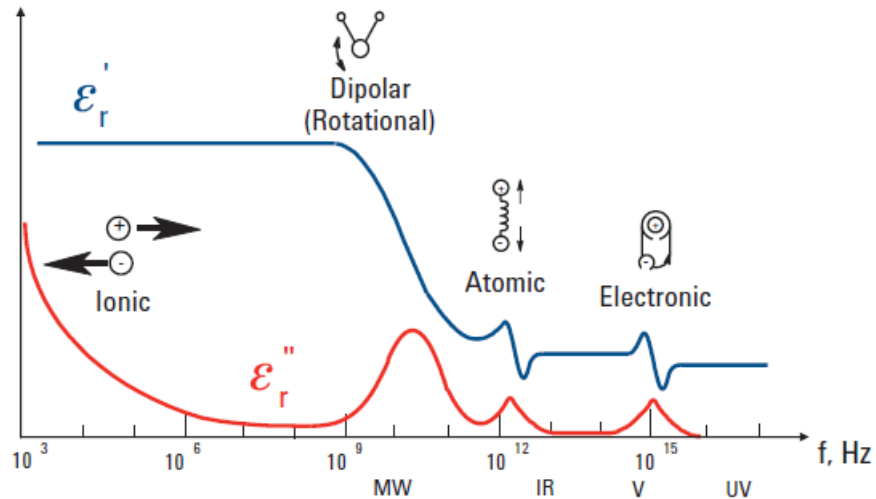


Figure 1.2 Dielectric mechanisms response [4]

Dielectric measurements have found tremendous use in the evaluation of biological tissues for cancer research [1], building materials [5], negative index materials [6], electromagnetic shielding solutions and propagation of wireless signals.

In [1], in-vivo investigations were conducted using an insertion-type planar probe to measure the permittivity characteristics of cancerous tissue and normal tissue. These were compared with ex-vivo measurements. The technique having used a probe exploited the reflection coefficients over a broad frequency band range from 0.5 to 30 GHz and used the values to obtain the complex permittivity of the tissue. The main objective was to investigate the suitability of the insertion-type planar probe for cancer detection.

In [5] the potential of microwave technique for online monitoring and evaluation of biofilms in pipelines was investigated. The pipeline was taken as a circular waveguide, while the whole setup used a transmitting and

receiving coaxial-line transducer that was connected to a vector network analyser. The measurements were done in the 45-47GHz frequency range with the permittivity of the biofilm-contained area expressed as a function of the resonance frequency after the resonance condition was established in the waveguide. The whole design then focused on the change of the resonance frequency shift as the biofilm layer length and thickness grew.

In [6], the dielectric properties of biological materials were investigated using an artificial metamaterial structure (MMS) with negative permittivity and permeability over the open waveguide sensor so that the sensing properties of the waveguide sensor could be increased. This used the classical waveguide sensor operating in the X-band. The waveguide sensor was designed for the measurement of dielectric properties for biological tissues in the microwave frequency band.

1.2 Thesis objectives

The objectives of this thesis are summarised through the following subsections to help align the ideas and for coherence.

1.2.1 Overall thesis objective

This thesis aims to develop an accurate and sensitive liquid mixture quantification and characterisation method for biological solutions. In doing this, broadband as well as resonance techniques are considered to qualitatively develop the most appropriate technique. Reference liquids are used for modelling in the absence of actual biological liquids with perspectives of biological liquid measurements constantly considered throughout the project.

1.2.2 Research goals

This research was driven by the following goals:

1. Achieve 95 % accuracy in liquid quantification using micro-litre volume samples while extracting the permittivity properties of the liquid at the same time.
2. Develop adequate guiding design criterion for achieving a highly sensitive sensor for water rich liquids.
3. Determine what kind of measurement system is appropriate at millimetre and sub-terahertz frequencies for characterising and quantification of polar liquids.
4. Compare the developed method to current available methods and conclude how the proposed method adds to the available knowledge.

1.2.3 Research merit

To enhance available spectroscopic methods for biological liquids by looking at possible high accuracy microwave quantification and characterisation methods using polar liquids.

Liquid material characterisation at millimetre and sub-terahertz-wave frequencies ensures that results obtained are largely due to the material under test without the influence of liquid ionic conduction effects, prevalent at lower frequencies. For example in the determination of microwave dielectric signatures of tumorous B-lymphoma cells [7], better accuracy was obtained for measurements done between 20 GHz to 40 GHz than those done below 20 GHz. Due to the challenge that arises from characterisation of liquids at such high frequencies, traditional microwave methods have not broadly covered this region and most available solutions are encumbered

with several limitations. This research therefore looks at creating novel methods that will enhance accuracy while using micro-litre liquid volumes. This was seen as a driving merit of this research even though some of the work ended up being done below the millimetre-wave band. To arrive at the appropriate method, both transmission and resonant methods were considered. Ultimately higher accuracy was achieved with the resonant method for material characterisation. This work established that in designing a resonant method for liquid material characterisation, the following enhances the sensitivity of the sensor:

- Create the sensing structure such that the liquid under test does not interrupt or interact with the main propagating field but only with the near-field or the evanescent field. This ensures that the signal monitored at the output port (which will also be the input port for a one-port structure) remains interpretable through all measurement.
- Ensure that the resonant structure is optimised for the defined bounds of operation of the sensor. This ensures that even in the worst case scenario, the sensitivity of the sensor remains reliable.

It is already established that a good knowledge of dielectric properties of liquids at microwave and millimetre-wave frequencies can be used to realise their composition. This has been shown to be important as it impacts on many applications pertaining to the human body as well other industrial and chemical processes. Even though a lot of work has been done in the characterisation of liquids, there continues to be a need for development of compact and cheap sensors that can easily be integrated with other devices. It has been observed that as the frequency increases from microwave into the millimetre-wave band and beyond, structures for liquid characterisation

tend to become compact which makes them ideal for integration into microfluidic platforms which are necessary for lab-on-chip implementations.

This work, in contrast to the conventional concept, focuses on development of novel liquid sensors which do not require the liquid to disturb the electromagnetic field in the main signal path. This non-conventional concept is based on transmission line structures that sense the liquid and determine the liquid's dielectric properties through the interactions of the radiated field from the device and the liquid. This has potential to extend the usage to very high frequency as opposed to methods that place the liquid in the main field path, since high attenuation tends to take place with such methods as the wavelength reduces to millimetre and sub-millimetre range. The resultant miniaturised sensors allow for accurate sensing of microlitre and picolitre sample quantities which is desired in medical investigation of living matter.

This work also builds on the existing knowledge base in extracting material properties from the measured scattering parameters.

1.3 Thesis outline

The thesis is arranged as follows: Chapter 1 introduces the topic and then gives the thesis objectives and novelty contributions. In Chapter 2, various microwave material characterisation methods are discussed, ending with the criteria for choosing the appropriate method. Chapter 3 focuses on the designed millimetre-wave In-Substrate Integrated Waveguide (SIW) sensor for broadband characterisation of liquids. This operates between 33 – 50 GHz. In Chapter 4, a Lab-On-Chip SIW slot antenna based sensor designed for microlitre liquid characterisation is presented. This operates at about 10 GHz and was meant as a prototype for millimetre-wave characterisation of

liquids. Chapter 5 focuses on the developed sub-terahertz sensor for solid substrate material characterisation. This essentially was laying the foundation for liquid characterisation in the sub-terahertz range. Chapter 6 concludes and gives future perspectives.

Chapter 2

Microwave Characterisation Methods for Materials

This chapter reviews the common material characterisation methods and how they are implemented with respect to the measured microwave responses (mostly scattering parameters).

Material characterisation usually involves the measurement of complex permittivity as a function of frequency at a particular temperature, although at times complex permittivity has been obtained as a function of temperature at a fixed frequency. The knowledge of dielectric properties so obtained offers an opportunity to know the low frequency conduction mechanism, interfacial polarisation and molecular dynamics [8]. Many techniques for material characterisation have been developed; these include the cavity resonator method, the transmission line method, the free space method and the open-ended coaxial probes. Resonator methods are accurate but not broadband and best suitable for low-loss materials, whereas transmission line techniques are broadband but mostly suitable for medium to high-loss materials, giving reasonable accuracy [9]. Open-ended coaxial probes, waveguides and cavity resonators can all be used to measure the properties for liquids. The free space method finds more usage in adverse conditions, like high temperature situations and large flat solid materials. Each method has its merits and application where they are best suited. Whether a method is destructive or non-destructive also determines where the method finds application. All these methods are impacted by the nature of the materials that they measure. For example, even though

resonant methods offer higher accuracy when compared to other alternatives, when used to measure high loss materials they lose sensitivity and possess some challenges. On the other hand transmission line methods suffer from metal losses that impact measurements [9].

Table 2.1 shows the common methods, the materials they measure, the s-parameters required to get the dielectric properties and the dielectric properties measured as a result.

Table 2.1 Material characterisation methods

Measurement Method	Materials that can be measured	Parameters required	Reported Dielectric properties measured
Transmission/Reflection method	Solids, Liquids	S_{11} , S_{21}	ϵ^*_r , μ^*_r
Open-ended coaxial probe method	Liquids, semi-solids	S_{11}	ϵ^*_r
Resonant cavity method	Rod shaped solid materials, liquids	Resonant Frequency, Q-factor	ϵ^*_r , μ^*_r
Free space method	High temperature material, large flat solids, gas, hot liquids	S_{11} , S_{21}	ϵ^*_r , μ^*_r

In solid dielectric measurements, air gaps are undesired as they have the tendency of causing the electric field to suffer from depolarisation, especially when it is perpendicular to the material under test. In transmission line

methods that use electrodes, air gaps have a tendency of creating a series capacitance which contributes to the overall systematic errors [9].

The next sections look at each of the characterisation methods and their application in liquid characterisation.

2.1 Open-ended coaxial probe method

The open ended coaxial probe method for material characterisation relates the impedance at the coaxial line end to the complex permittivity of the material under test [10]. In order for repeatability and accuracy to be assured, the sample must be homogenous with sufficient volume that offers an electrically infinite size. Therefore, for open ended coaxial probes used to measure liquids, sufficient liquid volume must exist between the probe tip and the end of the liquid container to additionally ensure that any signal reflection is all due to the liquid and not the container. Equally there must be sufficient liquid volume between the sides of the probe and the liquid container to ensure that reflections from fringing fields, as shown in Fig. 2.1, are only reflected back by the sample under test and not the container. Fig. 2.1 shows the typical parameters of an open ended coaxial line probe. As shown, when the traversing TEM field goes through the sample under test, reflections at the probe tip ensue. The measurement of the magnitude and phase of the reflections enable the extraction of the permittivity properties of the sample under test (SUT) as will be shown in the following sub-sections.

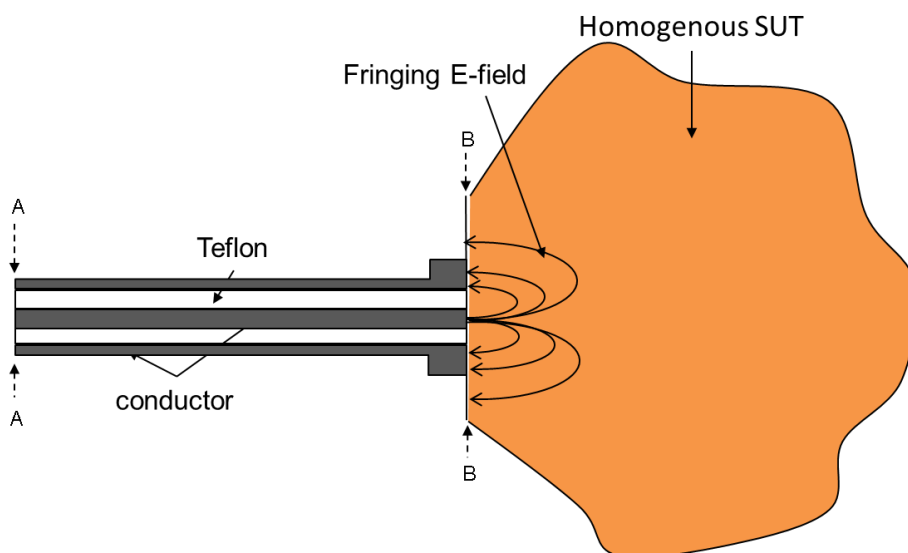


Figure 2.1 Open ended dielectric probe for permittivity measurements.

When using the open-ended coaxial probe method, there are three main sources of error, namely, cable stability, air gaps in the case of solids or air bubbles in the case of liquids and sample thickness. It's always advised that cable stability is ensured before measurements can be made and equally in between measurement and calibration, the cable is required to be in a firmly fixed position or errors will occur. Air gaps when measuring solids should be avoided by all means as they create a transition of capacitance and hence cause a significant source of error. This is true also for air bubbles on the tip of the probe. Measurements should therefore only be taken in the absence of these. The significance of the thickness of the sample arises from the fact that the desired measurement of the reflection coefficient should only be as a result of the material under test and not the effects coming from the sample holder or fixture. This requires that the sample appears infinitely thick to the probe. The sample thickness or depth must therefore be at least

twice the equivalent penetration depth of the electromagnetic wave. This in essence will ensure that the reflected waves at the far SUT-fixture interface, should the field reach there, will be attenuated by approximately -35 dB by the time the reflected signal reaches the probe end [11]. This effectively eliminates the effect of such reflected signals on the measurement.

2.1.1 Open-ended coaxial probe models

Four open-ended coaxial probe models have been developed, namely, capacitive model, antenna model, virtual line model and rational function model [12]. In each of the four models the probe is terminated by a semi-infinite homogenous sample.

2.1.2.1 Capacitive model

This model, as can be inferred from the name, exploits the changes in the coaxial line capacitance as it is exposed to the sample under test, with the line capacitance when radiating in air acting as the reference. Fig. 2.2 shows the equivalent circuit model [13].

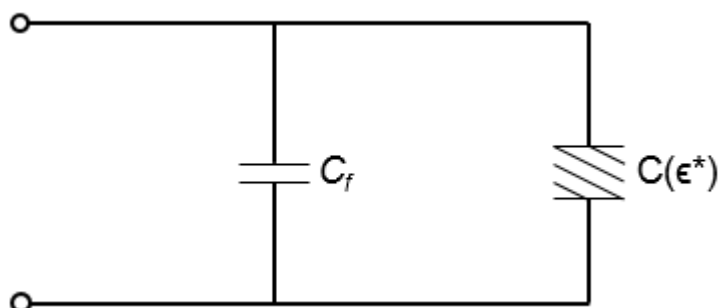


Figure 2.2 Capacitive model equivalent circuit

In Fig. 2.2, the sensor is depicted by two main elements, namely a lossy capacitor, $C(\epsilon^*)$, and a capacitor, C_f , that considers the effects of the fringing field in the Teflon (the dielectric for the coaxial line). The lossy capacitor on

the other hand relates to the capacitance measured when terminating in free space as shown in (2.1) [12].

$$C(\epsilon_r^*) = \epsilon_r^* C_0 \quad (2.1)$$

where C_0 is the capacitance when the coaxial line is terminating in air.

For the equivalent circuit to be valid, the dimensions of the line must be small when compared to the wavelength of the line at that frequency. This ensures that the open end of the line does not radiate and in turn confines the energy in the fringing region or reactive near field of the line. As the frequency increases, the evanescent modes increase and this leads to an equivalent increase in the value of C_0 . Therefore when the evanescent modes are considered, $C_0 + A\omega^2$ should be used in the place of C_0 , where A is a constant dependant on the line dimensions.

The input reflection coefficient, Γ^* , at the discontinuity plane is calculated as shown in (2.2).

$$\Gamma^* = \Gamma^{j\Phi} = \frac{1 - j\omega Z_0 (C(\epsilon^*) + C_f)}{1 + j\omega Z_0 (C(\epsilon^*) + C_f)} \quad (2.2)$$

where,

ω is the angular frequency and

Z_0 is the characteristic impedance of the coaxial line probe.

From (2.2),

$$\epsilon^* = \frac{1 - \Gamma^*}{j\omega Z_0 C_0 (1 + \Gamma^*)} - \frac{C_f}{C_0} \quad (2.3)$$

Eqn. (2.3) has two unknowns, C_f and C_0 , that are determined by using a calibration standard, deionised water in most cases, with known dielectric properties. Eqns. (2.4) and (2.5) give the equations that are used to determine these two unknowns:

$$C_0 = \frac{(1-|\Gamma_{std}^*|^2)}{\omega Z_0(1+2|\Gamma_{std}^*|\cos(\Phi_{std})+|\Gamma_{std}^*|^2)\epsilon''_{std}} \quad (2.4)$$

$$C_f = \frac{-2|\Gamma_{std}^*|\sin(\Phi_{std})}{\omega Z_0(1+2|\Gamma_{std}^*|\cos(\Phi_{std})+|\Gamma_{std}^*|^2)} - \epsilon'_{std}C_0 \quad (2.5)$$

where,

Γ_{std}^* is the complex reflection coefficient of the calibration standard referenced at the probe end,

Φ_{std} is the phase of the reflection coefficient,

ϵ'_{std} is the real part of the complex permittivity of the calibration standard and

ϵ''_{std} is the imaginary part of the complex permittivity of the calibration standard.

Looking at Fig. 2.1, it is noticeable that the measured input reflection coefficient will be referenced at the A – A plane, however it is desired that this measurement be referenced at the B – B plane which is the discontinuity plane . The reference plane is moved from A – A to B – B by using the relationship in (2.6).

$$\Gamma_{B-B}^* = \Gamma_{A-A}^* e^{j2\theta} \quad (2.6)$$

where 2θ considers the signal's round trip in the coaxial line given by

$$\Phi_{A-A} = \Phi_{B-B} - 2\theta \quad (2.7)$$

where

Φ_{B-B} is the phase of the reflection coefficient measured at the B – B plane and Φ_{A-A} is the phase of the reflection coefficient measured at the A – A plane.

The phase of the reflection coefficient at the B – B plane is determined by measuring the reflection coefficient when the coaxial probe is terminating in air. From [14] and using the internal radius of the conductor in the coaxial probe (a) and the radius of the external conductor (b), $C_f + C_0$ when terminating in air is

$$C_f + C_0 = 2.38\epsilon_0(b - a) \quad (2.8)$$

Using (2.8) in (2.2) gives the value of the reflection coefficient at the B – B plane as

$$\Gamma_0^* = \frac{1 - j2.38\omega Z_0 \epsilon_0 (b - a)}{1 + j2.38\omega Z_0 \epsilon_0 (b - a)} \quad (2.9)$$

From (2.9) the phase gives the value of Φ_{B-B}

$$\Phi_{B-B} = \Phi_0 = -2.38\omega Z_0 \epsilon_0 (b - a) \quad (2.10)$$

Using (2.10), (2.7) can be solved as

$$2\theta = -2.38\omega Z_0 \epsilon_0 (b - a) - \Phi_{A-A} \quad (2.11)$$

where Φ_{A-A} is obtained from the phase of the measured reflection coefficient at the A – A plane using a network analyser.

2.1.2.2 Antenna or radiation model

In the antenna or radiation model, the permittivity of the sample in contact with an open end coaxial line is calculated from the measured input admittance referred to the line discontinuity plane (where the line interfaces with the liquid) [12]. Fig. 2.3 shows the equivalent circuit of the antenna model.

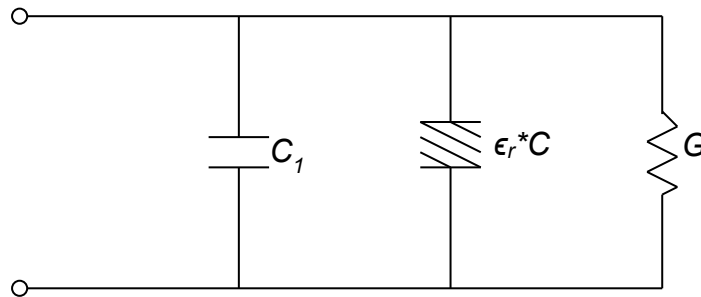


Figure 2.3 Antenna model equivalent circuit

The admittance at the discontinuity plane of the coaxial line is represented by a capacitance and conductance (C_2 and G in Fig. 2.3) [15]. The normalised admittance at the coaxial open end is given in (2.12).

$$\frac{Y}{Y_0} = j\omega C_1 Z_0 + j\omega Z_0 C_2(\omega, \epsilon_r^*) + Z_0 G(\omega, \epsilon_r^*) \quad (2.12)$$

Where, Z_0 is the characteristic impedance of the coaxial line, C_1 is the capacitance due to the fringing fields within the line, C_2 is the capacitance due to the fringing fields outside the line, ϵ_r^* is the complex permittivity of the

material under test, G is the radiation conductance and ω is the angular frequency.

In this model, with the coaxial line inserted in a lossy liquid, the radiation into the liquid mimics an antenna. The admittance for an antenna in a lossy medium can be approximated by [15]

$$Y(\omega, \epsilon_r^*) = \sqrt{\epsilon_r^*} Y(\sqrt{\epsilon_r^*} \omega, \epsilon_0) \quad (2.13)$$

Hence (2.13) becomes

$$\frac{Y}{Y_0} = j\omega C_1 Z_0 + j\omega \epsilon_r^* C_2 Z_0 + \epsilon_r^{*\frac{5}{2}} G Z_0 \quad (2.14)$$

Which is of a similar form to

$$\frac{Y}{Y_0} = K_1 + K_2 \epsilon_r^* + K_3 \epsilon_r^{*\frac{5}{2}} \quad (2.15)$$

When the complex values of K_1 , K_2 and K_3 are known, the permittivity of the sample under test can be calculated from the measured normalised admittance. Three standards are commonly used to determine the complex values K_1 , K_2 and K_3 , namely deionised water, methanol and air [12].

2.1.2.3 Rational function model

The rational function model uses an aperture admittance model for the 50- Ω open-ended coaxial line in contact with an homogenous dielectric. The developed model is based on a rational function of a full-wave moment method [16]. The formulation of the model includes radiation effects, the near field region energy storage impact and the evanescent mode effects [12]. Fig. 2.4 shows the rational function model.



Figure 2.4 Rational function model

The admittance of the rational model is given by (2.16) as shown in [12].

$$\frac{Y}{Y_0} = \frac{\sum_{n=1}^4 \sum_{p=1}^8 \alpha_{np} (\sqrt{\epsilon_r^*})^p (j\omega a)^n}{1 + \sum_{m=1}^4 \sum_{q=0}^8 \beta_{mq} (\sqrt{\epsilon_r^*})^q (j\omega a)^m} \quad (2.16)$$

Where α_{np} and β_{mq} are the model coefficients, ϵ^* is the complex permittivity of the dielectric under test, a is the radius of the inner conductor of the coaxial line, while Y is the admittance at the coaxial line end and Y_0 is the characteristic admittance of the coaxial line. The model is valid for the complex permittivity of the sample under test in the following range, $1 \leq \epsilon_r' \leq 80$ and $0 \leq \epsilon_r'' \leq 80$, with the frequency range between 1 and 20 GHz.

In [16] to calculate the complex permittivity of the sample under test, the following functions were defined:

$$b_p = \sum_{m=1}^4 \alpha_{mp} (j\omega a)^m \quad p = 1, 2, \dots, 8; \quad (2.17)$$

$$b_0 = 0; \quad (2.18)$$

$$c_q = \sum_{m=1}^4 \beta_{mq} (j\omega a)^m \quad q = 1, 2, \dots, 8; \quad (2.19)$$

$$c_0 = 1 + \sum_{m=1}^4 \beta_{m0} (j\omega a)^m \quad (2.20)$$

By substituting (2.17) – (2.20) in (2.17) and with Y considered as the measured admittance, the unknown permittivity is the square root of the root of (2.21).

$$\sum_{i=0}^8 (b_i - Y_{ci}) \sqrt{\epsilon^*}^i = 0 \quad (2.21)$$

It is necessary to observe that the correct root must have $\epsilon_r' > 1$ and $\epsilon_r'' > 0$ to be meaningful.

2.1.2.4 Virtual line model

In the virtual line model, the complex permittivity of the sample under test (SUT) is calculated by relating the reflection coefficient of an open-ended coaxial line, in contact with an SUT, with the effective transmission-line proposed [17]. The effective transmission line models the fringing electric field in the SUT and the open end of the coaxial line as shown in the equivalent circuit model shown in Fig. 2.5.

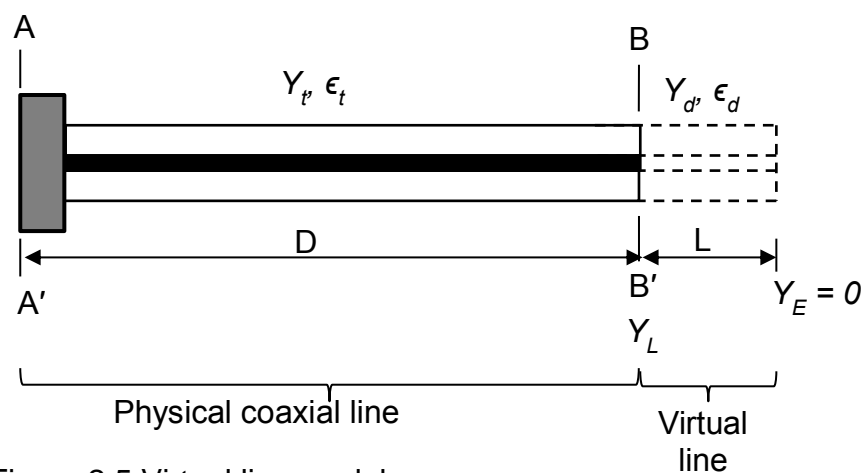


Figure 2.5 Virtual line model

In Fig. 2.5, plane $B-B'$ is the impedance reference plane, while plane $A-A'$ is the measurement plane. The admittance at plane $B-B'$ is calculated

using the characteristic admittance of the virtual line (Y_d) and the terminating admittance at the end of the virtual line (Y_E) as shown in (2.22).

$$Y_L = Y_d \frac{Y_E + jY_d \tan(\beta_d L)}{Y_d + jY_E \tan(\beta_d L)} \quad (2.22)$$

where Y_L is the admittance at the input of the virtual line, L is the length of the virtual line and β_d is the propagation constant in the SUT.

If the radiation loss is neglected, the terminating impedance at the end of the virtual line is a reflected impedance. In this case the terminating impedance will be an open circuit and the admittance $Y_E = 0$, effectively reducing (2.23) to

$$Y_L = jY_d \tan(\beta_d L) \quad (2.23)$$

Y_d is calculated by considering the virtual line as a coaxial line with external diameter b , internal diameter a and dielectric permittivity ϵ_d (which is the SUT permittivity), as shown in (2.24).

$$Y_d = \frac{\sqrt{\epsilon_d}}{60 \ln(b/a)} \quad (2.24)$$

The virtual line input admittance, Y_L , can also be calculated from the measured admittance at plane A – A' as shown in (2.25).

$$Y_L = \frac{1 - \Gamma_m e^{2j\beta_t D}}{1 + \Gamma_m e^{2j\beta_t D}} Y_t \quad (2.25)$$

where Y_t is the characteristic admittance of the physical coaxial line, β_t is the propagation constant in the physical coaxial line and Γ_m is the reflection coefficient at plane A – A'.

The permittivity of the SUT is calculated by substituting (2.24) and (2.25) in (2.23) to get (2.26) as

$$\epsilon_d = \frac{-jc\sqrt{\epsilon_t}}{2\pi fL} \cdot \frac{1-\Gamma_m e^{2j\beta_t D}}{1+\Gamma_m e^{2j\beta_t D}} \left(\frac{2\pi fL\sqrt{\epsilon_d}}{c} \right) \quad (2.26)$$

Where c is the speed of light in free space and f is the measured frequency, other parameters are as defined before.

The two unknown variables that are necessary to calculate the permittivity of the SUT, D and L , are determined through measurements of two standards with known dielectric properties. In [17], air and deionised water were used and this was achieved by substituting (2.24) in (2.25). Using an iterative procedure with the measured reflection coefficient, values for D and L were obtained.

2.2 Waveguide transmission and reflection method

In the waveguide transmission and reflection method, the material under test is placed in a section of waveguide or coaxial line and then the scattering parameters are measured at the input and output ports of the transmission line using a VNA. Two scattering parameters, the S_{11} and S_{21} , are used for onward post processing to obtain the full material characterisation. If the SUT is a solid, prior SUT machining is required so that it fits perfectly in the waveguide and does not leave any gaps. Similarly, liquids are required to

completely fill the waveguide section that is designated to hold them and not leave any space before the measurement is taken.

2.2.1 Working principle of the transmission and reflection method

In this method, the required equipment in most cases are a transmission line (could be a waveguide or coaxial line) and a vector network analyser. Prior to performing any measurements, the limits for the SUT thickness needs to be established, as this informs what scattering parameters to use between the forward scattering parameter, S_{21} , and the reverse scattering parameter, S_{11} . The transmission method finds application for measurements that have the transmission parameter, S_{21} , not below -30 dB, otherwise the reflection method is preferred.

Fig. 2.6 shows a typical setup of the transmission and reflection method.

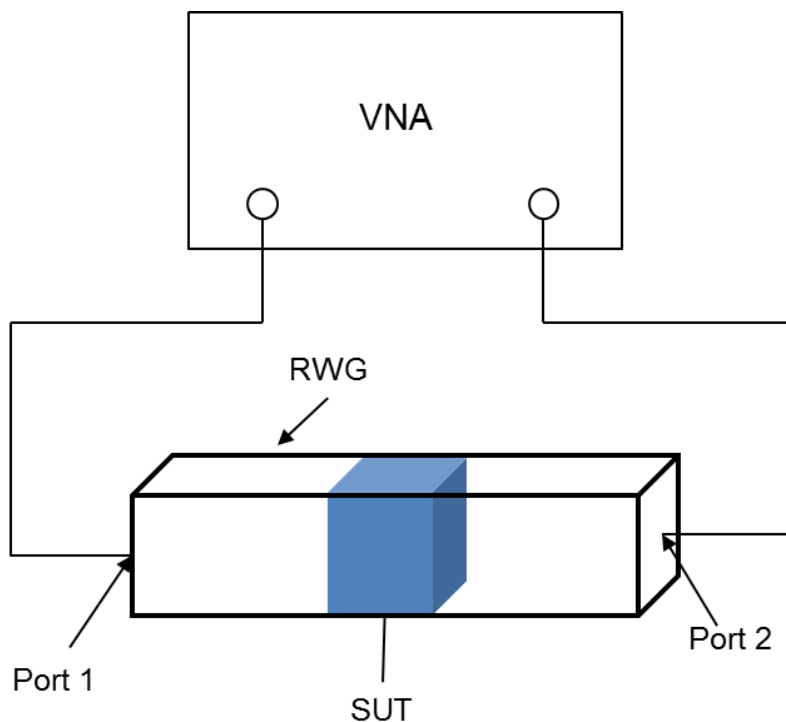


Figure 2.6 Typical transmission and reflection method

The developed equations from the measurement in Fig. 2.6 relate the scattering parameters to the permittivity and permeability of the material. Fig. 2.6 can be simplified by the schematic given in Fig. 2.7.

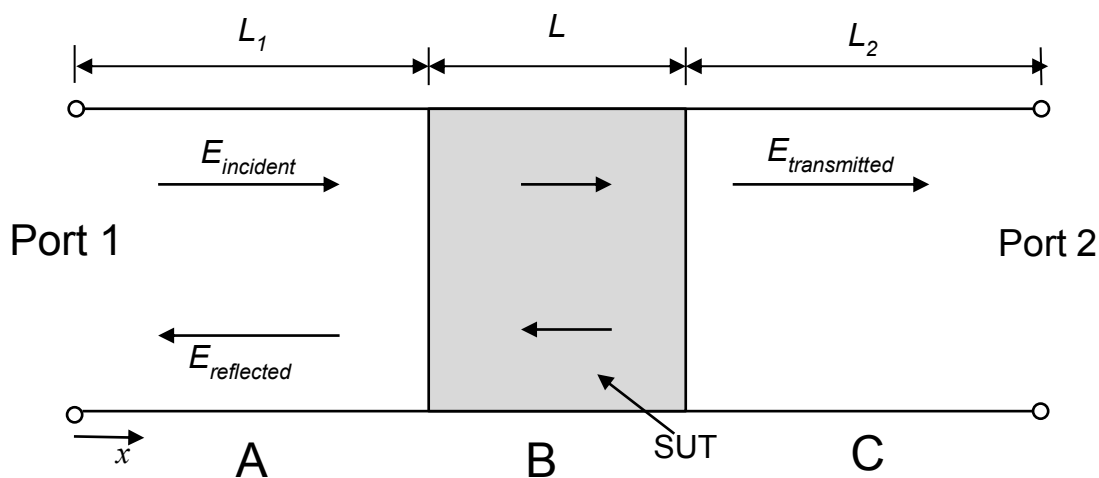


Figure 2.7 Schematic of the transmission and reflection method

The developed system of equations is usually overdetermined with variables comprising complex permittivity, the two reference planes positions and the

sample length. The equations are developed from an analysis of the electric field at the SUT interfaces. If electric fields E_A , E_B and E_C are considered in the regions A, B and C of Fig. 2.7 for either TEM mode in a coaxial line or TE₁₀ mode in a waveguide, the following spatial distribution of the electric field for an incident field normalised to 1 can be written as [18]:

$$E_A = e^{(-\gamma_0 x)} + C_1 e^{(\gamma_0 x)} \quad (2.27)$$

$$E_B = C_2 e^{(-\gamma x)} + C_3 e^{(\gamma x)} \quad (2.28)$$

$$E_C = C_4 e^{(-\gamma_0 x)} \quad (2.29)$$

Where

$$\gamma_0 = j \sqrt{\left(\frac{\omega}{c}\right)^2 - \left(\frac{2\pi}{\lambda_c}\right)^2} \quad (2.30)$$

$$\gamma = j \sqrt{\left(\frac{\omega}{c}\right)^2 \cdot \mu_r^* \epsilon_r^* - \left(\frac{2\pi}{\lambda_c}\right)^2} \quad (2.31)$$

c is the speed of light in vacuum, γ_0 and γ are the propagation constants in vacuum and SUT respectively, ϵ_r^* and μ_r^* are the relative permittivity and permeability respectively, ω is the angular frequency and λ_c is the cutoff wavelength. It is worth noting that in region C there is no backward wave since the transmission line is matched at port 2, this is reflected in (2.29).

Using Maxwell's equations to calculate the tangential components representing the boundary condition on the electric field with only a radial component, gives:

$$E_A(x = L_1) = E_B(x = L_1) \quad (2.32)$$

$$E_B(x = L_1 + L) = E_C(x = L_1 + L) \quad (2.33)$$

where L_1 and L are the distances from port 1 to the SUT interface and the SUT length respectively as defined in Fig. 2.7.

By solving (2.27) – (2.29) using the boundary conditions in (2.32) and (2.33), the equations for the scattering parameters can be obtained as shown in (2.34) and (2.38).

$$S_{11} = R_1^2 \left[\frac{\Gamma(1-T^2)}{1-\Gamma^2 T^2} \right] \quad (2.34)$$

$$S_{22} = R_2^2 \left[\frac{\Gamma(1-T^2)}{1-\Gamma^2 T^2} \right] \quad (2.35)$$

$$S_{21} = R_1 R_2 \left[\frac{T(1-\Gamma^2)}{1-\Gamma^2 T^2} \right] \quad (2.36)$$

Where

$$R_1 = e^{(-\gamma_0 L_1)} \quad (2.37)$$

$$R_2 = e^{(-\gamma_0 L_2)} \quad (2.38)$$

R_1 and R_2 are the reference plane transformation expressions while L_2 is the distance from port 2 to the SUT as defined in Fig. 2.7. T is the transmission coefficient in the SUT that is defined as

$$T = e^{(-\gamma L)} \quad (2.39)$$

When there is a sample in the transmission line, the transmission scattering parameter becomes

$$S_{21} = R_1 R_2 e^{(-\gamma_0 L)} \quad (2.40)$$

The unknowns from (2.34) – (2.40) are ϵ_r' , ϵ_r'' , R_1 , and R_2 , whereas L is in most cases known. These equations are sufficient for the complex permittivity of the SUT to be calculated as Nicholson-Ross-Weir showed [19, 20], the detail of which is given in the next section.

2.2.2 Nicholson-Ross-Weir method

Nicholson, Ross and Weir [19, 20] are credited with having developed the working principle of the transmission and reflection method that has evolved over time with the advancement of measurement methods. Nicholson-Ross [19], however, only considered solid materials in their measurements based on the model in Fig. 2.7.

Using the sums and differences of the scattering equations in (2.34) – (2.36), Nicholson-Ross, established the following relationship,

$$K = \frac{S_{11}^2 - S_{21}^2 + 1}{2S_{11}} \quad (2.41)$$

They further defined the reflection and transmission coefficient as

$$\Gamma = K \pm \sqrt{K^2 - 1} \quad (2.42)$$

$$T = \frac{S_{11} + S_{21} - \Gamma}{1 - (S_{11} + S_{21})\Gamma} \quad (2.43)$$

From basic principles however the reflection coefficient is defined as

$$\Gamma = \frac{Z - Z_0}{Z + Z_0} = \frac{\sqrt{\mu_r^*/\epsilon_r^*} - 1}{\sqrt{\mu_r^*/\epsilon_r^*} + 1} \quad (2.44)$$

From (2.44)

$$\frac{\mu_r^*}{\epsilon_r^*} = \left(\frac{1 + \Gamma}{1 - \Gamma}\right)^2 = c_1 \quad (2.45)$$

Also the transmission coefficient between the sample surfaces is

$$T = \exp(-j\omega\sqrt{\mu\epsilon}l_s) = \exp[-(\omega/c)\sqrt{\mu_r^*\epsilon_r^*}l_s] \quad (2.46)$$

From (2.46)

$$\mu_r^*\epsilon_r^* = -\left\{\frac{c}{\omega l_s} \ln\left(\frac{1}{T}\right)\right\}^2 = c_2 \quad (2.47)$$

Using (2.45) and (2.47), Nicolson-Ross were able to explicitly obtain the permittivity and permeability of materials as follows:

$$\mu_r^* = \sqrt{c_1 c_2} \quad (2.48)$$

$$\epsilon_r^* = \sqrt{\frac{c_2}{c_1}} \quad (2.49)$$

In [18] as well as [21] it was shown that the Nicolson-Ross method is divergent at integer multiples of one-half wavelength in the sample for low-loss materials. At these frequencies the $|S_{11}|$ parameter becomes very small and hence makes the equations give unreliable values as $|S_{11}|$ tends

towards zero. In an effort to overcome this problem others have tended to shorten the sample length. This however has been shown to lower measurement sensitivity. Furthermore, the solution for equation (2.45) and (2.47) was found not to be trivial as a phase ambiguity needed to be resolved at each calculated frequency and measured group delay [18].

What was proposed, which has widely been accepted and adopted, is that the combination of the equations (2.34) – (2.46) get solved iteratively. This results in solutions that are stable over the frequency band of measurement. This line of reasoning has therefore been followed in this work.

Since in this project liquids were predominantly measured, a sample holder was introduced. In the case of the transmission and reflection method, this required that plugs to stop the liquid from flowing out are introduced at either side of the liquid plane. This therefore introduces a further requirement to shift the measurement plane, not only from the input and output ports but to include beyond the plugs holding the SUT in place. The procedure for this is explained in the next subsection that looks at the de-embedding and reference plane transformation.

2.2.3 De-embedding and reference plane transformation

In Section 2.2.2, it was shown that after the inclusion of the sample holder when measuring liquids, it becomes evident that the equations derived by Nicolson-Ross cannot be used straight away as the measured S-parameters would this time include the effect of the sample holder. This is overcome by using the de-embedding procedure that ensures that the reference plane is moved all the way to the face of the SUT. Consider the schematic shown in Fig. 2.8, that shows a transmission line being used to characterise a liquid.

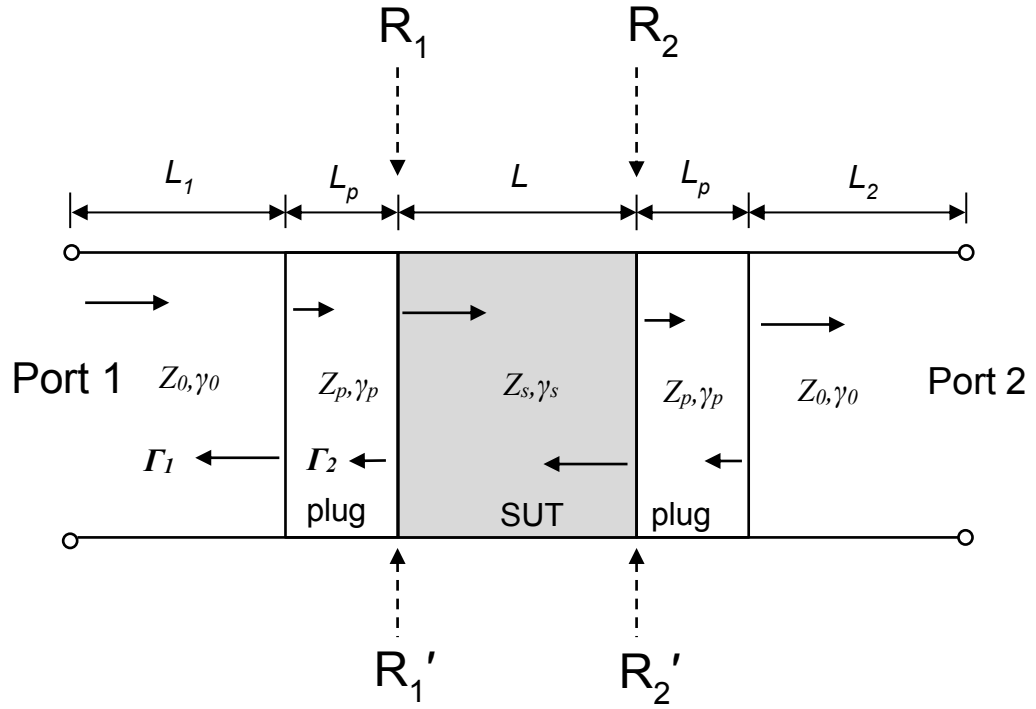


Figure 2.8 Schematic for liquid characterisation in a transmission line

In Fig. 2.8 $R_1 - R_1'$ and $R_2 - R_2'$ are the SUT reference planes at the input and output respectively. Z_0 , γ_0 , Z_p , γ_p , Z_s and γ_s are the impedance and propagation constant of the air filled, plug filled and sample filled sections of the waveguide. The expressions for the total forward and backward scattering parameters for the whole line from (2.34) – (2.36) become [22]

$$S_{21} = \frac{T_s(1-\Gamma_s^2)}{1-\Gamma_s^2 T_s^2} = \frac{4\gamma_s\gamma_0}{(\gamma_s+\gamma_0)^2 e^{\gamma_s L} - (\gamma_s-\gamma_0)^2 e^{-\gamma_s L}} \quad (2.50)$$

$$S_{11} = \frac{\Gamma_s(1-T_s^2)}{1-\Gamma_s^2 T_s^2} = \frac{(\gamma_0-\gamma_s)^2 e^{\gamma_s L} - (\gamma_0+\gamma_s)^2 e^{-\gamma_s L}}{(\gamma_s+\gamma_0)^2 e^{\gamma_s L} - (\gamma_s-\gamma_0)^2 e^{-\gamma_s L}} \quad (2.51)$$

Now, define Γ_1 as the reflection coefficient at the interface between the air section and the plug of the waveguide, Γ_2 as the reflection coefficient between the SUT and the plug as shown in (2.52) and (2.53):

$$\Gamma_1 = \frac{Z_p - Z_0}{Z_p + Z_0} \quad (2.52)$$

$$\Gamma_2 = \frac{Z_s - Z_p}{Z_s + Z_p} \quad (2.53)$$

With the transmission coefficient through the plug and the SUT defined as

$$T_1 = e^{-\gamma_p L_p} \quad (2.54)$$

$$T_2 = e^{-\gamma_s L_s} \quad (2.55)$$

By substituting (2.52) – (2.55) in (2.50) and (2.51), they simplify to:

$$S_{21} = \frac{(1 - \Gamma_1^2 - \Gamma_2^2 + \Gamma_1^2 \Gamma_2^2) T_1^2 T_2^2}{1 + 2\Gamma_1 \Gamma_2 T_1^2 - \Gamma_2^2 T_2^2 - 2\Gamma_1 \Gamma_2 T_1^2 T_2^2 + \Gamma_1^2 \Gamma_2^2 T_1^4 - \Gamma_1^2 T_1^4 T_2^2} \quad (2.56)$$

$$S_{11} = \frac{\Gamma_1 + \Gamma_2 T_1^2 (1 + \Gamma_1^2) + \Gamma_1 \Gamma_2^2 T_1^4 - \Gamma_1 T_2^2 (\Gamma_2^2 + T_1^4) - \Gamma_2 T_1^2 T_2^2 (1 - \Gamma_1^2)}{1 + 2\Gamma_1 \Gamma_2 T_1^2 - \Gamma_2^2 T_2^2 - 2\Gamma_1 \Gamma_2 T_1^2 T_2^2 + \Gamma_1^2 \Gamma_2^2 T_1^4 - \Gamma_1^2 T_1^4 T_2^2} \quad (2.57)$$

The waveguide sections filled with a plug, SUT and another plug can be considered as a cascade assembly, which helps simplify the de-embedding. To proceed, first of all measurements or simulations are done with only one plug inserted in the transmission line. The obtained S-parameters must be corrected to the planes at the interfaces of the plug. Thereafter measurements or simulations are done with the entire assembly complete to get the total S-parameters. Using ABCD parameters and treating the whole assembly as a cascade, the following relationship is developed:

$$[T_S] = [T_p]^{-1} \cdot [T_T] \cdot [T_p]^{-1} \quad (2.58)$$

where,

$[T_p]$ represents the plug ABCD parameters

$[T_s]$ represents the SUT ABCD parameters

$[T_T]$ represents the total ABCD parameters for the whole assembly

From the obtained ABCD matrix of the SUT, the corresponding S-parameters only due to the SUT effect can be calculated as

$$S_{11S} = \left[\frac{A_S + B_S Z_0^{-1} - C_S Z_0 - D_S}{A_S + B_S Z_0^{-1} + C_S Z_0 + D_S} \right] \quad (2.59)$$

$$S_{21S} = \left[\frac{2}{A_S + B_S Z_0^{-1} + C_S Z_0 + D_S} \right] \quad (2.60)$$

$$S_{12S} = \left[\frac{2(A_S D_S - B_S C_S)}{A_S + B_S Z_0^{-1} + C_S Z_0 + D_S} \right] \quad (2.61)$$

$$S_{22S} = \left[\frac{-A_S + B_S Z_0^{-1} - C_S Z_0 + D_S}{A_S + B_S Z_0^{-1} + C_S Z_0 + D_S} \right] \quad (2.62)$$

where Z_0 is the characteristic impedance of the line and A_S , B_S , C_S and D_S are the elements of the SUT ABCD matrix.

After obtaining the S-parameters due only to the liquid, the complex permittivity can then be obtained using similar methods as shown in subsection 2.2.2 as the assembly reduces to Fig. 2.7. The implementation of the transmission method is shown fully in Chapter 3.

2.2.4 Air gaps correction

Air gaps are a major source of errors when measuring solids using the transmission and reflection method, not so much for liquid samples. For liquid samples, the major source of errors in this regard are air bubbles. For the former case, air gaps are particularly of concern when present in the wide side of a rectangular waveguide or near the centre conductor of a coaxial line. This is because these regions have a stronger electric field. The case of a rectangular waveguide with an SUT leaving a gap as shown in Fig. 2.9 is considered.

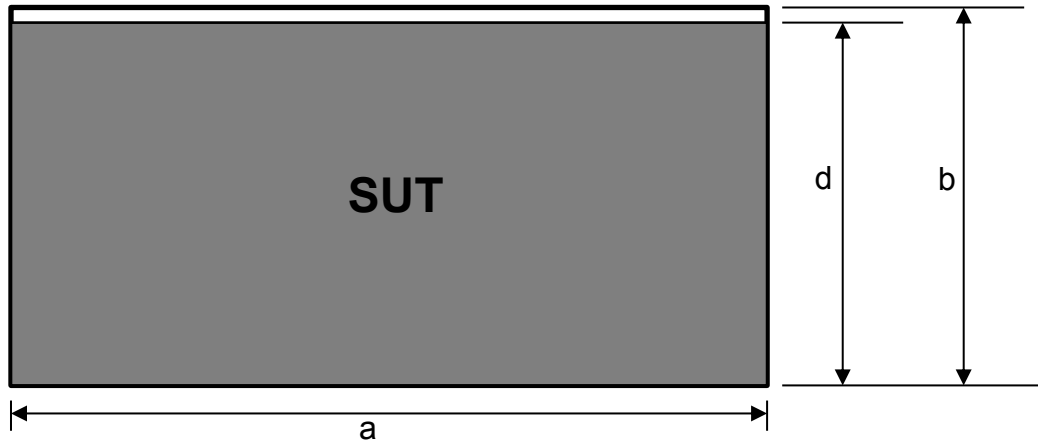


Figure 2.9 Rectangular waveguide showing gap left by SUT

The gap has been analysed by considering it as a layered capacitor [3, 23]. However, due to the fact that the wavelength decreases at higher frequency leading to the domination of multiple scattering, the capacitor model fails. The frequency independent model uses a perturbation theory for cavities [28]. This is developed by considering the difference between the propagation constant for the case without a gap and that with a gap, given by:

$$\gamma_{gap}^2 - \gamma_{no\ gap}^2 = \Delta\gamma^2 = (\epsilon_r' - 1) \left(\frac{\omega}{c}\right)^2 \frac{\int_{gap} \vec{E}_1 \cdot \vec{E}_2 dS}{\int_S |\vec{E}_1|^2 dS} \quad (2.63)$$

Where E_1 and E_2 are the electric field with no air gap and with an air gap present, respectively, and S is the cross sectional area.

By using the boundary condition relationship, (2.63) reduces to:

$$\frac{\Delta\epsilon_r'}{\epsilon_r'} = (\epsilon_r' - 1) \left(\frac{b-d}{b}\right) \quad (2.64)$$

2.3 Resonant method

Resonant methods use either cavities (generally called resonant perturbation method) or a resonator. For liquid measurements using resonant perturbation, a hole is made in the centre of the cavity where the electric field is maximum and hence causing the highest perturbation. For the resonator method, the strongest field region has to be identified, after which the liquid can be inserted across that region but all the while ensuring that the quality factor is not completely damped out and that the resonant mode propagates.

Resonant methods offer the highest accuracy and sensitivity when compared to non-resonant methods. The principle of their operation is that the introduction of an SUT in a specific region of the resonator tends to modify their known response in terms of change in resonant frequency, change in quality factor (Q) and change in the S-parameters. Various methods have been developed that relate these changes to the dielectric properties of introduced SUT. The next subsections give some examples of resonant perturbation and resonator methods.

2.3.1 Resonant perturbation method

In the resonant perturbation method, a cavity is first designed and its response without perturbation characterised in terms of Q factor and resonant frequency. When an SUT is introduced, the perturbation introduced causes the resonant frequency to shift by Δf_0 and a decrease in the unloaded Q -factor Q_u . In [24] a substrate integrated waveguide (SIW) cavity was used to characterise various liquids.

In terms of design, the resonant frequency of the TE_{101} mode of a rectangular cavity is related to its width a and length l (2.65) as

$$f_{101} = \frac{c}{2\pi\sqrt{\epsilon_r'\mu_r'}} \sqrt{\left(\frac{\pi}{a}\right)^2 + \left(\frac{\pi}{l}\right)^2} \quad (2.65)$$

where ϵ_r' and μ_r' are the real part of the permittivity and permeability respectively of the dielectric filling the cavity.

The goal is to critically couple the cavity at the input to the input feed section, which leads to a very high return loss at the resonant frequency and hence making the cavity very sensitive to any changes. This high sensitivity makes it possible to measure very small changes in the SUT.

Fig. 2.10 (a) shows a rectangular waveguide cavity with a liquid channel fed through the broad walls [25], while Fig. 2.11 shows a rectangular waveguide cavity with a liquid channel fed through the side walls [24].

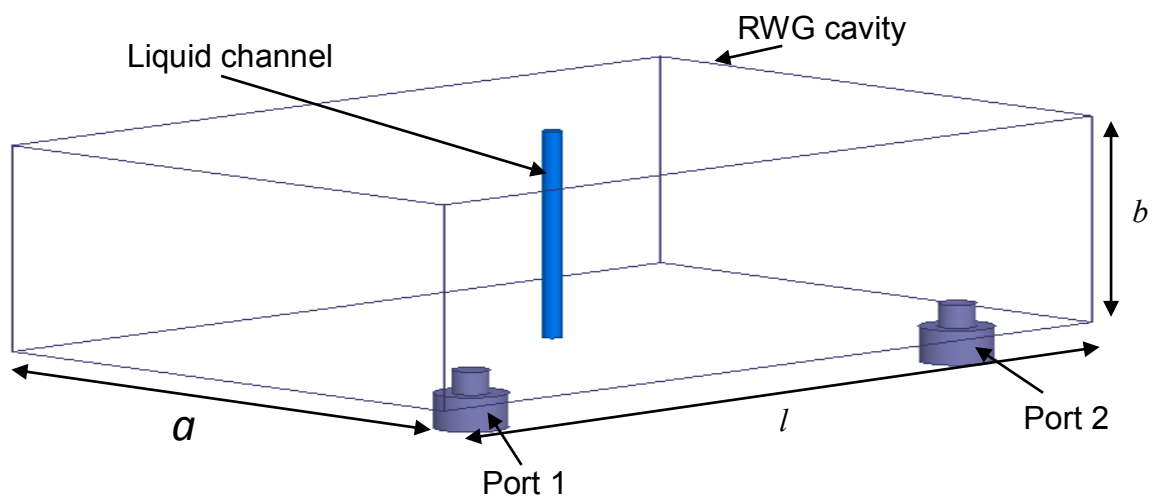


Figure 2.10 Rectangular waveguide cavity with feed through the broad wall

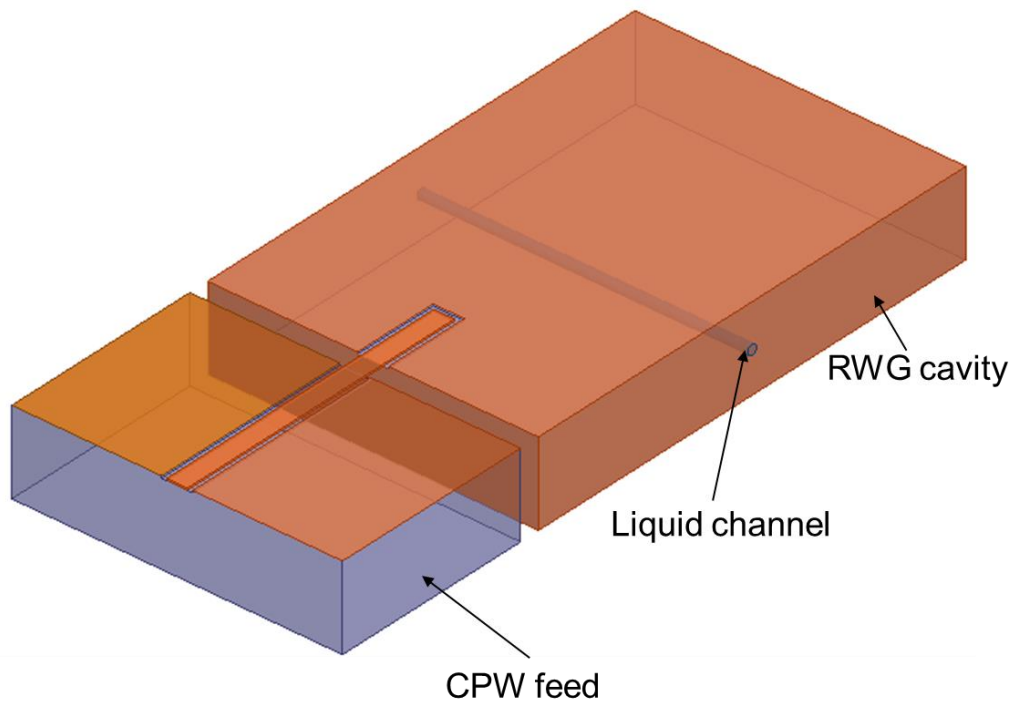


Figure 2.11 Rectangular waveguide cavity with liquid channel fed through the side walls

In both Fig. 2.10 and Fig. 2.11 the liquid is inserted in such a way that it interacts with the electric field at its maximum, which is in the centre of the cavity. Although inserting the liquid through the side walls is less sensitive when compared to inserting through the broad walls, it was preferred in [24] as it gives more mechanical stability since the width of side a is bigger than that of side b .

For the cavity perturbation method, the following equations that relate the dielectric properties of the SUT to the response of the cavity have been defined [24, 26]:

$$\epsilon_r' = \frac{AV_c}{V_s} \left[\frac{f_0 - f_s}{f_s} \right] \quad (2.66)$$

$$\epsilon_r'' = \frac{BV_c}{V_s} \left[\frac{Q_0 - Q_s}{Q_s Q_0} \right] \quad (2.67)$$

where,

ϵ_r' and ϵ_r'' are the dielectric constant and the loss factor respectively.

V_c and V_s are the volume of the cavity and of the sample respectively.

f_0 and f_s are the resonant frequency when the capillary is empty and when its filled with a liquid respectively.

Q_0 and Q_s are the Q factors of the cavity when its empty and when it has a sample.

A and B are constants that depend on the shape of the cavity and the location of the sample.

A and B are obtained through measurement of standards with known dielectric properties analytically. For the cases shown in Fig. 2.10, where a rectangular TE_{101} waveguide cavity has been used with a cylindrical sample inserted through the broad walls, $A = 0.5$ and $B = 0.25$.

The relationship established in (2.66) and (2.67) is that the dielectric constant of the SUT is directly proportional to the change in resonant frequency of the cavity. And similarly that the loss factor of the SUT is direct proportional to the change in the Q factor of the cavity.

2.3.2 Resonance sensing using dielectric resonators

In the dielectric resonator method, the RF part of the design will normally consist of a circuit that is optimised to resonate at a particular designed frequency to meet the desired measurement requirements and a fluidic channel designed to interact with the radiated field at a maximum field location to achieve the highest sensitivity. This extension of the resonance

method has made it possible to measure high loss liquids, whereas the perturbation method has been predominantly used for measuring low loss liquids. This is mostly due to the significant dampening of the quality factor experienced when measuring high loss liquids, which makes the analysis used in the perturbation method difficult to apply.

In [26], the resonant structure was designed using a planar folded quarter-wavelength type resonator that was etched in the central conductor of a coplanar waveguide. The microfluidic channel was then bonded to the top surface of the structure located perpendicular to the central conductor of the coplanar waveguide. The sensing mechanism is centred around the principle that when unfilled the sensor is characterised by the resonant frequency, transmission coefficient and the Q factor. When the microfluidic channel is filled, these parameters shift in value in response to the field interaction with the liquid. It is this shift in the parameters that is used to characterise the SUT properties. The more sensitive the sensor is to the changing conditions and if this is reflected in significant change in the response parameters, the more the likelihood of fully characterising of the SUT increases. On the other hand if the sensor is only significantly sensitive in one parameter, then only one dielectric property of the SUT can be calculated. In cases where quantification of the SUT is the desired goal, characterisation in only one parameter (for example dielectric constant) is sufficient.

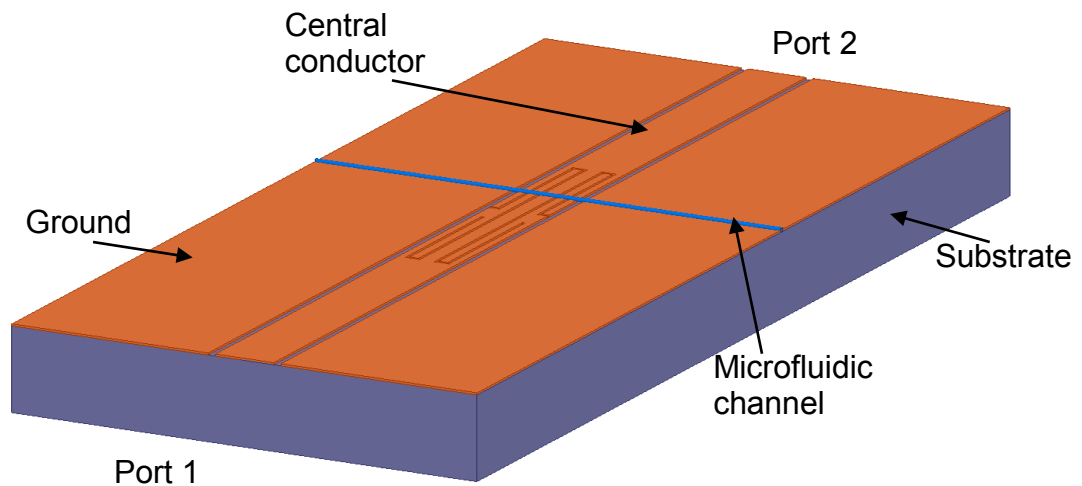


Figure 2.12 A quarter wavelength resonator built into central conductor of a coplanar waveguide to create a sensor

In Fig. 2.12, the dielectric properties of the SUT were extracted from the change in the magnitude of the S_{21} and the resonant frequency. A system of equations is usually created that relates the dielectric properties to the measurement parameters. These equations are then solved iteratively, in most cases using the Newton Raphson method.

The microfluidic channel is designed in an appropriate way that makes the sensing effective. In [26], polydimethylsiloxane (PDMS) was used to make the microfluidic channel. In the case of a microfluidic channel, attention must be paid on how the liquid is to be inserted into the channel and extracted out of the channel. Other considerations are the reusability of the channel after measurement.

Overall, the resonance method offers the highest accuracy and sensitivity although users have to bear in mind that resonant sensors offer a solution at either one frequency or over a narrow band of frequencies. For quantification

of samples, resonant methods have found many applications when compared to transmission and reflection methods.

2. 2.4 Free space method

The free space method, as applied to the characterisation and measurement of dielectric materials properties, is contactless and non-destructive. It has found application in the characterisation of solids, especially those at high temperature where minimal handling is required. There are few reported studies where it has been used to characterise liquids [27], although this usage is rare.

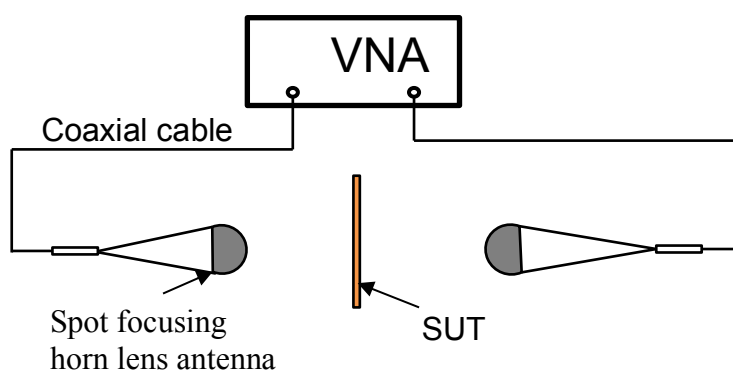


Figure 2.13 Illustration of free space method for material characterisation

In the case of the liquid as the SUT, just like in the transmission and reflection method, the liquid has to be encapsulated into a dielectric with known electrical properties. The sample would then form three sections, namely the dielectric with known properties, then the SUT and the dielectric with known properties as shown in Fig. 2.14.

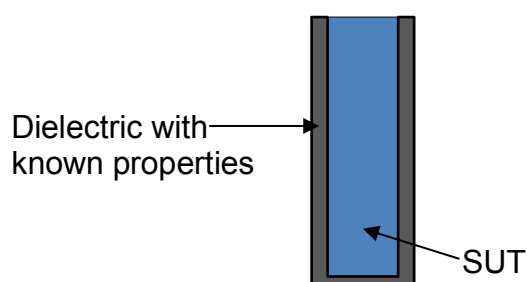


Figure 2.14 Encapsulation illustration for free space liquid characterisation

The dielectric properties of the liquid are then extracted by using a similar method to that given in section 2.2.3. The characteristic impedance of the line Z_0 is in this case replaced by the free-space wave impedance. The operation of the free space method extends from microwave to the millimetre region, offering a wide range of material characterisation.

The free space method suffers from a number of inaccuracies influenced by several factors such as ensuring that the antenna used transmits a plane electromagnetic wave onto a focused area and also ensuring that the wave goes through the SUT with minimal diffraction. These two factors coupled with the need to have a controlled environment around the measurement setup, makes using this method challenging at times.

In terms of calibration the through-reflect-line (TRL) is usually the calibration standard of choice. The initial setup must ensure that the antennas are placed at the start of the far field, that is at $2D^2/\lambda$. Where D is the big diameter of the horn antenna.

The major selling point of this method, as already intimated, is that it offers a purely contactless method for measurement. With all the limitations of accuracy indicated, in some applications the value of the measurement being contactless can be compelling and therefore make this the method of choice. Such applications can be measurement of dangerous chemicals or hot samples as already indicated.

2.5 Criteria for choosing appropriate technique for material characterisation

The change in a material's permittivity as the frequency is increased varies differently between low-loss materials and high-loss materials. For low-loss materials, the permittivity decreases almost linearly with increased frequency from the RF region into the millimetre-wave region. At the same time, the loss tangent increases with increased frequency. The permittivity value decrease in high-loss materials, however, is more rapid with increased frequency with the loss factor increasing rapidly and reaching a relaxation peak before it again decreases.

The aforementioned material characteristics including the materials' spatial dimensions and geometry influence the choice of dielectric measurement technique to use. Materials are categorised as either bulk (like integrated circuit substrates, polymers for packaging, building materials and liquids) or thin (for those on the scale of micrometre or sub-micrometre in one dimension like thin films in integrated circuit processing, coatings and polymer sheets) or nanoscale (which includes nanowires, quantum dots and large molecules). Some important considerations to make when deciding which technique to use are [4]:

- The frequency range of the method chosen,
- The measurement accuracy that is required,
- Whether the material is homogenous or isotropic,
- The material form, i.e. whether it is liquid or solid or powder or sheet,
- The restriction of the sample size,

- Whether the method is destructive or non-destructive,
- Whether the method is contacting or non-contacting,
- The temperature for the measurement,
- The cost of the technique,
- The expected values of permittivity and permeability. This also takes into account whether the material is low-loss or high-loss.

2.6 Summary

It is clear that the microwave characterisation method used depends to a great degree on the type of dielectric material that is to be measured. This is because materials come with differences in form, physical phase, size and shape [28]. Other important considerations before choosing the characterisation method include knowledge of the required uncertainty in the measurement, the required frequency of operation. After the characterisation method has been chosen, the next stage involves looking at the possible sources of errors and how these can be dealt with.

Dielectric measurements of solids suffer in accuracy when contrasted with those for liquids because whereas liquids fill the sample holder, solids suffer from leaving air-gaps. To counter this problem when measuring solids, others [9] have proposed coating the solid SUT with conductive material. Although this has the tendency of changing the line impedance and line loss, it is outweighed by the improved dielectric measurements as long as the air-gap is small. It was shown in section 2.2.3 that even though liquids have the advantage of being able to fill the container completely, they inadvertently add another material to be considered when doing the analysis. This is

overcome by de-embedding the obtained results by shifting the measurement plane to the liquid interface. There is therefore need to use a material with known properties as the container.

Chapter 3

In-Waveguide SIW Sensor

3.1 Introduction

This chapter sets out to develop an SIW sensor for micro-litre liquid characterisation in the millimetre wave regime using a transmission line method. Overall, the sensor combines the well-known transmission line de-embedding methods coupled with the newly developed Low Temperature Cofired Ceramic (LTCC) hollow SIW technique [29] in establishing a hollow structure in LTCC as the sample holder and subjecting the liquid under test to an E-field in the millimetre wave region. Although all efforts were made to fabricate the designed in-waveguide SIW LTCC sensor, the design was ultimately not made due to practical difficulty in vias hole filling and equipment availability for patterning. This meant that this work is presented with only simulation results and other methods were adopted, as described in chapter 4 and 5.

It is well established in literature [22, 30-34] that transmission line methods offer the advantage of obtaining results over a wide bandwidth while giving comparatively accurate results to the resonance methods. However high loss liquid (lossy) measurements done at higher frequency, starting from the millimetre wave and upwards, pose a challenge as subjecting the liquid sample to the E-field direct path tends to cause high field attenuation that compromises the sensor's sensitivity. To overcome this, it is desired that sensors designed for millimetre-wave and sub-millimetre-wave work with

extremely low volumes of liquids for reasonably meaningful results to be obtained.

To achieve low liquid volume measurement while placing the liquid under test in the direct EM field path of a waveguide is not trivial. However, with the advanced research methods in LTCC technology, many millimetre-wave applications and beyond that were not possible are now possible. LTCC makes it possible to build solutions that are especially structured as layers. These layers can be structured separately as per design and then co-fired together to make a complete system. In some cases layers can be co-fired separately and then integrated together at the final design stage.

Using LTCC has made it possible for a novel substrate integrated sensor built using Dupont 9K7 to be designed. The design has used some elements of substrate integrated waveguides (SIW) coupled with hollow SIW. The employment of vias walls in this regard helps to structure the full design given the fact that solid walls would be impossible to implement. To however enhance the performance of the sensor, the end product has been a compromise that has both solid walls and vias walls. The final design has the broader walls using solid walls with the narrow walls using vias walls.

3.2 Sensor design

The designed sensor works in the Q-band, between 33 – 50 GHz. This has great application potential in polar liquid measurements as very little ionic effects are experienced in this region and beyond. This particularly entails that results obtained are only as a result of the effect the liquid under test has on the EM field it is interacting with. This motivates the research

therefore, in that if accurate results can be obtained they then can all be attributed to the effect of the liquid on the applied electric field.

The sensor has three layers, namely the bottom and upper layers that are both built for the purpose of acting as covers for the microfluidic cavity. The microfluidic cavity forms the main part of the middle layer whose main purpose is that of being the sample holder, Fig. 3.1.

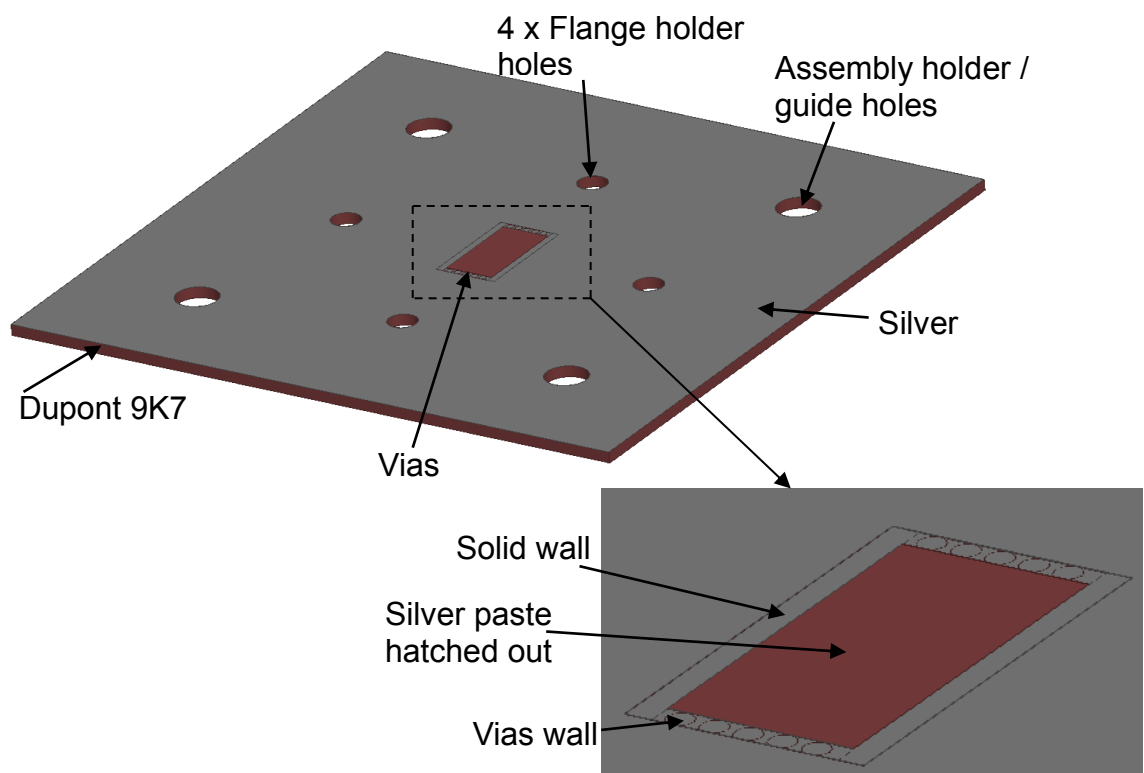


Figure 3.1 Top layer of the 3-layer structure

The walls of the structure are on the broad sides made of solid walls, while the vertical sides are made of vias holes as illustrated in Fig. 3.1. This ensures that the E-field loss is minimised. The details of the liquid cavity are shown in Fig. 3.2 that shows the middle layer.

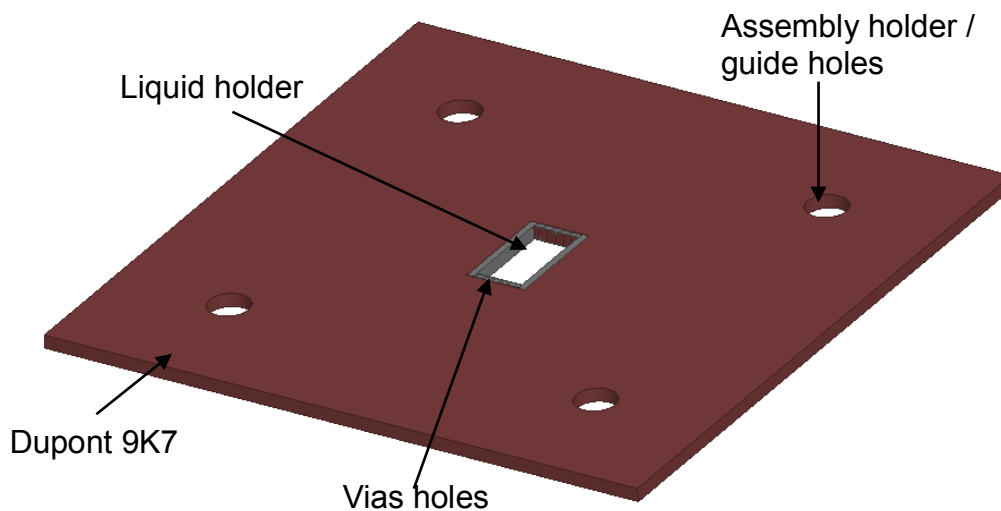


Figure 3.2 Liquid holder layer (middle layer)

The bottom layer and the top layer are designed exactly the same with the middle part left un-metallised as shown in Fig. 3.3.

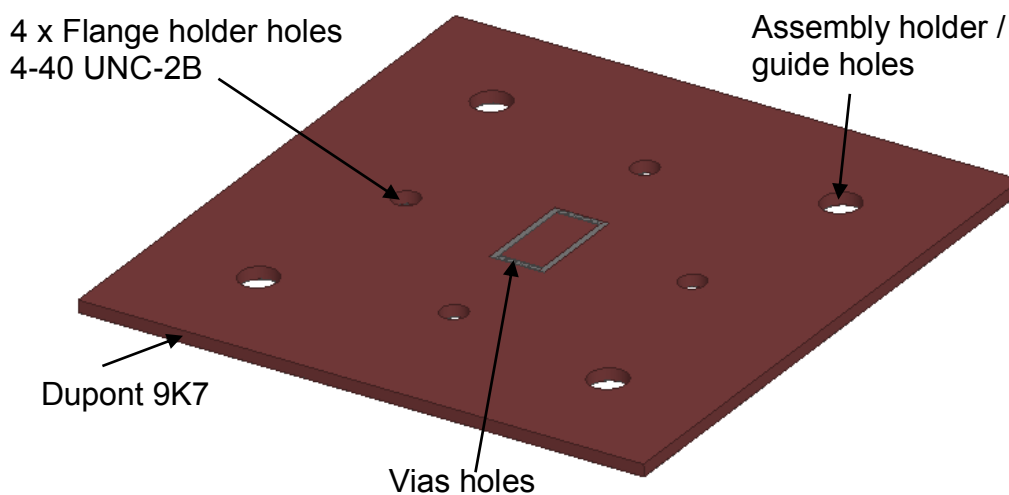


Figure 3.3 Bottom layer of the structure

The middle layer, in Fig 3.2, and the bottom layer, in Fig. 3.3, are cofired together to give a structure as shown in Fig. 3.4. The top layer is then assembled using the guide holes as shown in Fig. 3.5.

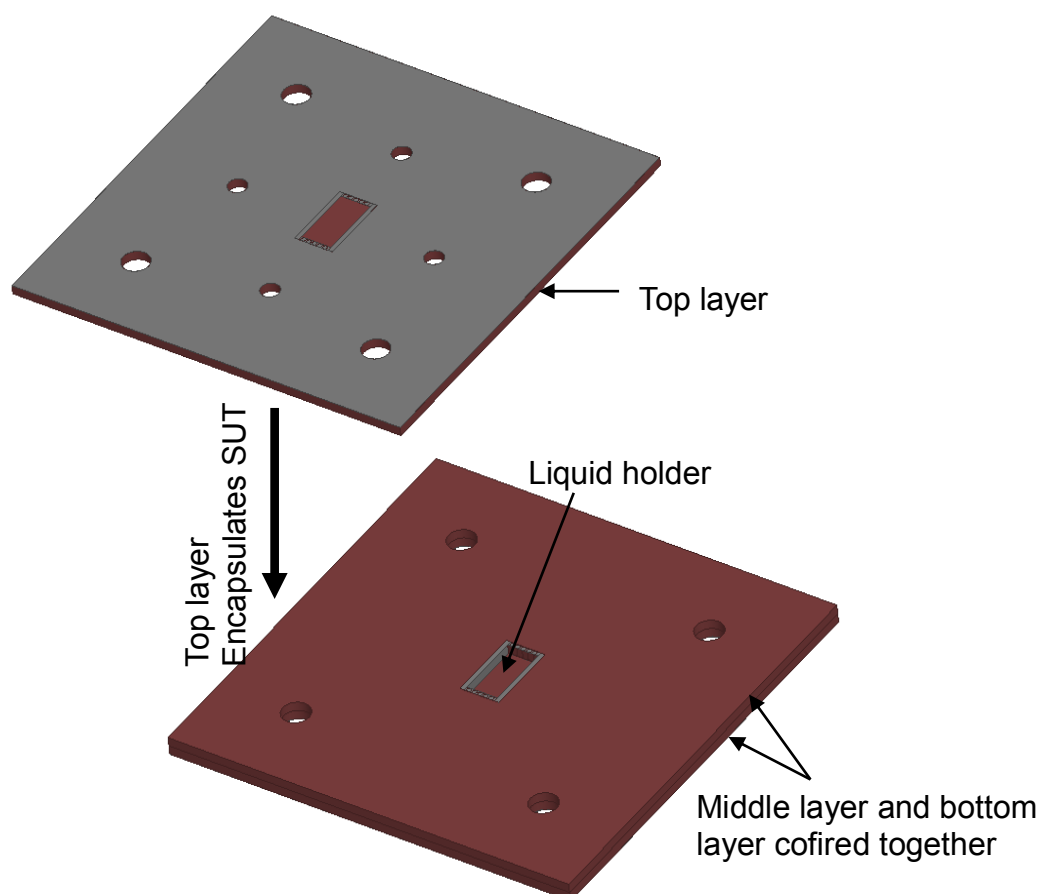


Figure 3.4 Assembly of the structure, middle and bottom layer are cofired together

Fig. 3.5 illustrates how the network analyser connections after a TRL calibration is performed were supposed to be done. The practical measurements were not done as the fabrication could not be completed as mentioned earlier. To ensure that the cavity was secure, 0.1 mm Dupont substrate material was left on each side of the cavity to hold the vias and solid walls in place. This implied that the complex permittivity calculated from the simulation was the effective permittivity of a combination of that of the liquid under test and the Dupont substrate on all sides of the liquid. Subsection 3.2.1 gives more details of the analysis used to develop the model.

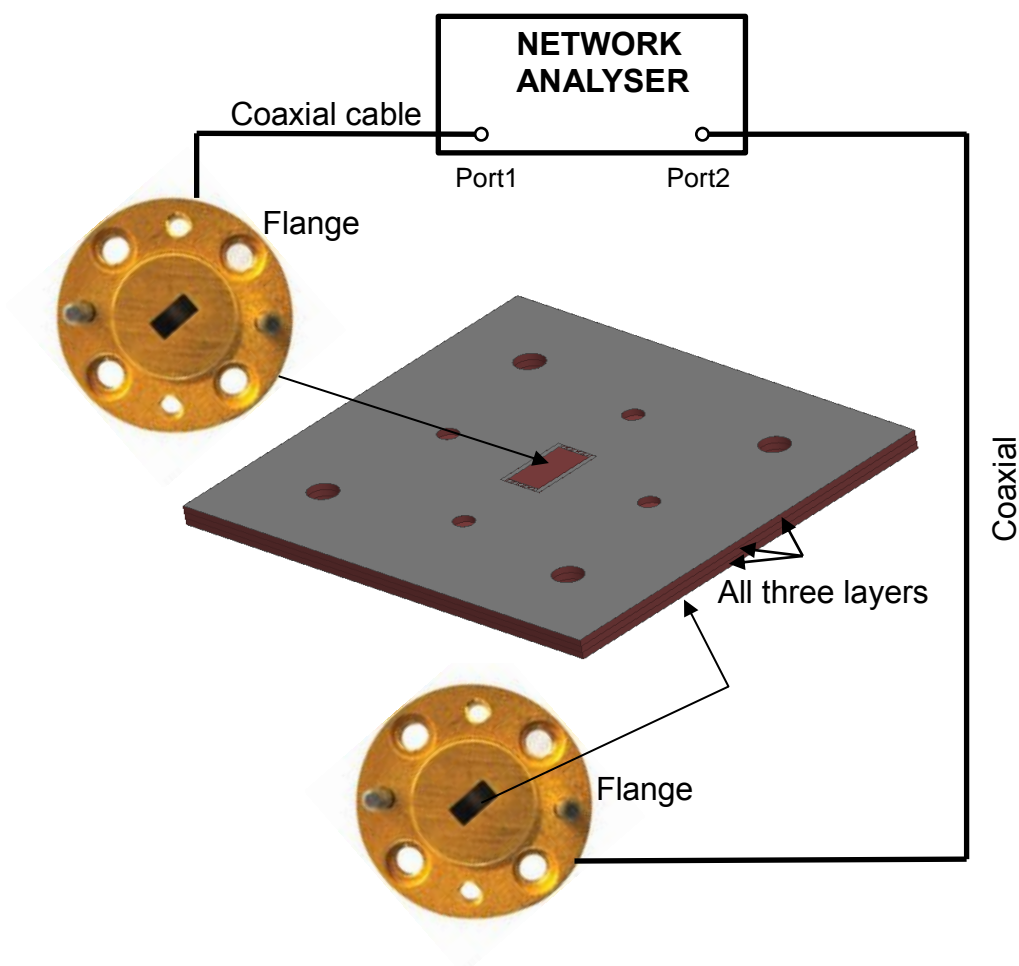


Figure 3.5 Network analyser illustration of the full setup

The upper and the lower layers are exactly the same and stay constant throughout the simulations. This is exploited in the method that has been used by obtaining the response to electric field of the two layers put together. This meant that the simulations that were carried out with all three layers in place in effect show the signal attenuation and phase change as a result of the liquid being measured. This electrical signature then relates directly to the liquid's properties and can hence lead to the liquid characterisation or identification.

The cavity needs to be fully filled to ensure that accurate results are obtained, and the maximum liquid volume that the sensor allows is $16 \mu\text{l}$.

This clearly shows that the proposed sensor is compact and well suited for liquid micro volume applications. The major limiting factor with the sensor is that the liquid volume will every time need to be the same, up to the capacity volume of the micro channel as no air spaces can be allowed.

The design was initially simulated using Ansys' 3D HFSS finite element software. The simulation designs were supposed to be fabricated using Dupont green tape 9K7 low temperature co-fired ceramic (LTCC) substrate, with ϵ_r' of 7.1 and $\tan\delta$ of 0.001. The Dupont 9K7 is free of both cadmium and lead and therefore exhibits biocompatible requirements for liquid measurements and does not pose any contamination challenges.

3.2.1 Analysis of the permittivity of the fluid

To understand the design fully, a look at the initial design stages is necessary. The waveguide used in this design is a WR-22 waveguide, operating in the Ka-band with a cut-off frequency (f_c) of 26.35 GHz. If only the dominant TE₁₀ is considered to propagate, the dimensions of the waveguide are obtained by using the following relationship [35],

$$f_c = \frac{1}{2\pi\sqrt{\mu_r'\epsilon_r'}} \sqrt{\left(\frac{m\pi}{a}\right)^2 + \left(\frac{n\pi}{b}\right)^2} \quad (3.1)$$

where ϵ and μ are the permittivity and permeability of the material filling the waveguide, a is the broad length of the waveguide, b is the height of the waveguide, and m and n represent the mode numbers.

For a vacuum filled waveguide propagating the TE₁₀ mode, (3.1) reduces to

$$f_c = \frac{1}{2a\sqrt{\mu_r'\epsilon_r'}} = \frac{c}{2a} \quad (3.2)$$

where c is the speed of light in free space and the other variables are as defined before.

$a = \frac{c}{2f_c} = 5.69\text{mm}$ in this particular case with the cut-off frequency defined as before. The design works as a wideband liquid characterisation sensor, operating between 33.35 GHz and 50.35 GHz.

Through using HFSS and simulating a high loss liquid (namely deionised water), the optimum waveguide hollow length for holding the liquid was derived as 1mm, with the encapsulating covers on top and below also being 1 mm as shown in Fig. 3.5. The total length of the waveguide in this design is therefore 3 mm.

The final structure shown in Fig. 3.5 is taken as a three layer structure with two liquid encapsulating layers or barriers of similar composition, namely the top and the bottom layers. This therefore helps to make the permittivity analysis more straight forward as the two layers were combined to form a through standard which was also used during the calibration stage. The initial stage therefore involves getting two port S-parameters of the through standard, that is the top and bottom layer together. No part of the liquid sample was introduced at this stage. In essence, it then gives an opportunity for different types of liquids to be measured as the subsequent measurements will have no dependency on the de-embedded part of the encapsulating layers.

Fig. 3.5 can be simplified as shown in Fig. 3.6 to simplify the analysis.

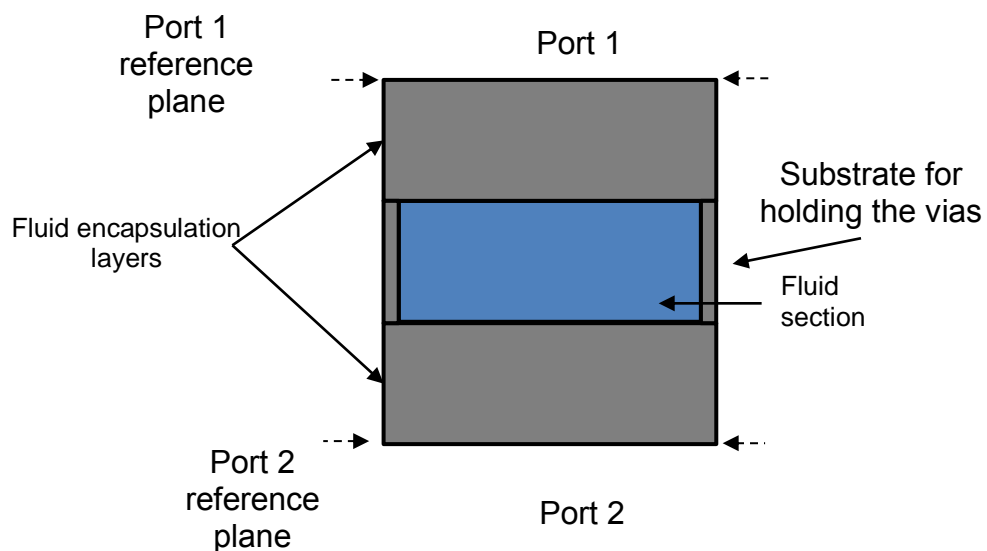


Figure 3.6 Cross section of the entire assembly or line assembly

The through standard on the other hand can be simplified as shown in Fig. 3.7.

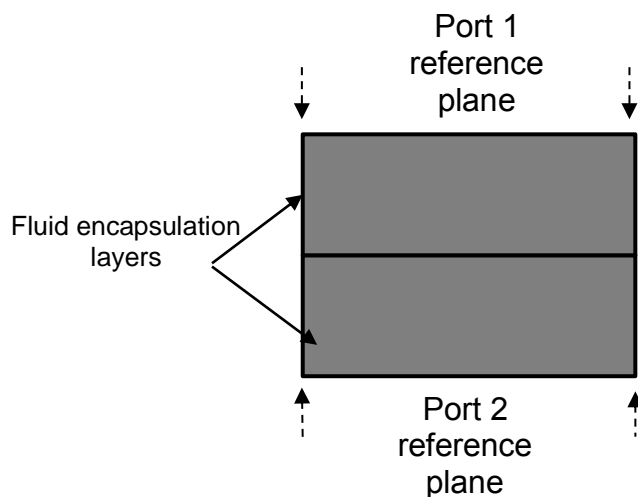


Figure 3.7 Cross section of the through standard

The simulated S-parameters for both the line and the through standard are transformed to T-matrices (transfer matrix or sometimes known as transmission matrix), T_{line} and T_{thr} respectively as shown in (3.3):

$$\begin{bmatrix} T_{11} & T_{12} \\ T_{21} & T_{22} \end{bmatrix} = \begin{bmatrix} \frac{S_{12}S_{21} - S_{11}S_{22}}{S_{21}} & \frac{S_{11}}{S_{21}} \\ -\frac{S_{22}}{S_{21}} & \frac{1}{S_{21}} \end{bmatrix} \quad (3.3)$$

This was necessary as T-matrices offer a mathematically simpler way of handling cascaded networks.

From Fig. 3.6 and considering the entire assembly as a cascade, the total T-matrix, T_{line} , can be expressed as:

$$[T_{line}] = [T_p] \cdot [T_{liq}] \cdot [T_p] \quad (3.4)$$

where $[T_p]$ represents the T-matrix for the top and bottom encapsulating layers and $[T_{liq}]$ is the T-matrix for the middle liquid layer.

Similarly for the through scenario given in Fig. 3.7, the total T-matrix can be expressed as:

$$[T_{th}] = [T_p] \cdot [T_p] \quad (3.5)$$

By combining (3.3) and (3.4), T_{liq} can be found as:

$$[T_{line}] \cdot [T_{th}]^{-1} = [T_{liq}] \quad (3.6)$$

From (3.6) it is clear to see that $[T_{line}]$ and $[T_{th}]$ are known either from measurement or simulation. $[T_{liq}]$ is unknown and contains the dielectric properties of interest. By finding the trace of either side of equation (3.6) it is possible to use the Newton Raphson method to iteratively calculate the complex permittivity of the liquid [34]. In this work fsolve, an iterative function in Matlab, was used to iteratively solve the trace of (3.6) and in so doing calculate the complex permittivity of different liquids:

$$Tr ([T_{line}] \cdot [T_{th}]^{-1}) = Tr ([T_{liq}])m \quad (3.7)$$

where m signifies the measured or simulated value.

The trace of an $n \times n$ square matrix B with entries b_{ij} , is defined as:

$$Tr(B) = \sum_{i=1}^n b_{ii} \quad (3.8)$$

In other words the trace of the matrix B is the sum of all the diagonal entries, where the diagonal entries are defined as entries when $i = j$ [36] .

The theoretical T-matrix of the liquid layer is defined as:

$$[T_{liq}] = \begin{bmatrix} e^{-\gamma_s l_s} & 0 \\ 0 & e^{\gamma_s l_s} \end{bmatrix} \quad (3.9)$$

The trace of (3.9) is then given as:

$$Tr([T_{liq}]_t) = 2Cosh(\gamma_s l_s) \quad (3.10)$$

where t emphasises that the trace is for the theoretical case, l_s is the length occupied by the liquid layer, and γ_s is the propagation constant given as:

$$\gamma_s = \frac{j2\pi}{\lambda_0} \sqrt{\epsilon_r^* - \left(\frac{\lambda_0}{\lambda_c}\right)^2} \quad (3.11)$$

From (3.11) it can be clearly seen that the propagation constant contains in it the complex permittivity of the liquid under test. This expression when substituted in (3.10) forms the basis for complex permittivity extraction as is shown in this section.

The simulated S-parameters from the cross section models shown in Fig. 3.6 and Fig. 3.7 were converted to the T-parameters using the relationship given in (3.3).

Using (3.3), the through T-parameters become

$$[T_{th}] = \begin{bmatrix} \frac{-detS_{th}}{S_{21}^{th}} & \frac{S_{11}^{th}}{S_{21}^{th}} \\ -\frac{S_{22}^{th}}{S_{21}^{th}} & \frac{1}{S_{21}^{th}} \end{bmatrix} \quad (3.12)$$

where $\det S_{th}$ stands for determinant of the S-parameter matrix of the through scenario and th is the abbreviation for through.

From (3.12), the inverse $[T_{th}]^{-1}$ required in (3.6) is derived as follows:

$$\det[T_{th}] = \frac{s_{11}^{th}s_{22}^{th}-\det S_{th}}{s_{21}^{th2}} \quad (3.13)$$

$$[T_{th}]^{-1} = \frac{s_{21}^{th2}}{s_{11}^{th}s_{22}^{th}-\det[S_{th}]} \begin{bmatrix} \frac{1}{s_{21}^{th}} & -\frac{s_{11}^{th}}{s_{21}^{th}} \\ \frac{s_{22}^{th}}{s_{21}^{th}} & \frac{-\det[S_{th}]}{s_{21}^{th}} \end{bmatrix} \quad (3.14)$$

Similarly, the transformed S-parameters of the entire structure is given as:

$$[T_{line}] = \begin{bmatrix} \frac{-\det[S_{line}]}{s_{21}^{line}} & \frac{s_{11}^{line}}{s_{21}^{line}} \\ -\frac{s_{22}^{line}}{s_{21}^{line}} & \frac{1}{s_{21}^{line}} \end{bmatrix} \quad (3.15)$$

Using (3.14) and (3.15) in (3.6) leads to the derivation of the T-matrix due only to the SUT given by:

$$[T_{line}] \cdot [T_{th}]^{-1} = \begin{bmatrix} \frac{s_{21}^{th}s_{22}^{line}-s_{11}^{th}\det[S_{line}]}{s_{11}^{line}(s_{11}^{th}s_{22}^{th}-\det[S_{th}])} & \frac{s_{11}^{th}s_{21}^{th}\det[S_{line}]-s_{11}^{line}s_{21}^{th}\det[S_{th}]}{s_{11}^{line}(s_{11}^{th}s_{22}^{th}-\det[S_{th}])} \\ \frac{s_{21}^{th}s_{22}^{th}-s_{21}^{th}s_{22}^{th}}{s_{11}^{line}(s_{11}^{th}s_{22}^{th}-\det[S_{th}])} & \frac{s_{11}^{th}s_{21}^{th}s_{22}^{line}-s_{21}^{th}\det[S_{th}]}{s_{11}^{line}(s_{11}^{th}s_{22}^{th}-\det[S_{th}])} \end{bmatrix} \quad (3.16)$$

From (3.16) the trace can be found as:

$$Tr ([T_{line}] \cdot [T_{th}]^{-1}) = \frac{s_{11}^{line} \cdot s_{22}^{th} + s_{11}^{th} \cdot s_{22}^{line} - \det[S_{th}] - \det[S_{line}]}{s_{21}^{line} \cdot s_{12}^{th}} \quad (3.17)$$

Eqn. (3.17) as per relationship in (3.7) gives the trace of the simulated or measured liquid, i.e.

$$Trace(liq)_m = \frac{s_{11}^{line} \cdot s_{22}^{th} + s_{11}^{th} \cdot s_{22}^{line} - \det[S_{th}] - \det[S_{line}]}{s_{21}^{line} \cdot s_{12}^{th}} \quad (3.18)$$

where m signifies that this is a measured or simulated result.

Using (3.10) and (3.18), a set of nonlinear functions is formed that reduces to zero. By iteratively solving these using a Newton Raphson method, the complex permittivity is extracted from the created function as follows:

$$F(\epsilon_{eff}^*) = [real(Tr(liq)_m - Tr(liq)_t); imag(Tr(liq)_m - Tr(liq)_t)] \quad (3.19)$$

The extracted effective complex permittivity is defined as such because as per Fig. 3.6 it includes the liquid section and the small substrate section for holding the vias wall.

A Matlab program was written to perform these functions coupled with the in-built `fsolve` function that was used to solve the nonlinear equations. This is given in more detail in appendix A. The extracted permittivity properties of various liquids are given in Section 3.3 and Section 4.4.

The next section introduces the measurement done using the Keysight dielectric measurement probe. These measurements were used to validate the simulation results of the developed sensor introduced in this chapter.

3.2.2 Keysight dielectric probe kit

The measurements using the dielectric probe validated the simulations done using the transmission/reflection method. This was also compared to other results in the literature. The dielectric probe kit makes it possible for measurements of complex permittivity to be undertaken for a wide range of semi-solids, malleable solids and liquid materials. The probe kit does all the network analyser control functions and calculations using the software installed either on the network analyser or an external computer. Once the reflection coefficient has been measured and presented to the software, it

converts it to the complex permittivity of the SUT. The results obtained are presented in various ways including plots of relative permittivity, loss tangent, loss factor, cole-cole as well as the tabular form of the same.

Keysight have three dielectric probes that have some differences in their usage and the range of operation [37]:

3.2.2.1 Performance probe

This probe comes in a slim design and combines rugged, high temperature and frequency performance. It comes sealed on the probe tip and the connector end and hence makes it to withstand harsh conditions. It can operate over a very wide temperature range from -40°C to $+200^{\circ}\text{C}$ and hence can be used for measurements done as a function of frequency or those done as a function of temperature. Its frequency range is from 500MHz to 50GHz. Because of its ruggedness, it finds application in fermentation tanks, chemical reaction chambers and many other food applications.

The performance probe is mostly used in measuring liquids, but has also found application in measurement of semi-solids and flat surfaced solid materials.



(a)



(b)

Figure 3.8 (a) Performance Probe (b) Calibration short [37]

3.2.2.2 High temperature probe

This probe is also rugged in design and is able to survive corrosive chemicals and withstands high temperatures. Its temperature range is -40°C to 200°C and can therefore be used for measurements as a function of either temperature or frequency. Its frequency range is however only between 200MHz to 20GHz but due to its large flange it gives better readings when used on flat faced solids as opposed to the other two. Its primary usage still remains on liquids.



Figure 3.9 High Temperature Probe Kit [37]

3.2.2.3 Slim form probe

As the name suggests, this probe comes in a slim design and therefore can be used in tight spaces and since they are designed as high turnover probes, sometimes they are cast into materials and left in place permanently until they can't be used anymore. The Slim Form Probe has a frequency range of 500MHz to 50GHz which makes it one of the most used probes due to its convenience and good frequency range. Its temperature range is from 0 to +125°C. The Slim probe can only be used for liquids or semi-solids that can conform to the probe tip. The minimum insertion of the probe is 5mm; this ensures that the sensing area is completely submerged in the SUT.

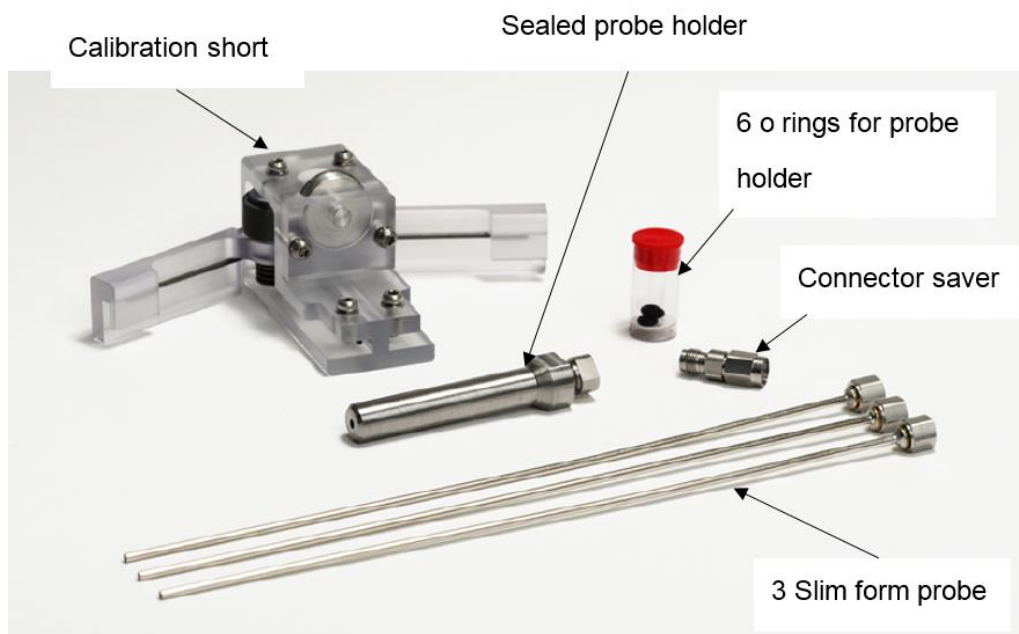


Figure 3.10 Three Slim Form Probes with the short standard and other accessories [37].

Apart from the probes, other important parts of the kit are the Electronic Calibration (ECal) module that is part of the setup and the flexible cable for connecting to the Network analyser. The ECal module has an automated electronic calibration feature that recalibrates the system automatically before each measurement is made. This helps eliminate the cable instability errors that can result when the cable is moved as can happen when moving the SUT to the sensor and also eliminates system drift errors. As much as possible the cable should be firmly fixed and not be subjected to movements once the calibration has been done. It's always advised that the cable should stabilise before any measurements can be made.

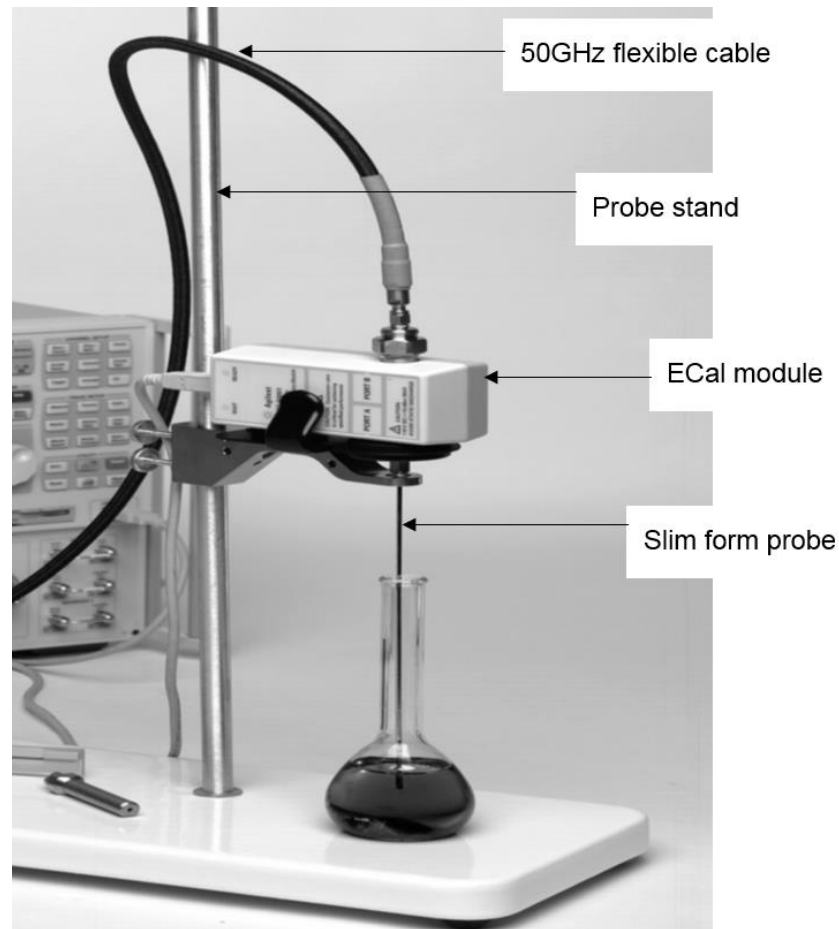


Figure 3.11 ECal module in use with Slim Form Probe also showing the flexible cable connecting to the Network Analyser [37]

3.2.3 Dielectric probe measurement results

Deionised water was measured with the Slim form probe inserted at different depth to see the effect of the depth on the measurements. In the first case, the probe was inserted up to 25mm deep in deionised water at 25°C and in the second case the measurement was taken at 50mm insertion depth. At both depths the measurements did not show much change except minor differences that could be as a result of the liquid drifting in temperature slightly between the measurements.

3.2.3.1 Measurements done with Probe immersed at 25mm and 50mm

The Fig. 3.12, Fig. 3.13 and Fig. 3.14 give the results obtained during measurements using the Keysight dielectric slim form probe immersed at 25mm and 50mm into deionised water.

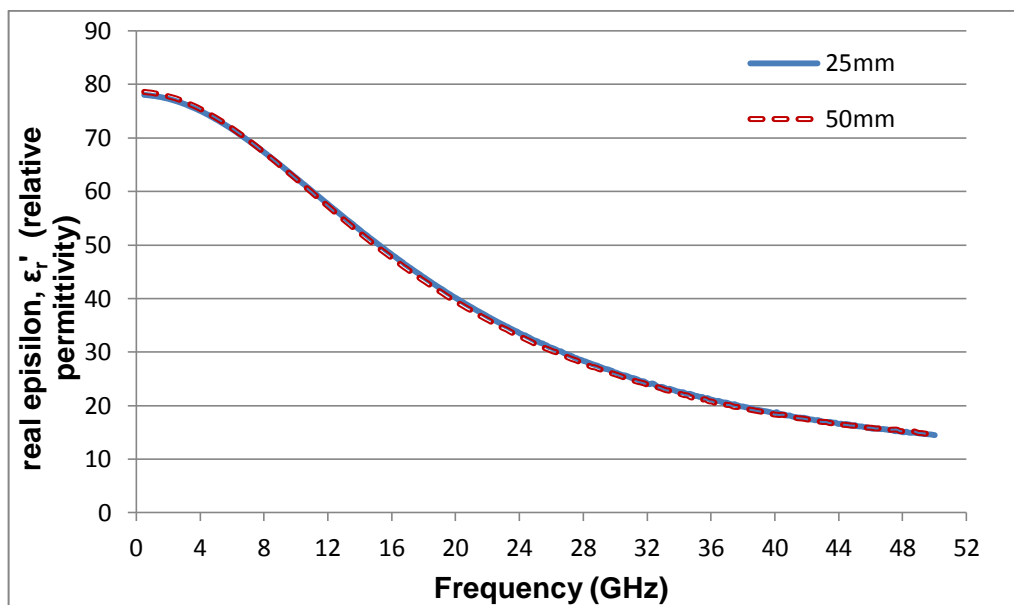


Figure 3.12 Deionised water relative permittivity measurement results at 25mm and 50mm probe depth

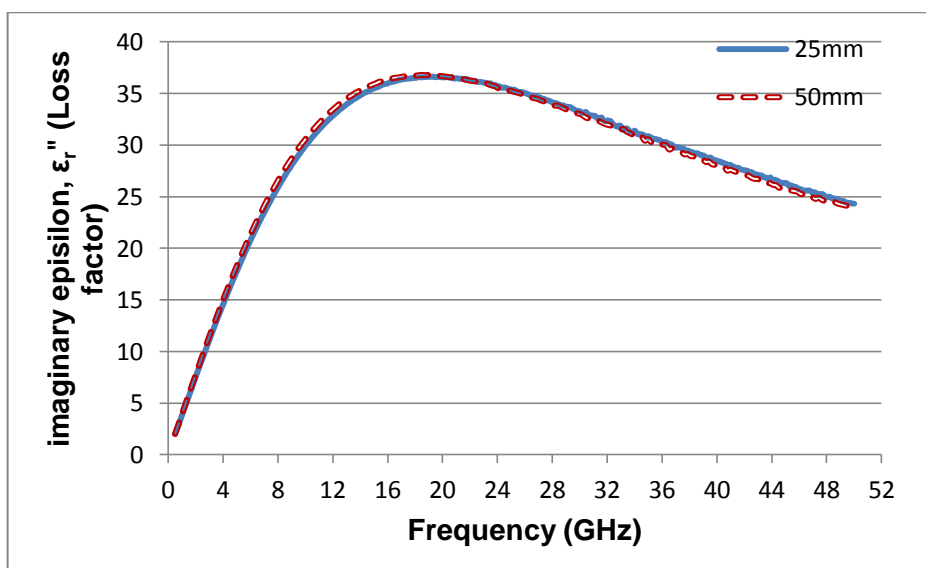


Figure 3.13 Loss factor measurement results at 25mm and 50mm probe depth immersed in deionised water

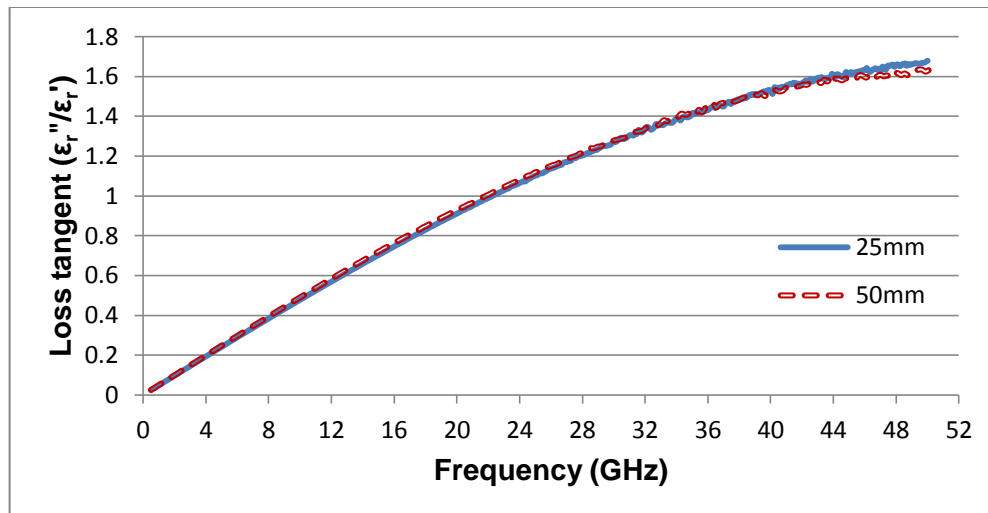


Figure 3.14 Deionised water loss tangent measurement at 25mm and 50mm probe depth

From the results obtained it is clear that once the mandatory 5mm depth of probe immersion has been achieved, it does not matter how deep the probe is immersed as long as it is not inserted too close to the base of the sample holder. In both cases above, it was ensured that the probe was not close to the base of the sample holder. The probe should not be immersed to anywhere near the base of the sample holder so that the measured reflection coefficient is purely from the sample. This meets the requirement for this method which desires that the sample is infinite in size. To confirm this, a short was put at the base of the beaker without seeing its influence on the measurement result.

3.3 Simulation results

In this section the simulation results using the in-waveguide LTCC sensor are presented. The extraction of the complex permittivity of the liquid under test was done using the three stage method given in section 3.2.1:

- a. Simulate the through standard to obtain the scattering parameters.
This is the case where only the two cover layers are considered, namely the top layer and the bottom layer.
- b. Simulate the line scenario. This is the setup where all three layers with the liquid well encapsulated are considered.
- c. Use the developed matlab code to extract the complex permittivity of the liquid.

In the following subsection, the simulation results for deionised water and methanol are presented.

3.3.1 Deionised water simulation results

Fig. 3.15 gives the S-parameter plot of the through standard. The through standard scattering parameters shown in Fig. 3.15 are to be used for all subsequent simulations of different liquids as they are part of the permanent fixture.

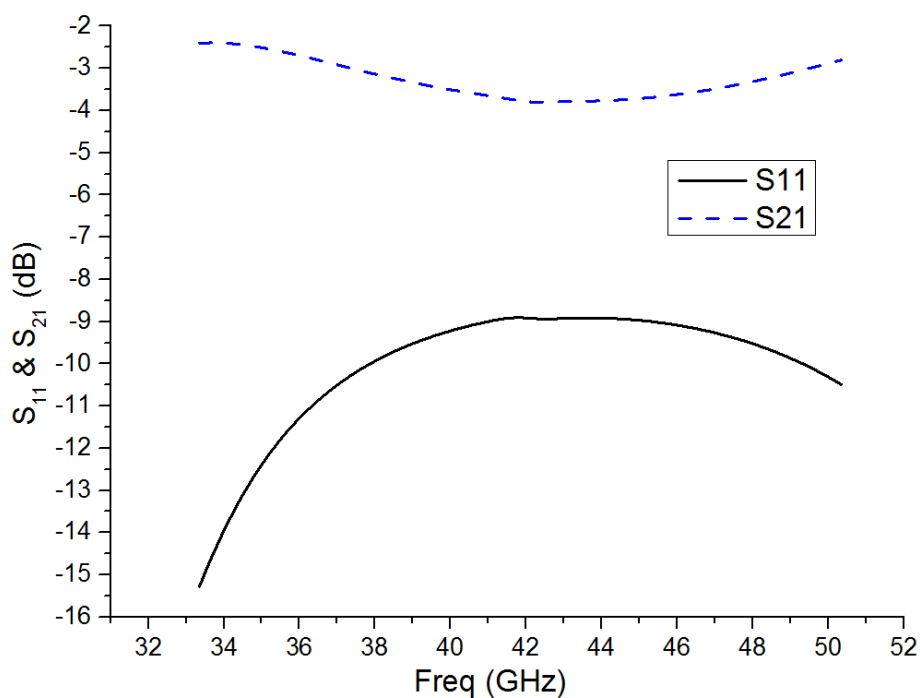


Figure 3.15 S₁₁ and S₂₁ plots for through standard

The line simulation with deionised water as the sample was then undertaken. All these simulations only took place after the optimised sample thickness for high loss liquids had been determined through several simulations in the earlier work. In these simulations it was concluded that as long as the S_{21} was above -30dB , valid results of the complex permittivity could be obtained. As can be seen in Fig. 3.16 the simulation of deionised water as the SUT falls well within the limits of operation of this sensor.

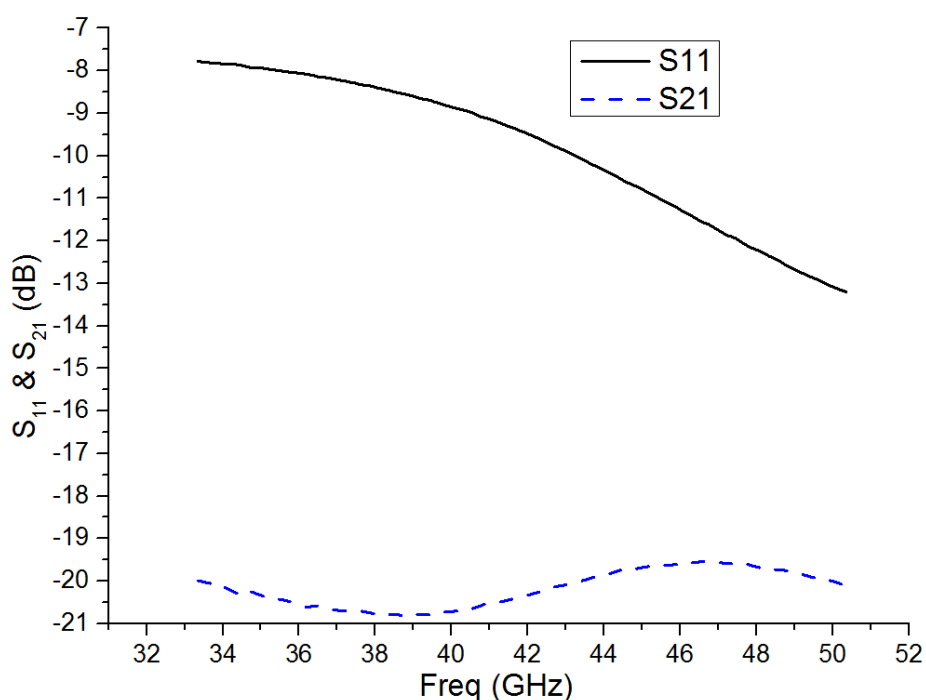


Figure 3.16 S_{11} and S_{21} Simulation results for Deionised water using the in-waveguide sensor

Using the scattering parameters presented in Fig. 3.15 and Fig. 3.16 the complex permittivity of the liquid was extracted for this broadband case between 33.35 GHz to 50.35 GHz as shown in Fig. 3.17.

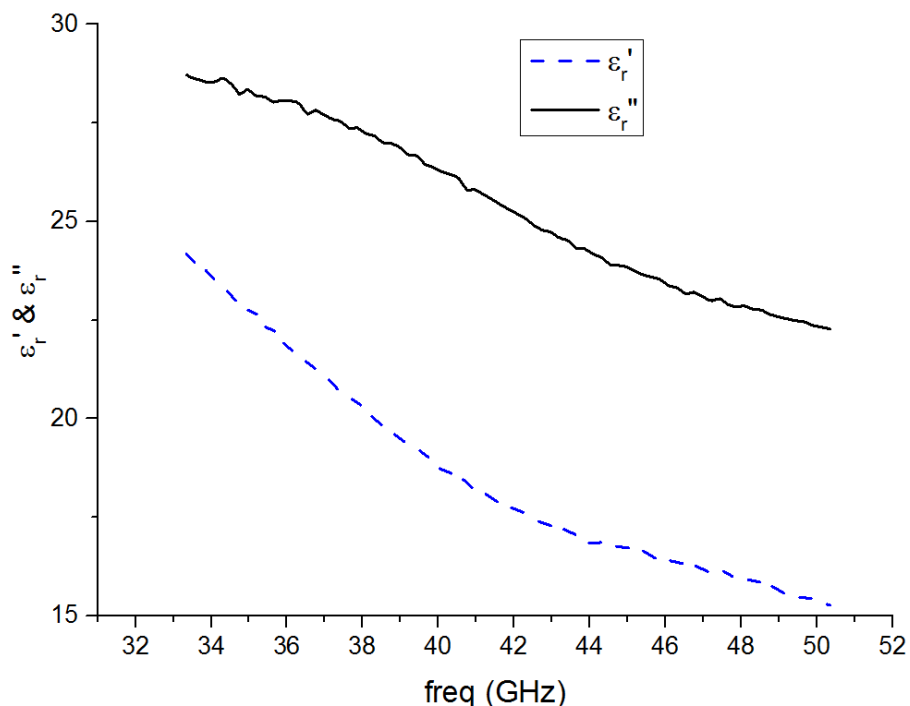


Figure 3.17 Extracted real and imaginary part of the complex permittivity of deionised water

3.4 Comparison of In-SIW sensor results with dielectric probe kit measurement results

The simulated results using the in-waveguide sensor were then compared with the measurement results obtained using the Keysight dielectric probe kit. Close agreement between the results was achieved which validated the designed sensor. For this exercise, deionised water and methanol were considered with the results as given in Fig. 3.18 – Fig. 3.21. Using two pure liquids and obtaining the results as presented was sufficient validation of both the design and the complex permittivity extraction method. In the extraction method, as shown in appendix A, the debye model was used as the initial estimation of the complex permittivity of the sample at the start frequency (33.35 GHz). The Matlab program converged quickly to the

correct complex permittivity values once it was run. After the conversion of the first iteration at 33.35 GHz, this value is then used as the initial estimate for the next iteration and so on and so forth until all the frequency points have been exhausted.

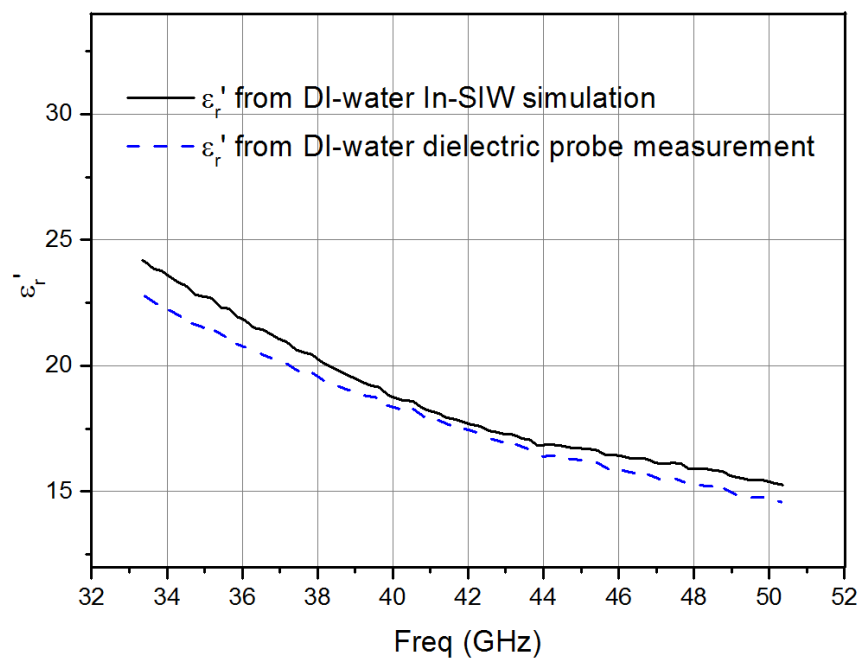


Figure 3.18 Relative permittivity result for Deionised water when measured using the Keysight dielectric probe and LTCC in-waveguide sensor simulation result

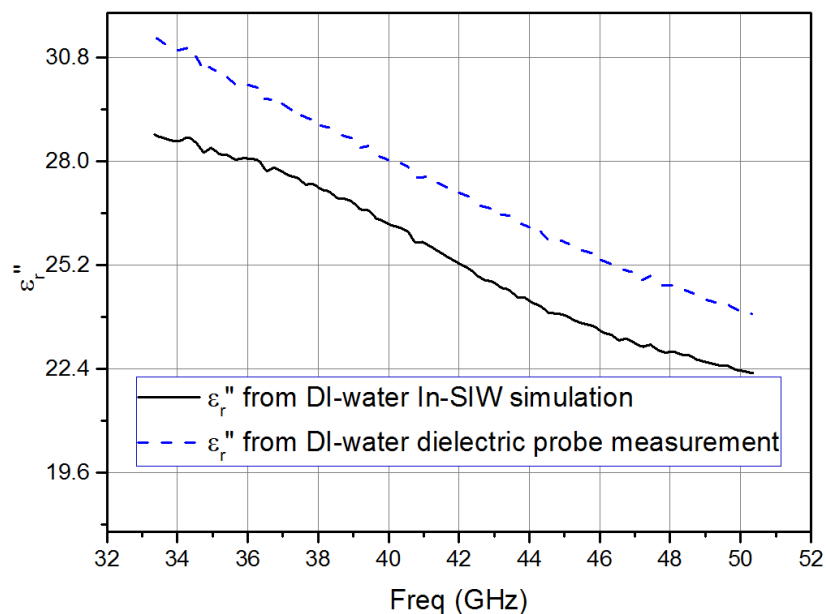


Figure 3.19 Loss factor of Deionised water when measured using the Keysight dielectric probe and the LTCC In-waveguide simulation result

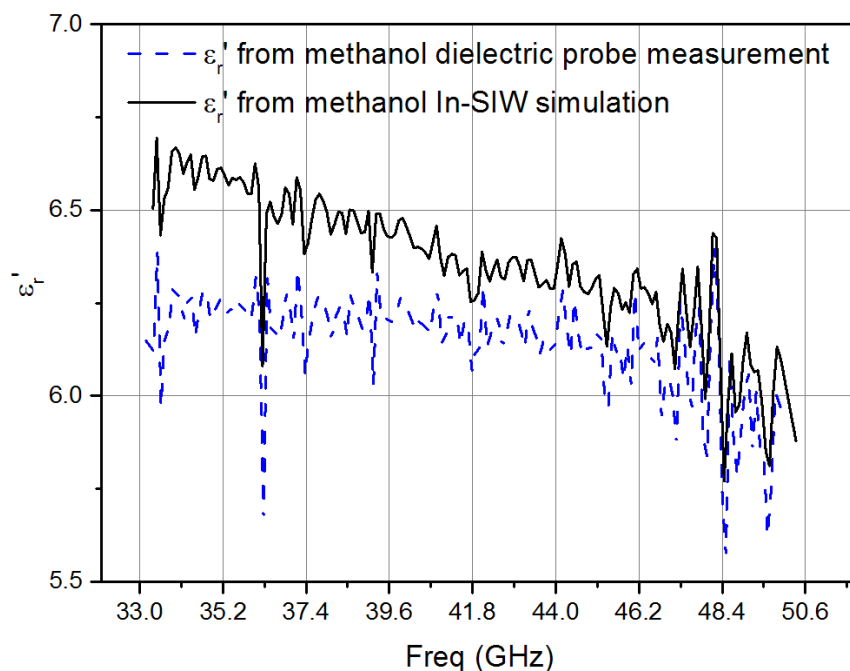


Figure 3.20 Relative permittivity of Methanol when measured using the Keysight dielectric probe and the simulation result of the LTCC in-waveguide sensor

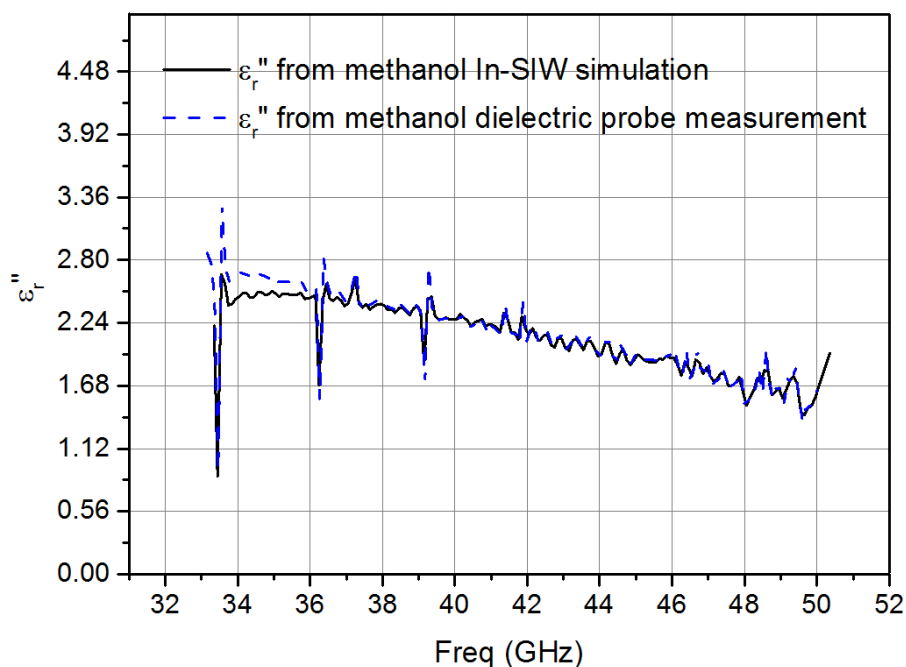


Figure 3.21 Loss factor of Methanol when measured using the Keysight dielectric probe and the simulation result when using the designed in-waveguide sensor

The slight difference between the measured results and the simulated results was attributed to the final part of the complex permittivity extraction that used a simple mixing formula to eliminate the effect of the substrate support wall from the calculated effective permittivity. Using a robust mixture model like the Maxwell-Garnet model would have yielded a closer agreement as observed in Chapter 4.

3.5 Summary

In this chapter, the development of an In-waveguide broadband liquid characterisation sensor based on an SIW structure has been described. The SIW structure was proposed to be fabricated using LTTC due to the easy with which it enables layered structures to be fabricated. It was

proposed that the bottom layer and the middle layer (which has the liquid cavity), were to be cofired together. This would lead to the creation of a stable hollow structure. Since each layer was going to be 1mm thick, 4 layers of raw LTCC were to be used (each layer being 254 μm). Although this structure was not successfully fabricated, the design, simulation and analysis offered valuable learning experience that was used in the subsequent work. Equally during this work the coding analysis of material dielectric properties was developed. This involved extracting the material dielectric properties based on the propagation constant of the wave in the material under test. The next chapter will present a sensor that evolved from the work discussed in this chapter as it aimed to seek a sensor where the SUT interacted only with the evanescent waves and near-fields generated by the main transmission line.

Chapter 4

Microfluidic-Integrated SIW Lab-on-Substrate Sensor for Microlitre Liquid Characterisation

4.1 Introduction

Microfluidic devices use a compact design to perform microlitre or nanolitre liquid volume measurements [38]. Predominantly, microfabrication techniques are employed to create micro-channels, whereas liquid insertion is achieved by using pumps, syringes and valves. Some measurements require that the liquid is flowing at all times whereas other measurements may take place with the liquid in what is referred to as a static state (not flowing). Sometimes, more than one microfluidic channel is used to enable the insertion of more than one liquid and allow for chemical reaction of the liquids to further facilitate property measurements as the mixture transitions through various stages.

Microfluidic devices and/or lab-on-substrate devices have been used in sensors to characterise various chemical and biological liquids. Most devices tend to consist of two parts: one part provides for the microwave or optical circuit whose characteristics vary when exposed to the sample under test (SUT), the other part comprises the microfluidic channels with their covers. Lab-on-substrate devices are patterned on planar surfaces that allow for standard fabrication processes, from PCBs to metal electrode deposition.

The work in Chapter 4 is published in the IEEE sensors journal [39] and was presented when in its early stage at the European Microwave Conference

2016 [40]. The journal extended the work presented at the European Microwave Conference. This work presented for the first time a microfluidic sensor fabricated using an SIW structure that ensured that the device was planar and compact while returning the performance of the standard equivalent waveguide structure.

Biological sensors play a critical role in the everyday investigation and analysis of liquids/fluids in various medical and biological applications [31, 41-44]. Cell identification and quantification particularly are significant in arresting certain potential life threatening cases in the human body. This impact and motivation have been working as drivers to enhance further research into cheaper, environmentally friendlier and higher accurate devices but require very small volume of the sample materials. Additionally, the continued advancement in micro-technology and computational techniques are huge contributing factors to the current enhancement being seen in the quest for accurate biological material characterisation.

Resonance methods are the most accurate when used in electrical material properties characterisation and material quantification compared to the other available alternatives such as transmission-line techniques [25, 26, 45-47]. The resonance methods are normally used to characterize materials at either a single frequency or a narrow band. Previously, resonance methods were restricted to measurement of low loss materials due to broadening of the resonance curve as the loss increased. However, the methods have recently been adapted to measure and characterize high-loss liquids through various modeling techniques [48]. Due to the high sensitivity of resonance

methods, they particularly allow for reduction of sample volume and enhance sensor compactness [49].

With the advancement of substrate integrated waveguides (SIWs) in the last decade, it is now possible to design planar devices offering functionality that was previously reserved for traditional waveguides. This reduces cost, offers reduced size and makes for easy integration with other planar circuits [50, 51]. Recently, [52] an SIW resonator sensor for liquid permittivity measurements was presented. However, the sensor requires substantial liquid volume as well as sensor immersion in the liquid. The immersion exposes the sensor to the possibility of contamination as well as corrosion. In [26] a planar resonator is presented, although compact, it is only able to characterize liquids with relative permittivity extending from 20 to 40 as these are the limits of the predictive model employed.

In this chapter, a novel liquid sensor with application for liquid mixture solutions detection, identification and quantification, e.g. cell quantification, that combines the following advantages compared to the state-of-the-art is presented: 1) measurement of relative permittivity, real part of complex permittivity, with ϵ'_r ranging from low ϵ'_r to high ϵ'_r materials with no technical restriction, 2) noninvasive and contactless characterization, 3) compact liquid volume, with only 7 μl being sufficient, and 4) potentially reusable sensor requiring only a replacement of the microfluidic subsystem in the plug-and-play fashion. The sensor is made reusable by creating guiding holes on the microfluidic subsystem and the microwave subsystem. Furthermore, a mathematical model is developed to analyse and synthesize the SIW sensor. Based on the proposed analytical model, a program

implemented by using MATLAB is developed to transform the measured return losses and resonant frequencies to various interesting liquid material properties, e.g. dielectric constants. A performance comparison is conducted between the designed sensor and the commercial sensor from Keysight Technologies and other sensors designed by others. The frequency choice of 10 GHz is a compromise between sensor sensitivity and cost. At much lower frequency, the sensor would become less sensitive, while at very high frequency the sensitivity would increase but so would the fabrication cost and measurement challenge.

4.2 Working principle and sensor design

Fig. 4.1 and Table 4.1 show the 3D structure and important design parameters of the SIW microfluidic-microwave sensor. The sensor is implemented using an SIW structure integrated on top with a longitudinal slot antenna, designed to operate at the center frequency of 10 GHz. The SIW is implemented based on a RT/Duroid 5880 substrate that is copper plated on the top and the bottom surfaces. Vertical copper plated via holes electrically connect the top copper layer to the bottom copper layer, thereby forming both side walls of the SIW. One edge of the SIW, as shown in Fig. 4.1, is short-circuited by using a series of vertical copper plated via interconnections. A longitudinal rectangular slot cavity antenna is then created into the top metallic layer with its center position located at a quarter-wavelength distance from the short-circuited end of the SIW. For the measurement, an additional 50- Ω microstrip feed line is integrated to the

design with a tapered microstrip transition that matches the SIW impedance of $72\text{-}\Omega$ at the design frequency to that of the 50-ohm microstrip.

Electromagnetic (EM) field radiation from the rectangular slot antenna occurs because the slot cavity interrupts the transverse surface currents in the metallic wall of the SIW, thereby creating an electric field in the slot. The induced electric field can be viewed using its equivalent magnetic sheet and radiates into the outer space [53]. To create a contactless sensor, a dielectric layer is used to cover on top of the SIW slot antenna, acting as an isolation layer between microwave and microfluidic subsystems. A microfluidic subsystem, consisting of a micro-channel and liquid in and outlets, is then created in another substrate, which is subsequently bonded on top of the isolation layer. The final substrate layer, performing as a liquid-channel cover, was then bonded on top of the microfluidic subsystem to encapsulate the liquid inside the microfluidic channel. The microfluidic channel is transversely located above the centre of the antenna slot where the radiated EM near-field is maximum in order to get the best sensing accuracy and sensitivity. The sensing principle is to track any changes in resonant frequency and return loss of the slot antenna as a result of an interaction between the radiated near-field and the encapsulated liquid in the microfluidic channel.

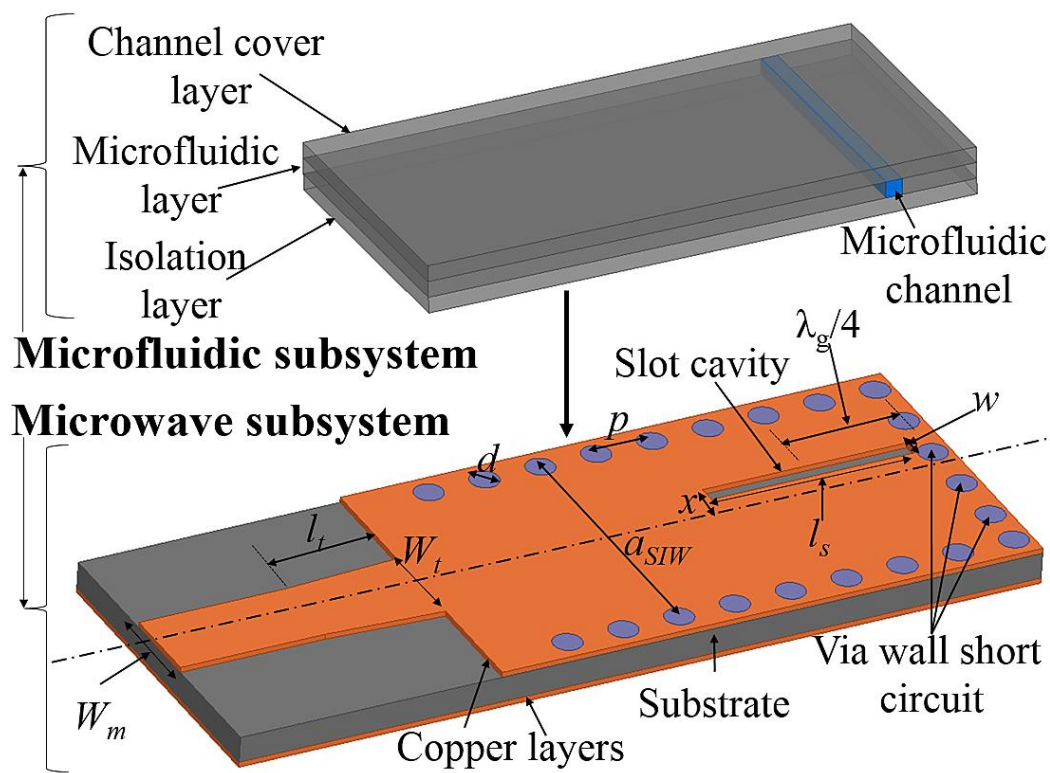


Figure 4.1 3D drawing of SIW waveguide integrated with a single slot antenna and microfluidic subsystem

Table 4.1 Summary of the design parameters

Parameter	Description	Length (mm)
d	Via post diameter	0.5
p	pitch	0.8
a_{SIW}	SIW width	15.4
b	SIW height	1.575
l_s	Slot length	11.7
w	Slot width	0.5
x	Displacement from centre of SIW to centre of slot	1.85
l_t	Microstrip taper length	6.7
W_t	Microstrip taper width	5.4
W_m	50-Ω microstrip width	4.62

The SIW design procedure follows the steps given in [54]. The important design consideration is that the pitch (p) is less than or equal to twice the vias post diameter (d) and that the post diameter is less than a fifth of the guided wavelength (λ_g) as given in (4.1). Under this condition the field leakage can be negligible and the performance of the SIW structure is similar to the conventional rectangular waveguide. The SIW width (a_{SIW}) is then the equivalent dielectric waveguide width (a_e) given by (4.2), where a_{RWG} is the width of a conventional rectangular waveguide and ϵ_r is the relative permittivity of the substrate.

$$d < \frac{\lambda_g}{5} \text{ and } p \leq 2d \quad (4.1)$$

$$a_{SIW} = \frac{a_{RWG}}{\sqrt{\epsilon_r}} \quad (4.2)$$

Rogers RT/Duroid 5880 substrate was used to implement the SIW structure, with a dielectric constant of 2.2 and a loss tangent of 0.0009 at 10 GHz. RT/Duroid 5880 has low moisture absorption, very good chemical resistance and offers the lowest electrical loss for reinforced Polytetrafluoroethylene (PTFE) material making it a good substrate for the dielectric encapsulating the liquid [20]. The optimum design parameters of the SIW waveguide are summarized in Table 4.1.

A single slot antenna is well sufficient to achieve highly accurate tracking of the resonant frequency changes and the return loss variations when different types of liquid samples are encapsulated in the channel above the antenna slot. The slot length (l_s) and the slot displacement from the SIW center (x) in Fig. 4.1 are optimized to obtain the lowest voltage standing wave ratio

(VSWR). The displacement of the slot from the center of the SIW plays a critical role in the design, since it directly impacts on the effective resonant slot conductance. The displacement is calculated by using the Stevenson formula [55] that gives the effective resonant slot conductance.

$$g(x) = g_o \text{Sin}^2 \left(\frac{\pi x}{a_{SIW}} \right) \quad (4.3)$$

$$g_o = (2.09 a_{SIW} \lambda_g / b \lambda_o) \text{Cos}^2 (\lambda_o \pi / 2 \lambda_g) \quad (4.4)$$

where $g(x)$ ($=G_s/G_{SIW}$) is the normalized conductance of a resonant longitudinal shunt slot, g_o is a constant, λ_g is the guide wavelength, λ_o is the free-space wavelength, x is the slot displacement from the center of the guide and a_{SIW} and b are the waveguide width and height [56]. G_s is the slot conductance and G_{SIW} is the guide characteristic conductance. The slot length (l_s) is impacted by the permittivity of the dielectric filling the waveguide. This was calculated by (4.5), [57]:

$$l_s = \frac{\lambda_o}{\sqrt{2(\epsilon_r + 1)}} \quad (4.5)$$

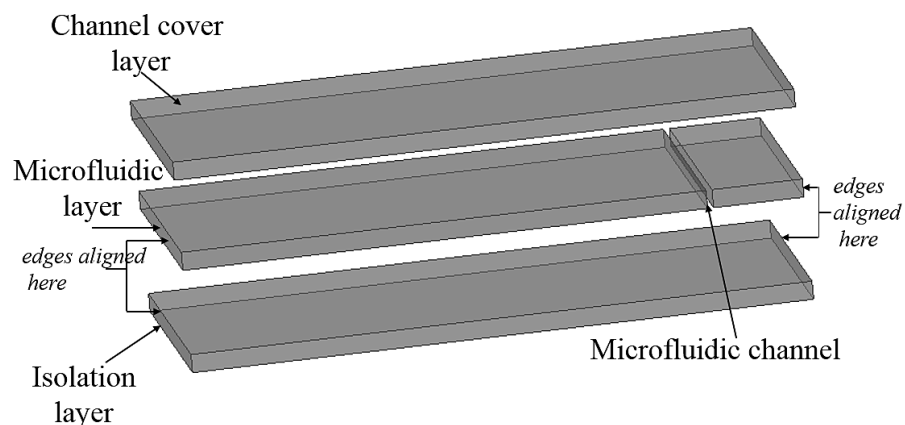


Figure 4.2 Precisely cut Microfluidic subsystem layers aligned at the edges

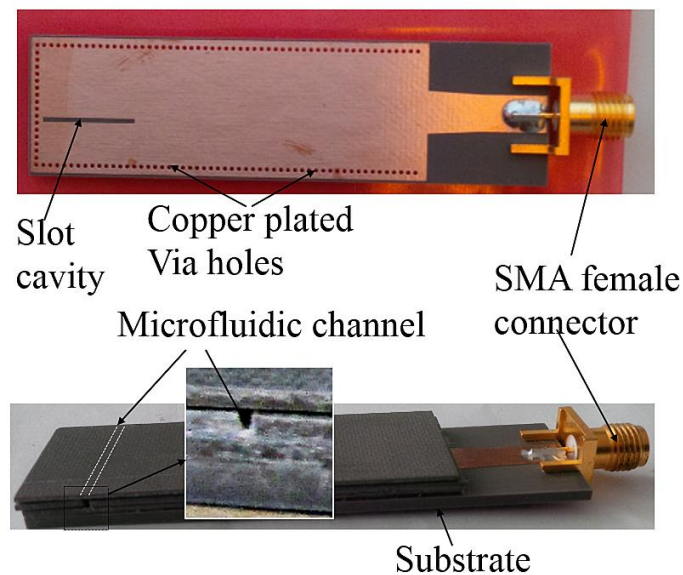


Figure 4.3 Fabricated prototype, before (top) and after (bottom) mounting the microfluidic subsystem

For the design frequency of 10 GHz and substrate relative permittivity of 2.2, the calculated slot length is 11.86 mm. The slot length was further optimized with HFSS to 11.7 mm in order to achieve the lowest VSWR.

A tapered microstrip transition from a 50- Ω input microstrip line to the SIW was designed to achieve good matching over the whole operation band of the SIW [58]. The tapered microstrip line converts the TEM propagation mode of the microstrip to the TE₁₀, which is the fundamental mode, in the SIW.

The position of the microfluidic channel is determined based on the design rule that the radiated EM near-field is maximum at the quarter-wavelength distance from the short-circuited end of the SIW. In this design, the microfluidic channel is located at 6.7 mm from the short-circuited end of the SIW, in order to achieve the best sensing accuracy. The microfluidic subsystem is made up of three layers, the isolation layer, the microfluidic

layer and the channel cover layer. All layers are precisely cut out using the LPKF 200 Protolaser machine in the laboratory. The three layers are aligned as shown in Fig. 4.2 for bonding. To ensure that the slot cavity is not in physical contact with the liquid sample under test, the isolation layer consisting of a low-loss dielectric substrate is bonded on top to cover the SIW antenna slot. The thickness of the isolation layer is 790 μm . However, adding a dielectric isolation layer on top of the slot results in a slight resonant frequency shift [59] : in this design from 10 GHz to 9.6 GHz. After integrating the isolation layer, the microfluidic subsystem is implemented on top by using another dielectric substrate containing a micro-channel. The height of the microfluidic channel is 790 μm , which equals the thickness of the substrate. Another dielectric substrate is then bonded on top to cover the microfluidic channel, ensuring the liquid is well encapsulated inside the microchannel. Epoxy bonding was used for all three substrate layers. All three dielectric substrates forming the microfluidic subsystem are implemented by using Rogers Duroid 5880. The width of the microfluidic channel is optimized by HFSS to 500 μm for the best sensing accuracy and sensitivity.

Fig. 4.3 shows the fabricated sensor prototype before (top) and after (bottom) integrating the microfluidic subsystem to the microwave SIW sensor, respectively.

4.3 Model analysis

An equivalent circuit model for the radiating area of the slot antenna was developed as shown in Fig. 4.4. It was developed by considering that because the slot interrupts the transverse currents of the SIW, the EM-wave

radiation is induced from the slot both in the upward direction into the isolation layer and microfluidic channel as well as in the downward direction into the SIW. Fundamentally, if the impedance or admittance attributed to the measured liquid can be calculated, it then means the relative permittivity of the liquid under test at the resonant frequency can be accurately determined.

This becomes clear when it is considered that the slot cavity represents a rectangular waveguide. Similarly, the isolation, microfluidic and channel cover layers can be seen as dielectric waveguide slabs. The material properties of the unpatterned isolation and channel cover layers is sufficiently provided by the manufacturer, i.e. the Rogers Duroid 5880. The microfluidic layer, on the other hand, is composed of a micro-fluidic channel, filled with the liquid under test, embedded into the Rogers Duroid 5880 substrate. This means that only the permittivity of the liquid under test is unknown and must be determined. Understanding this enables the relative permittivity of the liquid to be calculated using transmission line analysis of the conductance of the whole equivalent two-dimensional circuit model in Fig. 4.4, in relation to the measured resonant frequency and return loss.

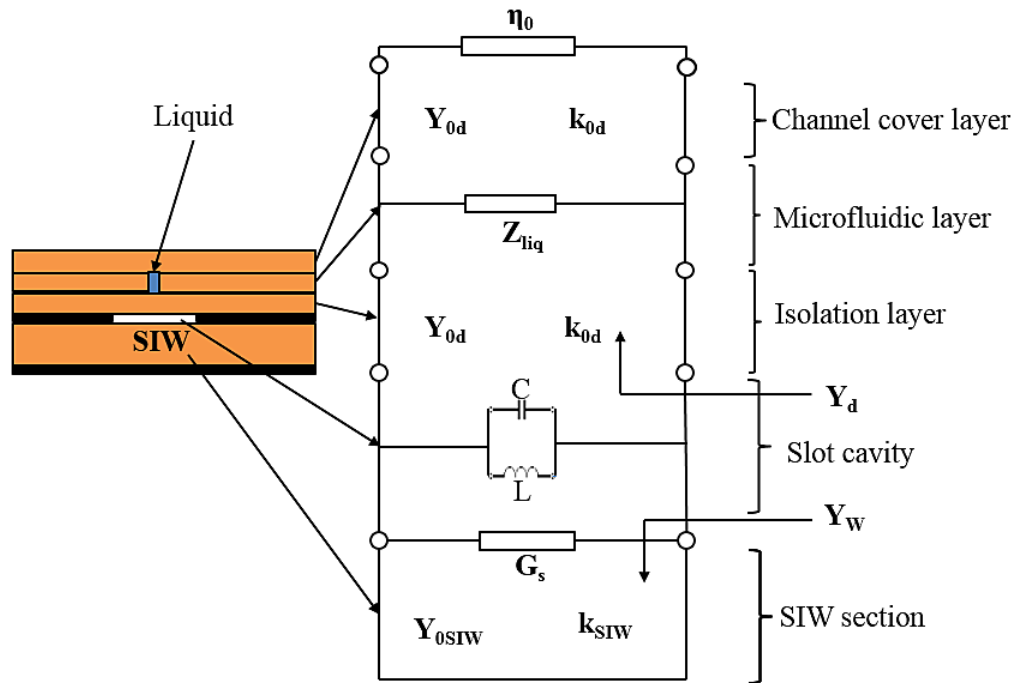


Figure 4.4 SIW Sensor radiating area equivalent 2-D circuit

The total conductance (G_t) of the equivalent circuit can be calculated as in [59] by:

$$G_t = Y_w + Y_d + G_s + j \left(\omega C - \frac{1}{\omega L} \right) \quad (4.6)$$

where G_t is the total conductance of the entire equivalent model, G_s is the resonant conductance due to the thin slot, with C and L being capacitance and inductance of the slot cavity. Y_w and Y_d are respectively the admittance seen from the slot looking into the SIW and also from the slot looking into the isolation layer. This implies that Y_d is the effective admittance due to the isolation layer, the microfluidic layer and the liquid channel cover layer.

Resonance occurs when the slot admittance presented to the SIW is real [55]. In [59] it was investigated that the conductor wall thickness introduces a resonant frequency shift but leaves the resonant conductance of the antenna

slot unaffected. The total conductance of the equivalent circuit can therefore be reduced to (4.7) at the resonance while still giving accurate results:

$$G_r = Y_w + Y_d + G_s \quad (4.7)$$

where G_r is the resonant conductance of the entire equivalent model. The slot resonant admittance, G_s , has already been defined in (4.3) and (4.4).

Assuming that the standing wave for the electric field across the slot is symmetrical, the return loss at the input port can be represented in the form of the equivalent shunt admittance (G_r/Y_{SIW}) as a result of the longitudinal slot in the broad wall of the waveguide [60]:

$$S_{11c} = \frac{\frac{G_r}{Y_{SIW}}}{2 + \frac{G_r}{Y_{SIW}}} \quad (4.8)$$

where Y_{SIW} is the characteristic admittance of the waveguide, which, in this case, is the equivalent characteristic admittance of the SIW, tapered transition and the 50- Ω microstrip. S_{11c} is the calculated reflection coefficient at the input port. The expressions of the admittance variables in Fig. 4.4 were developed as follows. From transmission line theory:

$$Y_w = -jY_{0SIW} \cot(k_{SIW}b) \quad (4.9)$$

where the characteristic admittance in the guide below the slot is given by

$$Y_{0SIW} = \frac{\beta_d}{k_0 \eta_0} \quad (4.10)$$

and $k_{SIW} = \frac{2\pi\sqrt{\epsilon_s}}{\lambda_0}$ with ϵ_s being the relative permittivity of the dielectric filling the SIW. β_d is the propagation constant in the dielectric given by:

$$\beta_d = \sqrt{\epsilon_s k_0^2 - \left(\frac{\pi}{l_s}\right)^2} \quad (4.11)$$

where l_s is the length of the slot cavity.

Y_d is equally calculated using the transmission line theory. This is done by considering the impedance due to the isolation layer and a combination of the microfluidic layer and the impedance due to the liquid channel cover layer.

Y_d can then be defined as:

$$Y_d = Y_{0d} \frac{1 + jZ_{eq}Y_{0d}\tan(k_{0d}h)}{Z_{eq}Y_{0d} + j\tan(k_{0d}h)} \quad (4.12)$$

where Z_{eq} is the total impedance seen looking into the microfluidic layer from the isolation layer, given in (4.13) and Y_{0d} (which in this case is the same as Y_{0SIW}) is the characteristic admittance of the isolation layer and k_{0d} is equal to k_{SIW} since the dielectric used in both cases has similar properties:

$$Z_{eq} = Z_{liq} \frac{Z_{0d} + jZ_{liq}\tan(k_{liq}h)}{Z_{liq} + jZ_{0d}\tan(k_{liq}h)} \quad (4.13)$$

where $Z_{liq} \left(= \frac{k_0\eta_0}{\beta_{liq}} \right)$ is the characteristic impedance due to the microfluidic layer, while $k_{liq} \left(= \frac{2\pi\sqrt{\epsilon_{eff}}}{\lambda_0} \right)$ is the propagation constant in the microfluidic layer. ϵ_{eff} is the effective permittivity, which is the permittivity as a result of the liquid under test and the dielectric forming the microfluidic channel given by Maxwell-Garnet relationship as

$$\frac{\epsilon_{eff} - \epsilon_{liq}}{\epsilon_{eff} + 2\epsilon_{liq}} = f \frac{\epsilon_s - \epsilon_{liq}}{\epsilon_s + 2\epsilon} \quad (4.14)$$

where ϵ_{liq} and ϵ_s are the relative permittivity of the liquid and the dielectric forming the microfluidic channel respectively, while f is the fractional volume occupied by the dielectric in the microfluidic layer. The Maxwell-Garnet model was used because the electric field is considered constant across the

mixture of the dielectric substrate and the liquid under test. The Maxwell-Garnet is also designed for small volume fractions of inclusions [61] and is easy to solve.

To calculate the characteristic impedance of the waveguide feed network, the three sections of the feed network, consisting of the SIW, tapered microstrip transition and microstrip feedline, are considered as a cascade as shown in Fig. 4.5.

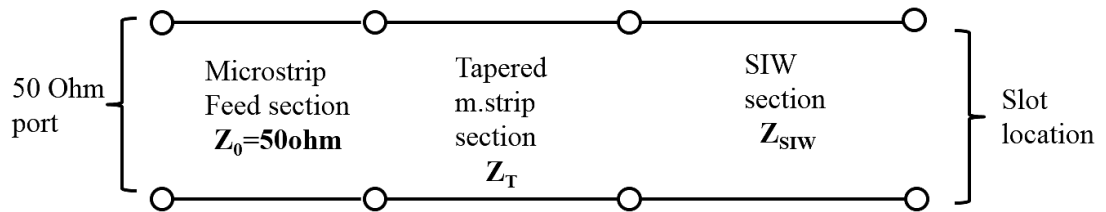


Figure 4.5 Equivalent model of the feed network

Each section of the feed network in Fig. 4.5 is designed using HFSS and their S-parameters are obtained. The S-parameters are converted to ABCD parameters so that the total ABCD parameters of the cascade can be obtained as:

$$[T_{in}] = [T_m] \cdot [T_t] \cdot [T_{SIW}] \quad (4.15)$$

where $[T_{in}]$ represents the total cascade ABCD parameters of the feed circuit with $[T_m]$, $[T_t]$ and $[T_{SIW}]$ representing the ABDC parameters for the 50- Ω microstrip, the tapered microstrip and the SIW sections, respectively. The ABCD parameters for the entire feed network are then converted back to S-parameters and used to obtain the equivalent characteristic impedance of the whole feed structure as:

$$Z_{SIW} = Z_0 \sqrt{\frac{(1+S_{11})^2 - S_{21}^2}{(1-S_{11})^2 - S_{21}^2}} \quad (4.16)$$

Substituting (4.3), (4.9) and (4.12) in (4.7) and then using (4.8) and (4.16), an expression for S_{11c} can be written with the effective relative permittivity of the liquid and dielectric forming the microfluidic subsystem as a variable.

The calculated S_{11c} is then iteratively compared with the measured S_{11m} to get the effective relative permittivity of the liquid and dielectric sample holder as shown in (4.17). In this particular case, the solve system, `fsolve`, of nonlinear equations in MATLAB was used, together with the developed MATLAB program, to numerically calculate the effective relative permittivity of the liquid at the resonant frequency. The known relative permittivity of the dielectric material forming the microfluidic subsystem was used as the initial value. Therefore, the relative permittivity of the liquid under test can be numerically calculated at the resonant frequency of the measurement using (4.14). The relative permittivity of various liquids and liquid mixtures characterized by the SIW sensor is compared to that measured by the Keysight 85070E dielectric probe sensor, under the same environment control. The measurement result comparisons are shown in Section 4.4.

$$f(\epsilon_{eff}) = [Re(S_{11m} - S_{11c}); Im(S_{11m} - S_{11c})] \quad (4.17)$$

4.4 Measurement results

4.4.1 Measurement setup, sensor calibration and standard measurement

The liquid under test was, prior to each measurement, injected into the microfluidic channel using a 100 μl syringe with one end of the microfluidic channel well capped. The liquid was let to overflow at the inlet before the microchannel inlet was capped to ensure complete liquid filling. When the microchannel was completely filled by the liquid under test without any air gap or bubble, the liquid inlet of the microchannel was then sealed. The S-parameter measurement was done by using the Keysight E8361A Network Analyzer. One-Port reflection calibration was performed using the Keysight Electronic Calibration (ECal) N4691-60006 module prior to the measurement. All liquids were maintained at 25°C by using a warm water beaker that was maintained at 25°C.

Three sample materials, which are air, Methanol and DI water, were measured and characterized. Air was measured in order to calibrate the measurement for an empty microfluidic channel, while the other two materials had their respective liquids filled in the channel.

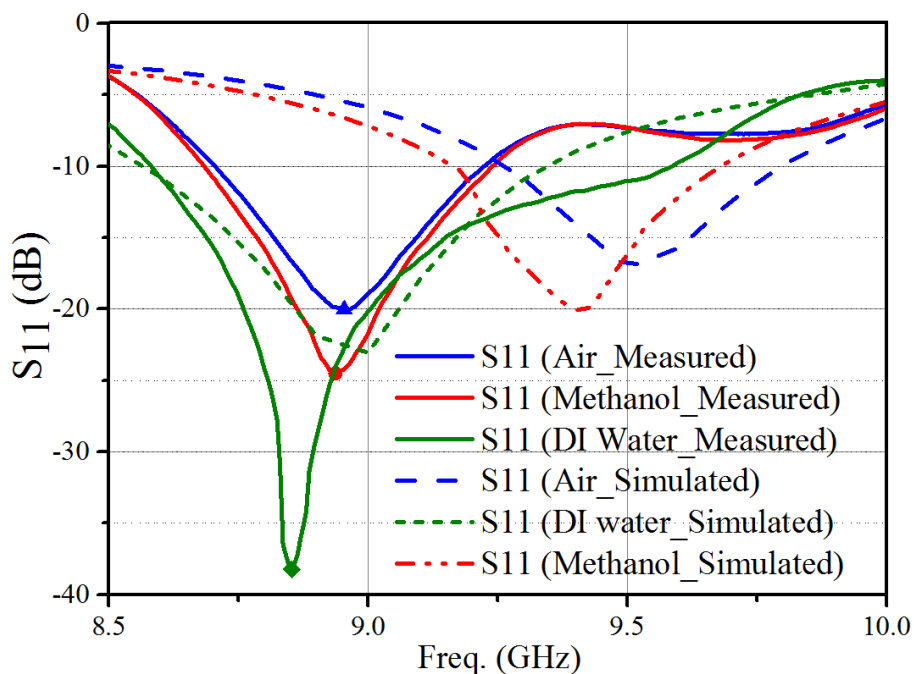


Figure 4.6 S_{11} plot for simulated and measured Air, Methanol and DI water samples

Fig. 4.6 shows that with the empty, air-filled, microfluidic channel, the measured resonant frequency of the SIW sensor was 8.96 GHz with a return loss of 20.02 dB. With methanol and DI water samples, the resonant frequency was 8.94 GHz with a return loss of 24.51 dB and 8.85 GHz with a return loss of 38.21 dB, respectively. A resonant frequency shift of 110 MHz was observed between DI water and air (empty channel), while a shift of 20 MHz was observed between methanol and air.

The resonant frequency shifts between the empty channel and liquid-filled channel were significant and; therefore, it was clear that accurate characterizations and discriminations between each different liquid material under test could be obtained.

For all simulations, HFSS used the default meshing setting with the lambda target set at 0.3333. HFSS then used auto-adaptive meshing based on the

fields for it to obtain the final mesh. Fig. 4.6 shows that the simulated results are shifted in frequency and return loss because the epoxy effect was not included in the simulation, difference in conductor loss used, and also the simulation uses approximated properties for the samples under test. The measured values are used for subsequent calculations.

4.4.2 Quantification measurement of liquid mixture

The SIW sensor demonstrated liquid quantification by measuring liquid mixtures of DI water and methanol with methanol to DI water composition varying from 0-100 % by volume. An increment of methanol volume by 20 % corresponding to an equal decrease of DI water by volume for each measurement step was conducted. Zero percent methanol constituent in the liquid mixture indicated 100 % DI water. Fig. 4.7 shows the measurement result indicating the reflection coefficient (S_{11}) of the different liquid mixtures.

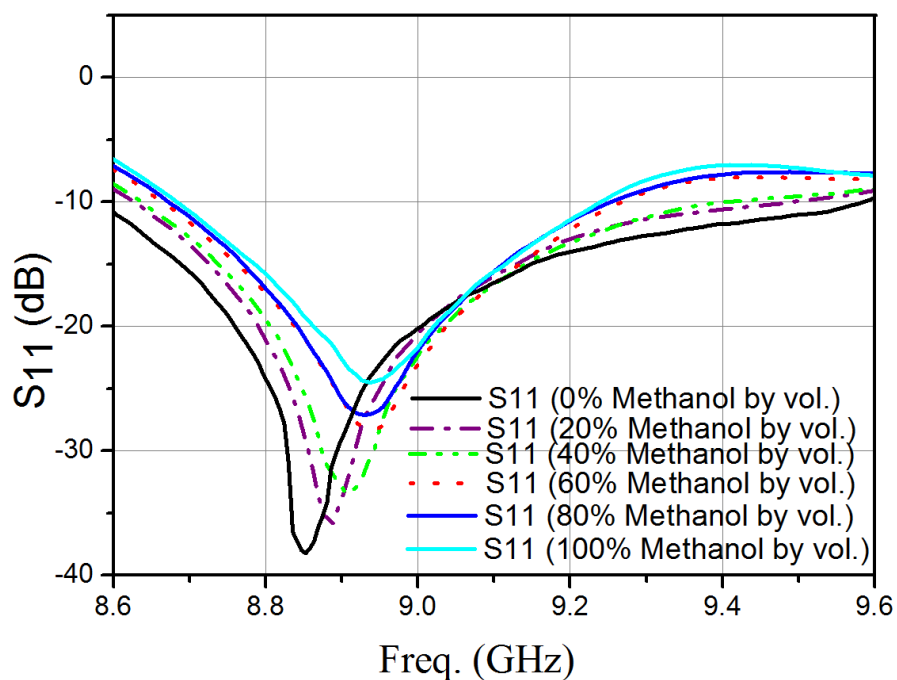


Figure 4.7 Measured S_{11} plot for Methanol and DI water mixtures

Varying mixture concentration gives an equivalent change in resonant frequency and return loss. This change is mostly because a high loss liquid has more perturbation effect on the radiated near-field than a lower loss liquid and hence having a lower resonant frequency. Therefore, by starting with 100 % methanol and decrement each measurement step downwards by 20 % by volume, it was observed that the resonant frequency correspondingly shifted downwards as more water by volume dominated the test sample.

This is illustrated in Table 4.2 and Fig. 4.8, with values for the mixture characterization model, developed by a fitting curve method, included. This characterization model therefore embodies the behavior of this particular mixture and can be subsequently be used to determine the composition of any given DI water – methanol mixture.

Table 4.2 Deionised water-methanol mixture measurement

Frequency (GHz)	Methanol fractional volume (measured)	Methanol fractional volume (Model)	Percentage difference
8.86	0	0.00067215	0
8.88	0.2	0.20378764	1.89382
8.90	0.4	0.39054383	2.364042
8.92	0.6	0.61892344	3.153907
8.93	0.8	0.78270568	2.16179
8.94	1.0	1.0047337	0.47337

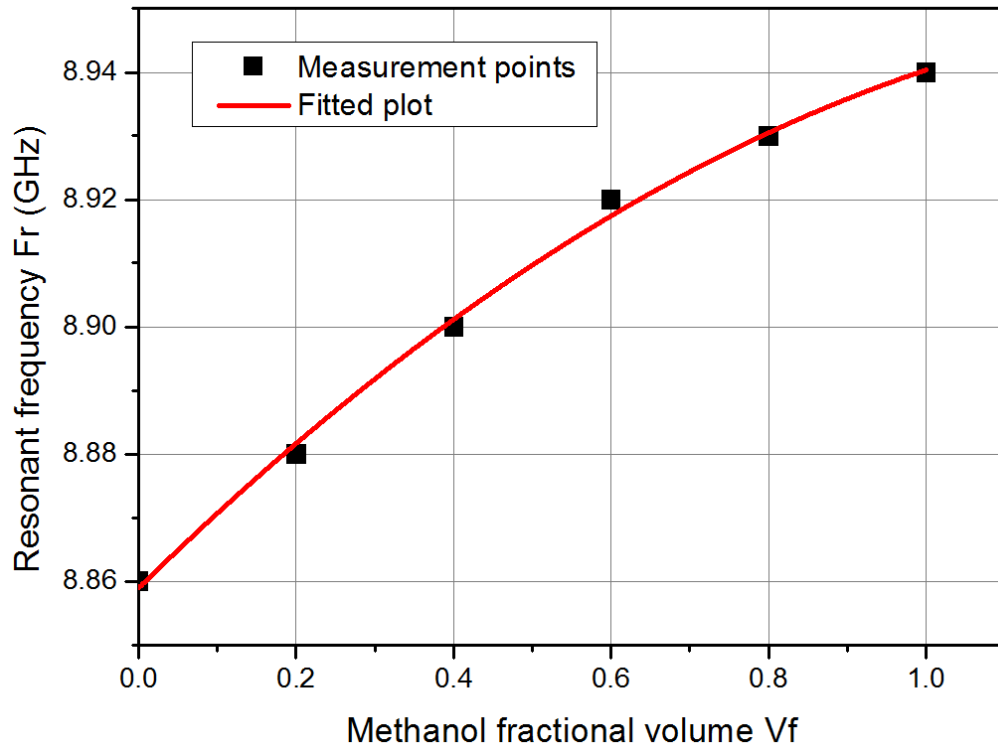


Figure 4.8 Measured resonant frequency against Methanol fractional volume

The equation characterizing the mixture measurement is given as

$$F_r = 8.85893 + 0.12161V_f - 0.04018V_f^2 \quad (4.18)$$

where V_f is the fractional volume of methanol and F_r is the measured resonant frequency. This means that for a deionised water – methanol mixture, by only using (4.18) and the measured resonant frequency, the methanol percentage in the mixture can be calculated.

4.4.3 Relative permittivity measurement

Using the software program developed from the mathematical model in section 4.3, it was possible to determine the relative permittivity (real part of the complex permittivity) of the liquid under test. This was achieved by solving iteratively the equation given in (4.17), with the Matlab program illustrated in Appendix B . The relative permittivity was calculated for the DI

water and methanol mixtures mentioned in the preceding subsection. These liquids and liquid mixtures were also measured using the Keysight 85070E dielectric probe under the same environment control and condition. As shown in Table 4.3, the results showed good agreement between the SIW sensor and the commercial probe, with the percentage difference between the two sensor devices varying from 0.4 % to 3 %. However, for the SIW sensor, only $7 \mu l$ of the sample liquid was required for an accurate measurement while the commercial probe required more than $100 ml$ for the same accuracy.

Table 4.3 Relative permittivity measurement of methanol/DI-water mixture using SIW slot antenna and the Keysight dielectric probe

Test sample (by volume)	Freq. (GHz)	Relative Permittivity (this work)	*Relative permittivity (Keysight probe)	% diff.
100%Methanol	8.94	8.58	8.37	2.44
80% Methanol	8.93	11.92	11.63	2.43
60% Methanol	8.92	23.55	22.86	2.93
40% Methanol	8.90	34.54	34.39	0.43
20% Methanol	8.88	48.67	48.44	0.47
100% DI water (0% methanol)	8.85	66.12	65.67	0.68

*Measured using Keysight 85070E probe sensor.

4.4.4 Sensor sensitivity

Simulations were performed to analyse the sensitivity of the sensor. Three test samples with relative permittivity of 10, 10.01 and 10.1 were used, low ϵ'_r values were used to prove good sensitivity for low relative permittivity liquids. The sensitivity of the sensor was approximated to be $\pm 0.01 \epsilon'_r$ or $\pm 1\%$ of ϵ'_r as shown in Fig. 4.9, where there is no significant shift in frequency with sample ϵ'_r difference of 0.01, but a clear difference is seen when the sample ϵ'_r has a difference of 0.1.

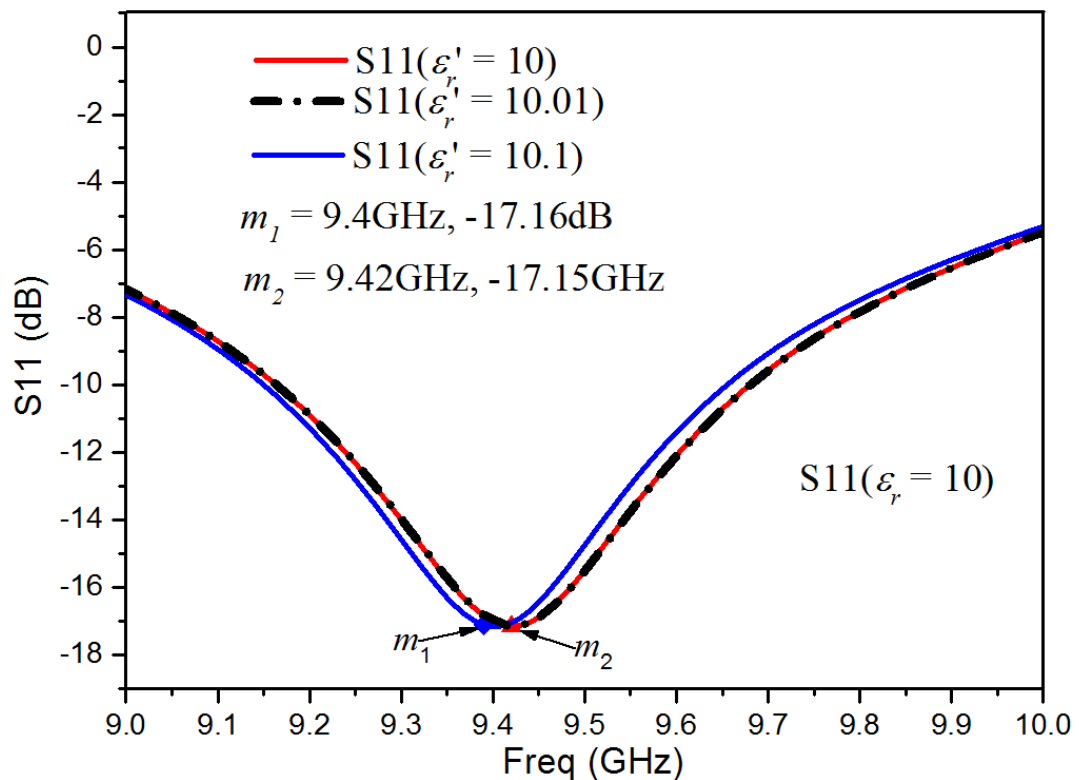


Figure 4.9 Sensor sensitivity simulations

In Table 4.4, key figure-of-merit and parameter comparisons between this work and the state-of-the-art [26] and [62-64] are presented.

Table 4.4 Key parameter comparison of measurement of this work and other work

Key Parameter	[26]	K.D.P***	[62]	[63]	[64]	This work
Relative permittivity (ϵ'_r) of deionised water	Reported S_{21} results	65.67	63	63.5	66.5	66.12
Liquid volume	<i>nl</i>	100 <i>ml</i>	1.8 <i>ml</i>	1.16 <i>ml</i>	Not indicated	7 μ <i>l</i>
Freq. for DI water measurement (GHz)	17.9-19.34	8.85	9.7	9.7	8.5	8.5
Fabrication complexity	Moderate	Moderate	Moderate	Moderate	N/A**	Low
Lab-on-substrate suitability	Yes	No	No	No	N/A	Yes
Characterisation method	Resonance	Reflection	Transmission	Transmission	N/A	Resonance
Permittivity measurement range	20 – 40*	Not limited	Not limited	Not limited	Not limited	Not limited
Planar structure	Planar	Non-planar	Non-planar	Non-planar	N/A	Planar
Measurement setup	Non-invasive and contactless	Non-invasive	Non-invasive	Non-invasive	N/A	Non-invasive and contactless
Fabrication	Cleanroom	Standard machining	Standard machining	Standard machining	N/A	Standard PCB
Design complexity	Complicated	Moderate	Moderate	Moderate	N/A	Moderate

*Limited to indicated range because of the predictive model

**Results obtained using developed interpolation function

***K.D.P (Keysight Dielectric Probe)

4.5 Summary

The developed microwave microliter sensor in this work has shown some of its potential range of usage leading to accurate quantification of liquid mixtures and further liquid characterization through measurement of the relative permittivity. The accuracy in measurement was enhanced by the resonance operation of the sensor. This ensured that with only $7 \mu l$ of the liquid, sufficiently accurate results were obtained. Furthermore, the developed model based on a dielectric covered waveguide fed slot antenna enhanced confidence in the obtained results. The quantification measurements of DI water and Methanol mixtures with methanol varying in increments of 20 % by volume gave a good indication of how this sensor could be applied. Equally the measured relative permittivity of the liquids affirmed the universal nature of the characterization range, therefore lending this sensor to potentially vast applications. This microwave microliter sensor consequently has potential in the characterization of biological liquids.

Chapter 5

Sub-millimetre Wave Sensor for Dielectric Material

Characterisation

5.1 Introduction

This chapter describes the design of a sub-terahertz sensor for solid dielectric material characterisation. The importance of this work was twofold, namely to offer an alternative accurate characterisation method for the W-band where dielectric properties of materials are not readily available and to lay the foundation for a method for calculating thin-film material thickness. Thin-film material thickness calculation has proved to be a challenge especially for substrates spun on glass substrates. Non-invasive, high frequency material characterization applications, demand that accurate devices are used. Resonant structures with high quality factor have proved to be sufficiently accurate when used in this regard. This is supported by the fact that the higher the quality factor, the more measurable and trackable are the small changes in material properties. One such device is the split-ring resonator (SRR). The last few decades have seen advancement in the design of split-ring resonator devices leading to high performance microwave devices with application mostly in left-handed metamaterials (LHMs) [65-69], filters [70-72] and material characterization sensors [73-76]. Apart from offering high performance, split-ring resonators together with their counterpart, the complementary split-ring resonator (CSRR), offer compact

and low radiation loss systems and good control of the electrical characteristics.

CSRRs respond to the electric field as opposed to the SRR that couples the magnetic field. In design terms the CSRR has a ring made of a dielectric on the conductor while the SRR has a metallized ring on a dielectric. Both forms of the ring resonator have attracted a lot of interest in sensing applications because of the relatively high quality factor type of resonators that they are able to create. In [76] a planar split-ring resonator based RF biosensor was developed for label-free detection of biomolecules, specifically the prostate specific antigen. This ability to detect such a sensitive material has motivated this research to characterize dielectric materials at high millimetre wave frequencies or sub-terahertz. Furthermore characterization information of most materials in this band is very limited.

In this chapter, a resonant sub-terahertz dielectric characterization sensor operating at 100 GHz is presented. The use of CSRRs with their inherent gap reduces the resonant frequency of the structure. Furthermore having the design at sub-terahertz guarantees that the sensor is compact regardless of using a waveguide as the transmission line of choice. Using a waveguide for the transmission line ensures that the design benefits from it having high power handling and low radiation loss while still offering a competitive compact structure. This chapter primarily focuses on the design and accurate characterization of sub-terahertz applicable dielectric materials. This is motivated by the inadequately available reference data in this region. For the first time a sensor with three functions in one is presented. These functions are namely that: 1) the sensor can operate as a resonant sensor

offering dielectric characterization at a single frequency for applications requiring fast and accurate properties determination. This is achieved by using a sliding short at the output port, effectively making the structure a one port resonant structure, 2) the sensor can also be used for broadband measurements, with bandwidth of 6 GHz, to characterize dielectric materials. This is achieved by removing the sliding short at the output port, effectively having a two port transmission line structure and 3) the sensor can also work as a tuneable sensor offering resonant measurements at predetermined sliding short positions with known response behaviour. Having designed the sensor in this three-prone way validated its operation and measurement accuracy like never reported before. The extraction of the material dielectric properties was achieved through a developed model analysis made possible using the Ansoft finite element software (HFSS). Through this model the bounds for the materials that could be measured by the sensor were determined. The sensor was modelled for measurement of materials with relative permittivity values up to 5 and loss tangent up to 0.01. This covers most common low loss materials that find application at sub-terahertz frequencies.

5.2 Sensor design and fabrication

The CSRR in this work is patterned on the broad-wall of an air filled WR-10 waveguide. Fig. 5.1 (a) shows a schematic of the top view of the CSRR patterned on a WR-10 waveguide with all parameters, this is not drawn to scale however. In Fig. 5.1 (b) the equivalent lumped element circuit of a double CSRR is shown.

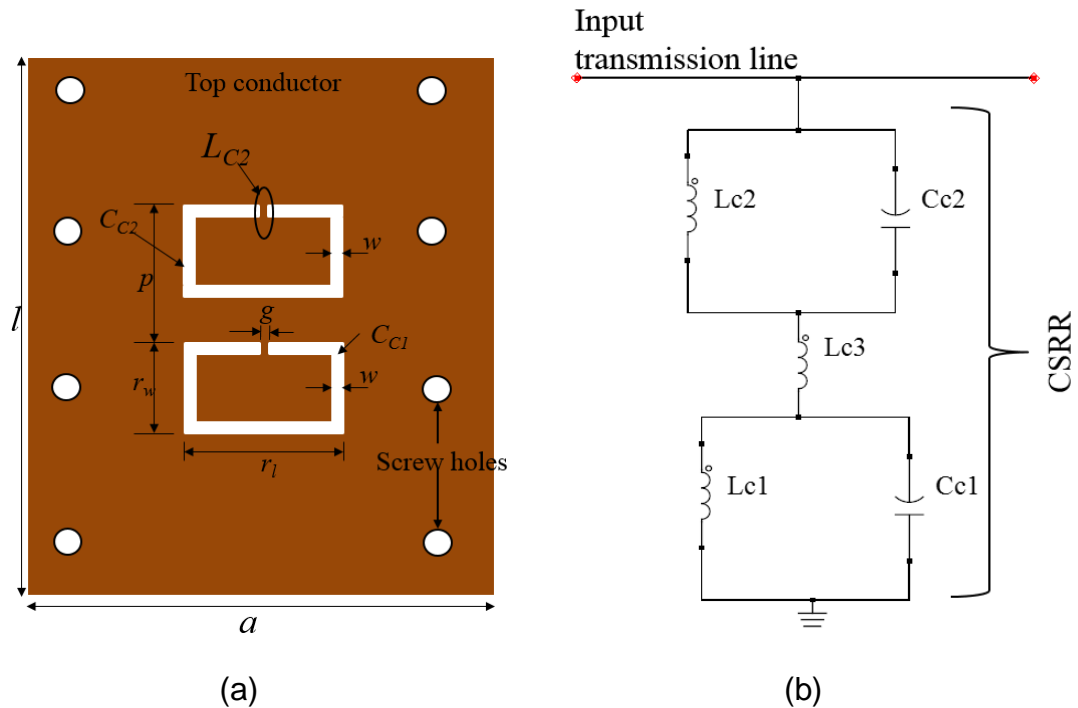


Figure 5.1 (a) CSRR schematic in the broad-wall of a rectangular waveguide (b) CSRR equivalent lumped element model

The inductor L_{C3} represents the mutual inductance between the two CSRRs separated by the distance $(p-r_w)$ in Fig. 5.1 (a). The metal plate in the middle of the each ring creates capacitance (C_{C1} and C_{C2}) with the one outside the ring that is determined by the circumference of the inner metal ring as well as the size of the gap between the two metal sections, w . The inductance, contributed by L_{C1} and L_{C2} , is determined by the size of the metal strip left to hold the ring in place, noted by g and w . The values of C_c (total capacitance loading the line) and L_c (total inductance loading the line) determine the resonant frequency (5.1), with the magnitude of the return loss being affected by the loading of the transmission line by the CSRR:

$$f_R = \frac{1}{2\pi\sqrt{C_c L_c}} \quad (5.1)$$

where C_c is a combination of C_{c1} and C_{c2} , and L_c is a combination of L_{C1} , L_{C2} and L_{C3} .

All the parameters in Fig. 5.1 are defined in Table 5.1 for this design operating at 100 GHz. Two CSRRs are used to increase the E-field interaction with the material under test as the measurements are surface based.

Table 5.1 Summary of the design parameters

Parameter	Description	Length (mm)
a	Waveguide width	2.54
l	Waveguide length	30
p	Pitch	1.5
r_l	Ring length	1.81
r_w	Ring width	1.0
w	Slot width	0.17
g	Gap width	0.23

The fabricated prototype is shown in Fig. 5.2 with all the components used to make the device. To enable the patterning of the CSRRs, the WR-10 waveguide was split in the H-plane, whereby the full waveguide groove was machined on the bottom block while the top layer, that acted as the conductor cover, had the two CSRRs patterned into it. Creating the device this way, adds reusability, by being able to structure different kind of devices on the top conducting cover. Sufficient screw holes were provided for to ensure that the contact when assembled was as close as possible to a completely enclosed waveguide in one block. The waveguide was made using copper as seen in Fig. 5.2.

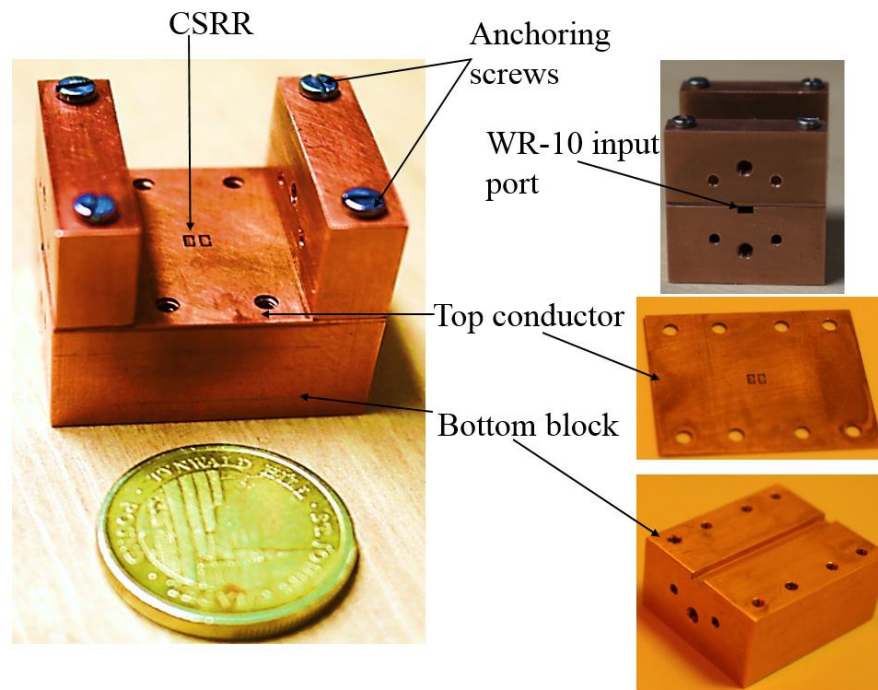


Figure 5.2 Fabricated prototype, showing assembled structure and the components of the structure

This design uses two scenarios, one where the device works as a resonant sensor and another where it works as a transmission line sensor. To make the device a resonant sensor with sufficient field radiation from the CSRR, a contacting sliding short was used at the output port. The CSRR was designed at $3\lambda_g/4$ guided wavelength at 100 GHz from the short circuit position. To this end, the total length of the sliding short was 12.45 mm. The requirement for making a contacting sliding short is that it is made from a low loss metal and is able to make direct contact with one of the broadside waveguide walls. The sliding short was designed as given in [77], where periodic sections of low-Z and high-Z spaced at $\lambda_g/4$ are used to ensure a close to perfect short circuit, shown in Fig. 5.3. In [77] it was established that the sliding short does not need to touch the side walls of the waveguide, but only the bottom of the broad wall when created as described above.

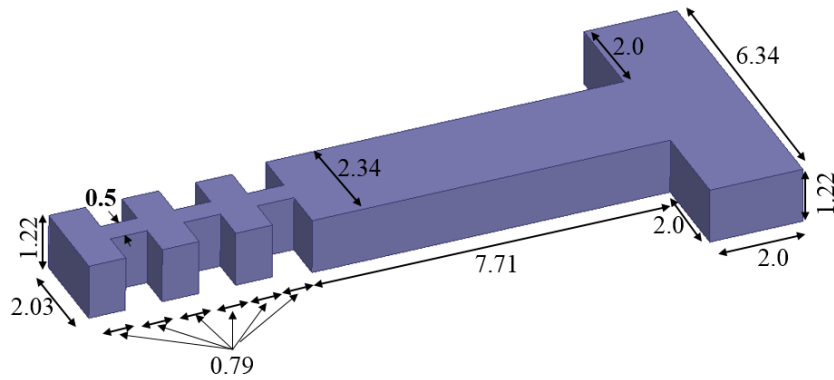


Figure 5.3 Contacting sliding short

In Fig. 5.4, a full setup of the transmission method measurement is shown as well as the resonant measurement setup. The transmission method setup is the case where the sliding short is removed and the sensor essentially works as a 2-port device, with SUT interaction with the sensor still being through the radiated field from the CSRR. In the resonant method setup as can be seen, the sliding short is inserted at port 2 to essentially create a one port system. The material under test was secured as shown in Fig. 5.4 to ensure that the air gap effect was minimised as much as possible.

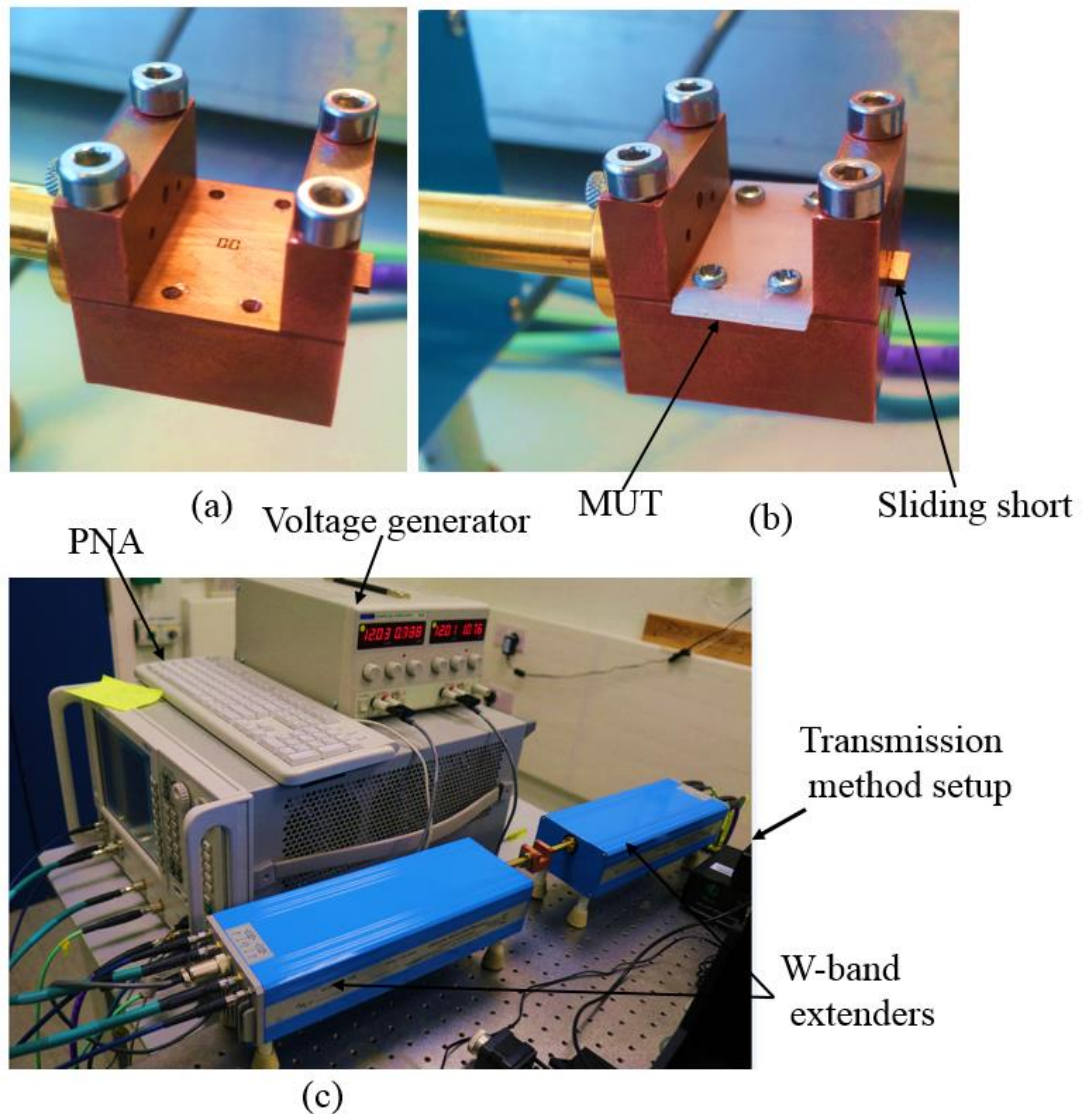


Figure 5.4 Measurement setup (a) with sensor working as a resonant sensor (b) resonant setup with MUT (c) transmission method setup

5.3 Complex permittivity extraction model

5.3.1 Resonant method material permittivity extraction

The case where the device is used as a resonant sensor is that when the sliding short circuit is inserted at port 2, pushed in up to $3\lambda_g/4$ for maximum radiation. The complex permittivity extraction model for the resonant method starts with the analysis to establish the bounds of operation of the sensor. This analysis model was created by using hypothetical materials and

simulating the full design using HFSS. Air was used as the measurement standard in this analysis. By simulating the design with hypothetical materials with relative permittivity (ϵ_r') ranging from 1 to 5 and loss tangent ($\tan \delta$) varying from 0 to 0.01, the relationship between the resonant frequency and return loss magnitude with the complex permittivity was developed for materials with properties in this range. A similar method was used in [26], where relative permittivity and loss factor were used as varying parameters. The difference in this model is that the relationship between both resonant frequency and S_{11} magnitude at the resonant frequency for both scenarios, when one variable is varied and the other kept constant, is used fully to yield the complex permittivity of the solid material being measured. In [26] this was not developed fully to the point of being used.

In Fig. 6(a) and 6(b) the resonant frequency and minimum magnitude S_{11} response with varying ϵ_r' and $\tan \delta$ respectively is shown. In summary this model is developed as follows:

1. Vary ϵ_r' from 1 – 5 (with $\Delta\epsilon_r'$ equal to 1) while keeping $\tan \delta$ constant through the values 0, 0.0005, 0.005 and 0.01. Simulations were done using HFSS through each value of ϵ_r' while keeping $\tan \delta$ constant.
2. Vary $\tan \delta$ from 0 to 0.01 while keeping ϵ_r' constant through all values from 1 to 5.
3. Use air as the standard, $\epsilon_r' = 1$ and $\tan \delta = 0$.
4. Develop the following relationship:

$$\Delta f_r = \frac{1\Delta f_r}{2\Delta\epsilon_r'} \Delta\epsilon_r' + \frac{1\Delta f_r}{2\Delta\tan\delta} \Delta\tan\delta \quad (5.2)$$

which can be simplified further as

$$\Delta f_r = R_1 \Delta \epsilon_r' + R_2 \Delta \tan \delta \quad (5.3)$$

where R_1 and R_2 express the relative value of the resonant frequency change in relation to the relative permittivity and the loss tangent respectively.

5. A similar relation was developed for the magnitude of S_{11} as shown below.

$$\Delta S_{11} = \frac{1\Delta|S_{11}|}{2\Delta\epsilon_r'} \Delta\epsilon_r' + \frac{1\Delta|S_{11}|}{2\Delta\tan\delta} \Delta\tan\delta + K \quad (5.4)$$

which again is simplified to

$$\Delta S_{11} = R_3 \Delta \epsilon_r' + R_4 \Delta \tan \delta \quad (5.5)$$

Where R_3 and R_4 represent the relative change of the magnitude of S_{11} to the change in ϵ_r' and $\tan \delta$ respectively.

The constants R_1 , R_2 , R_3 and R_4 are established through the simulations in step (1) and (2). Average values are used for the change in resonant frequency as well as the change in magnitude of S_{11} in respect to those of the measurement standard, air in this case.

Table 5.2 Calculation of R_1 and R_3 values

$\tan \delta$	R_1 (GHz)	R_3
0	4.785	-0.2809
0.0005	4.785	-0.2888
0.005	4.75	-0.2852
0.01	4.66	-0.2806
	<i>Mean $R_1 = 4.745$</i>	<i>Mean $R_3 = -0.28592$</i>

Table 5.3 Calculation of R_2 and R_4 values

ϵ_r'	R_2 (GHz)	R_4
1	0	-0.61713
2	-100	1.86503
3	-400	0.93376
4	-433.33	-1.2483
5	-500	-2.6194
	<i>Mean $R_2 = -286.66$</i>	<i>Mean $R_4 = -0.56202$</i>

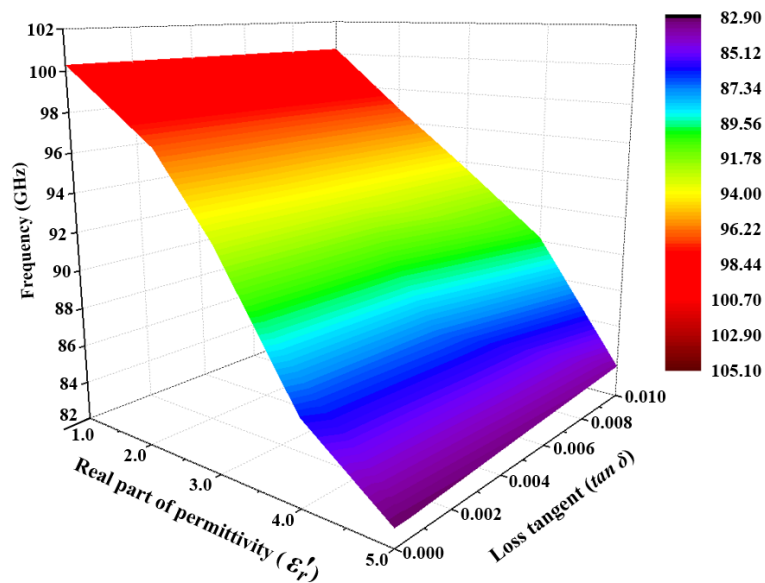


Figure 5.5 3D plot of resonant frequency against relative permittivity with loss tangent kept constant through values 0, 0.0005, 0.005 and 0.01

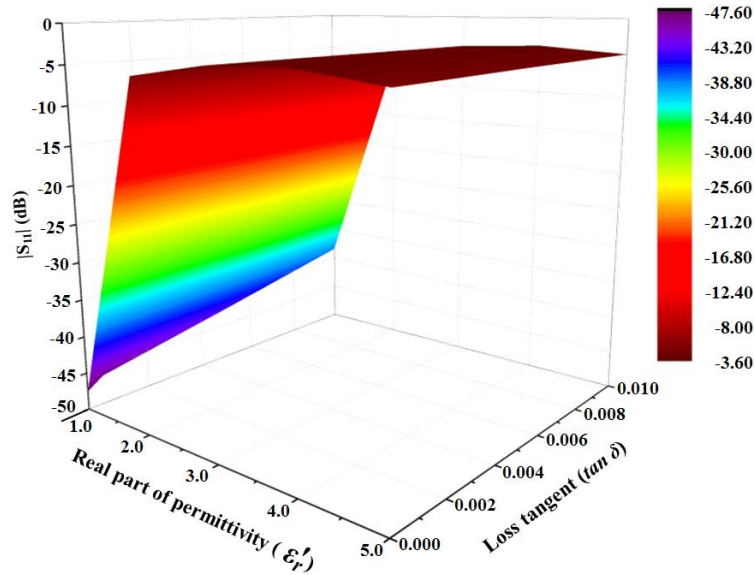


Figure 5.6 3D plot of S_{11} against loss tangent with relative permittivity kept constant through the values 1, 2, 3, 4, and 5.

From Fig. 5.5, it is clear to see that the change in resonant frequency is influenced more by the relative permittivity rather than the loss tangent. With the loss tangent maintained constant, the maximum resonant frequency change is 17.4 GHz, while the maximum resonant frequency change as a result of varying the loss tangent is only 4 GHz. Using the analysis from Fig. 5.5 and table 5.2 and table 5.3, (5.3) becomes

$$\Delta f_r = 4.745\Delta\epsilon_r' - 286.66\Delta\tan\delta \quad (5.6)$$

Similarly using Fig. 5.6 and Table 5.2 and Table 5.3, (5.5) becomes

$$\Delta s_{11} = -0.28592\Delta\epsilon_r' - 0.56202\Delta\tan\delta \quad (5.7)$$

From (5.6) and (5.7) and using air ($\epsilon_r = 1$, $\tan\delta = 0$) as the reference, the dielectric properties of the materials under test can be extracted.

5.3.2 Transmission method material permittivity extraction

In the next stage of the measurements, the sliding short was removed, hence creating a 2-port device for broadband material characterization. The same materials as in section 5.3.1 were measured, namely PTFE, PMMA and HDPE. The analysis required two standards for accurate results to be obtained. The two standards used were air and PTFE. PTFE was chosen because its response is steady through the whole band of operation. This was confirmed using the Keysight free space method. Measured values of PTFE using the Keysight free space method were used for the second standard. The measurement had four steps as follows:

1. Measure the full 2-port S-parameters with nothing loaded on the CSRR, i.e. air measurement standard.
2. Measure the full 2-port S-parameters response with the PTFE securely fixed to the CSRR face. This was the second and final standard.
3. Measure the SUT in a similar way as was done for PTFE.
4. Using the developed matlab code obtain the relative permittivity of the SUT. The code was based on fitting a 3D data set comprising of the measured S_{21} parameters of the standards and the known relative permittivity of the standards as shown in Fig. 5.7.

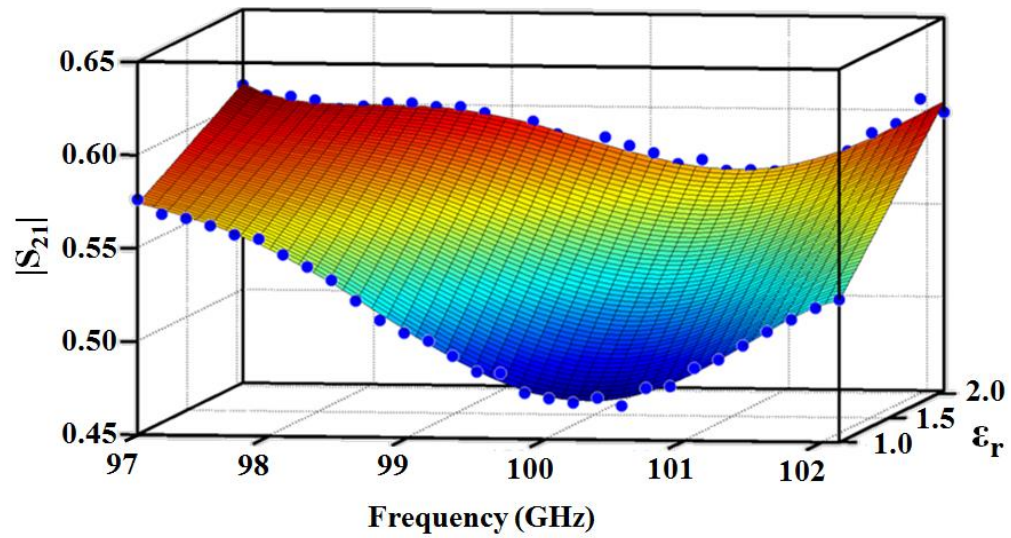


Figure 5.7 3D fitted curve to S21 measurement standard

From the fitted curve, a relationship was developed that was used to subsequently extract the relative permittivity of any measured SUT as follows:

$$\epsilon_r' = \frac{|S_{21}| - p_1 - p_2 f - p_3 f^2 - p_4 f^3 - p_5 f^4 - p_6 f^5}{p_7 + p_8 f + p_9 f^2 + p_{10} f^3 + p_{11} f^4} \quad (5.8)$$

where the coefficients are defined as shown in Table 5.4 for the three materials measured, f is in GHz and $|S_{21}|$ is in magnitude form:

Table 5.4 3D fitted curve coefficients for 3 materials

Parameter coefficient	PTFE	PMMA	HDPE
p_1	4.412184×10^6	6.097935×10^6	3.771760×10^6
p_2	-2.243027×10^5	3.077725×10^5	-1.913290×10^5
p_3	4.559849×10^3	6.212530×10^3	3.881261×10^3
p_4	-46.335277	62.691313	-39.357670
p_5	0.235352	0.316260	0.199503
p_6	-4.780377×10^{-4}	6.380752×10^{-4}	-4.044113×10^{-4}
p_7	1.552182×10^5	3.590628×10^4	7.499228×10^4
p_8	-6.232793×10^3	1.433391×10^3	-3.013647×10^3
p_9	93.837832	21.446359	45.403181
p_{10}	-0.627791	0.142534	-0.303937
p_{11}	0.001574	3.550359×10^{-4}	7.627779×10^{-4}

5.3.2.1 Keysight free-space material characterization measurement setup

The dielectric properties of SUTs were additionally characterized using commercial Keysight 85071E material measurement software, which was regarded as the reference to the proposed method in this chapter. The measurement setup uses free-space transmission configuration, shown in Fig. 5.8. The SUTs are placed in the collimated beam between parabolic mirrors. Using 85071E software, the S-parameter network analyser data can be instantly converted into the complex permittivity and permeability of the SUTs.

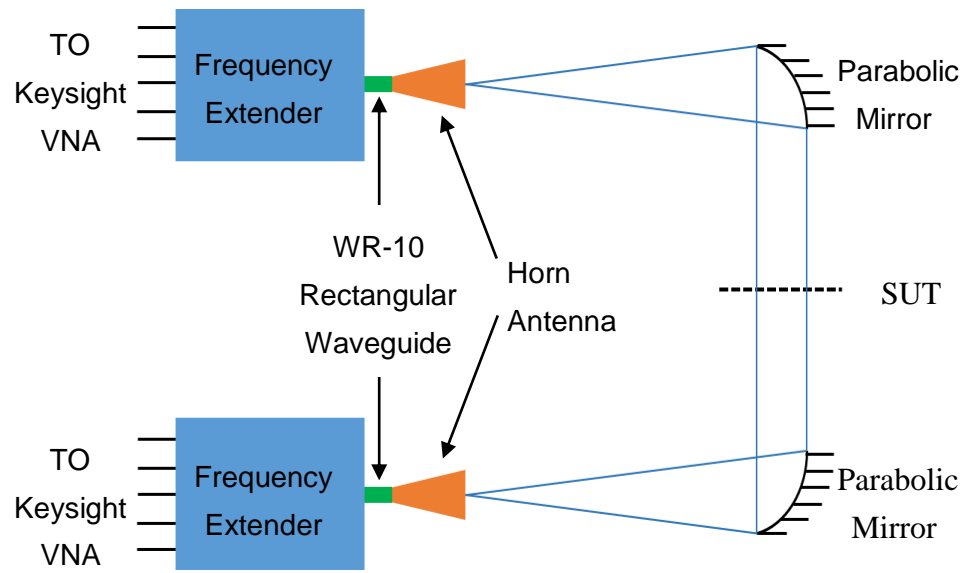


Figure 5.8 Keysight free space material characterisation setup

5.4 Measurement results

5.4.1 Resonant method results

The Through-Reflect-Line (TRL) calibration method was used prior to conducting measurement. When using the resonant method, the measurements were essentially one port measurements as a sliding short was inserted in the second port. The sliding short was held in place by a precision movement block to ensure that it was always in the same position. Fig. 5.9 shows the S-parameter response of the measurement of PTFE, PMMA, HDPE and air as the standard. Loading the CSRR sensor with a solid MUT causes the resonant frequency to shift downwards in frequency and the return loss to increase. The shift in frequency and S11 magnitude corresponds to the complex permittivity of the material under test. Much more shift in either measurement parameter is seen for a material with higher relative permittivity while a higher loss tangent corresponded with a higher insertion loss.

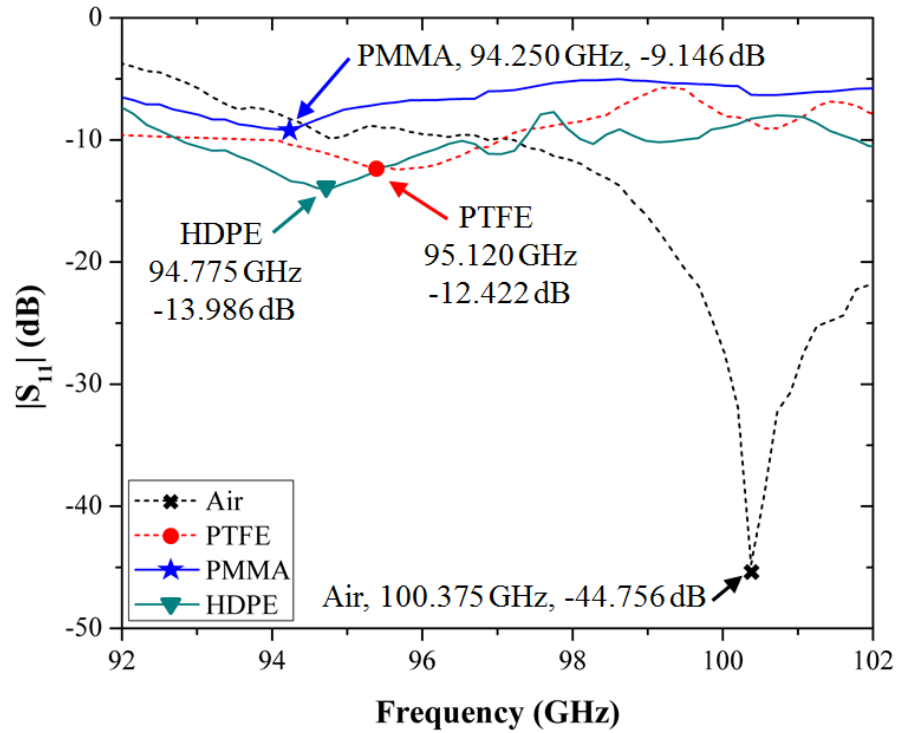


Figure 5.9 Measured and simulated S11 response for Air, PTFE, PMMA and HDPE samples.

Using the model developed in section 5.3.1, the permittivity of the materials under test were extracted as follows using only the measured data.

- (i) Measure the air standard and take note of the resonant frequency and s_{11} magnitude response.
- (ii) Measure the sample and calculate Δf_r and Δs_{11} from the measured resonant frequency and s_{11} magnitude for each sample in Fig. 5.7.

$$\Delta f_r = f_{r0} - f_{rs} \quad (5.9)$$

$$\Delta s_{11} = s_{11o} - s_{11s} \quad (5.10)$$

Where f_{r0} and f_{rs} are the resonant frequency when measuring air and the MUT respectively. Similarly s_{11o} and s_{11s} are the magnitude of the return measured signal for air and the sample at port 1 respectively.

- (iii) Using (5.9) and (5.10) calculate $\Delta\epsilon_r'$ and $\Delta\tan\delta$
- (iv) Finally find the relative permittivity of the material under test as $1 + \Delta\epsilon_r'$ and the loss tangent as $0 + \tan\delta$.

The four steps were done by a simple Matlab program. The extracted complex permittivity values are given in table 5.4 together with the values measured using the Keysight free space method only for the frequency points of interest.

Table 5.5 Complex permittivity results – Resonant method

<i>MUT</i>	<i>Freq</i> (GHz)	<i>S11</i> dB	<i>Resonant</i>	<i>Resonant</i>	<i>Free space</i>	<i>Free space</i>	<i>Difference</i>	
			<i>Method</i> (<i>this work</i>) ϵ_r'	<i>Method</i> (<i>this work</i>) $\tan\delta$	<i>measurement</i> (<i>Keysight free</i> <i>space</i>) ϵ_r'	<i>measurement</i> (<i>Keysight free</i> <i>space</i>) $\tan\delta$	$\frac{\Delta\epsilon_r'}{\epsilon_r'}$	$\frac{\Delta\tan\delta}{\tan\delta}$
PTFE	95.12	-12.422	2.124	0.00028	2.055	0.00029	0.032	0.035
PMMA	94.25	-9.146	2.652	0.006	2.6115	0.0062	0.015	0.033
HDPE	94.775	-13.986	2.32	0.000122	2.3675	0.000126	0.0204	0.0327

5.4.2 Resonance Technique-Tuning Capability

The tuning capability of the sensor was demonstrated by moving the sliding short to a new position optimized for optimal radiation. In the first instance given in section IV (a), the sliding short was inserted fully at 12.45 mm length from port 2. In this sub section however, the sliding short was inserted up to 10.78 mm from port 2 to obtain another maximum radiation point. Measurements for all previously measured materials were then done with results obtained as shown in Fig. 5.10.

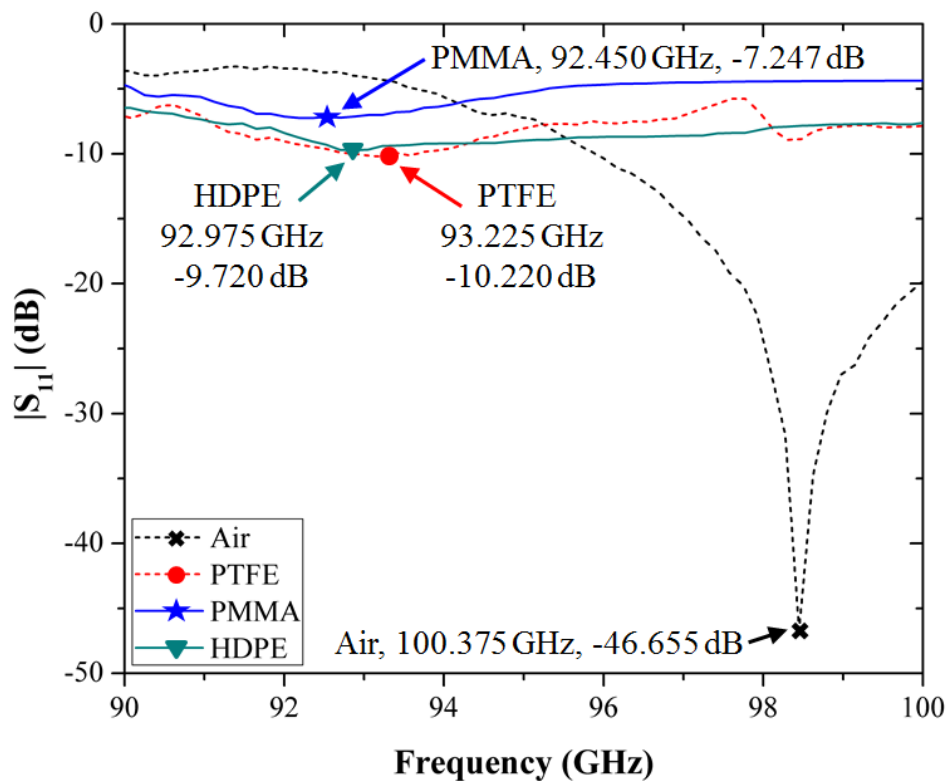


Figure 5.10 Measured S₁₁ with the sliding short inserted at 10.78 mm from port 2

Using the complex permittivity extraction developed in section 5.3.1, the material properties were extracted as shown in Table 5.5. The results in

Table 5.5 compared well with those obtained using the Keysight free space method, further validating the tuning functionality of the sensor.

Table 5.6 Complex permittivity with sliding short tuned at 10.78 mm from port 2

<i>MUT</i>	<i>Freq</i> (GHz)	<i>S11</i> (dB)	ϵ_r'	$\tan\delta$
PTFE	93.225	-10.22	2.116	0.00027
PMMA	92.45	-7.247	2.625	0.0059
HDPE	92.975	-9.72	2.31	0.000265

5.4.3 Transmission method results

The transmission method measurement setup is illustrated in Fig. 5.4. In Fig. 5.11 the measured S_{21} parameters for different solid materials together with the air measurement are shown. After repeated measurements, it was established that the meaningful bandwidth of measurement was about 5 GHz, from 97 GHz to 102 GHz.

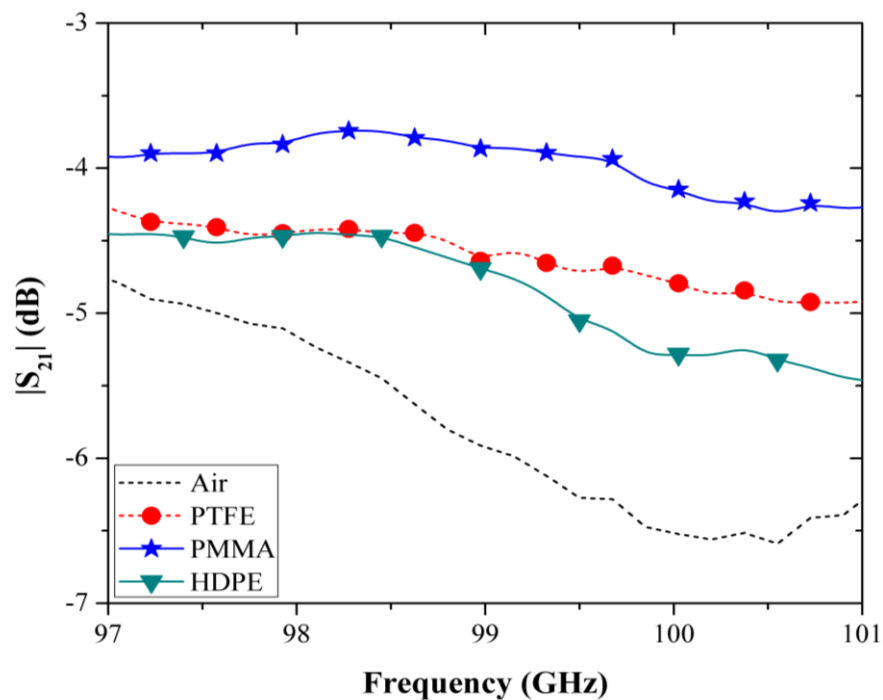


Figure 5.11 S_{21} plot for measured Air, PTFE and PMMA samples.

Using the relationship established in section 5.3.2, the relative permittivity of PTFE, and PMMA were extracted. These were compared with the results that were obtained when these materials were measured using the Keysight free space method as shown in Fig. 5.12:

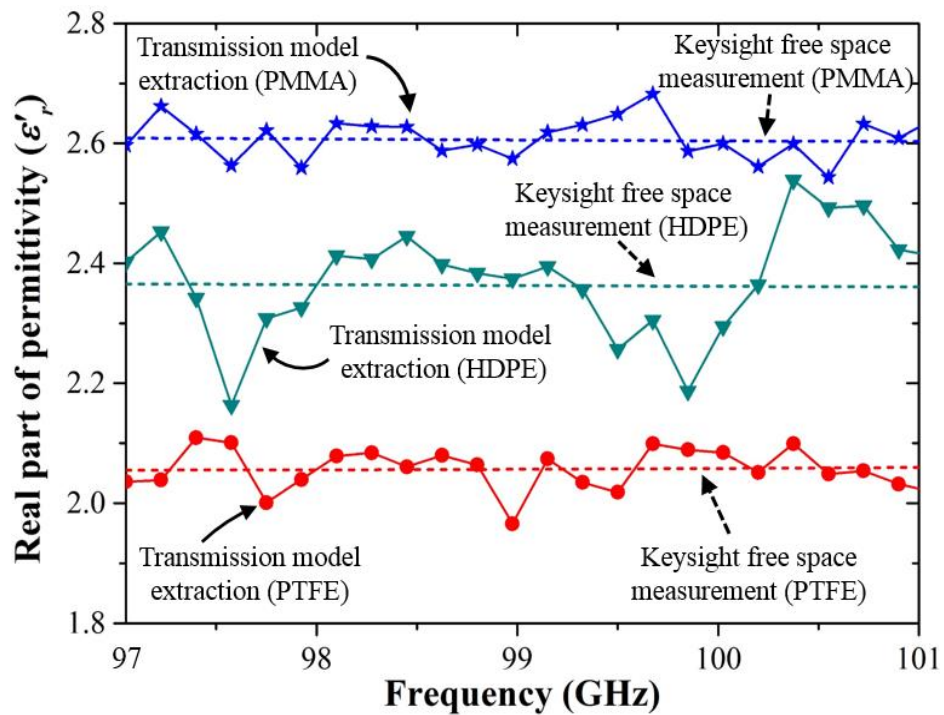


Figure 5.12 Transmission method extracted relative permittivity for PTFE and PMMA

The difference between the measurement of this work and that done using the Keysight free-space method is within the reported values for the substrate materials. The advantage of using the developed method is that it offers a faster characterisation alternative by using a small device, whereas the Keysight method requires the use of many components to setup in order to ensure that the signal is correctly aligned.

5.5 Summary

A multifunctional sensor was demonstrated in this chapter for the purposes of characterizing flat solid materials in the sub-terahertz region. Two major functions of the sensor were identified that serve two purposes: the resonant functionality gives highly accurate results at a single point, which quickly gives an indication of the properties of the SUT, while the transmission functionality gives measurement results at several frequency points, in turn giving a comprehensive broadband characterization of the SUT. Furthermore, the sensor offers the tuning functionality when operated in the resonant mode. By tuning the sliding short at port 2, the sensor is able to offer single resonant point properties of the SUT at a new measurement frequency. The developed sensor has potential in the characterization of thin film materials and especially the determination of thin film material thickness.

Chapter 6

Conclusion and Future Work

6.1 General summary

This research work has shown the importance of choosing an appropriate material characterisation method to achieve reliable results. By not using an appropriate method, the designer risks wasting considerable time and developing an unreliable device encumbered with inaccuracies.

For liquid mixture quantification, it was established that resonance methods are more appropriate when compared with transmission line alternatives. Apart from the high accuracy that resonance methods provide, the single point measurement makes quantification analysis more interpretable. Although in this work, the quantification was only done on liquid mixtures, similar analysis can be used on cell solutions and other biological solutions. The primary basis of the quantification is to obtain the characterisation profile of the pure quantity of the two major constituent elements being measured. The in-between variants of the two elements can then be added to the profile based on either the known volumes or quantities. The developed profile can be characterised by a mathematical expression for that mixture that can be used for any unknown mixture quantities to infer the constituent volumes or quantities as shown in Chapter 4. This work further reinforced the established understanding that transmission line methods are best suited for broadband characterisation of a material and for gathering general electrical properties of a material.

In Chapter 4 it was further shown that by choosing a substrate material with specific interesting properties, a microfluidic channel can be built cheaply without the need for extra tubing. The desired properties of such a substrate material are those that make the substrate not to be porous and reactive, and not to be contaminating. In this work the Rodgers Duroid 5880 was found to be such a substrate material. Using this material, a microfluidic channel housing up to $7 \mu\text{l}$ liquid volume was cut out and used. In making the microfluidic channel in this manner, it was necessary that another layer of the substrate material was used as an isolation layer. The isolation layer has the sole purpose of separating the microfluidic subsection from the microwave subsection. When looked at as a whole, the isolation layer together with the microfluidic channel, combines with the microwave subsection to form the permanent fixture. This forms the basis of establishing the air standard, as it is constant throughout all measurements.

A multifunctional sensor was later designed and fabricated as shown in Chapter 5. This dual sensor was able to work as a resonance sensor on one hand and as a transmission sensor on the other. To work as a resonant sensor, a sliding short was inserted on port 2 while by removing the sliding short the sensor worked as a transmission sensor. It was also shown that the sensor could equally work as a tuneable sensor by changing the position of the sliding short. This multifunctional feature enables the sensor to give general electrical properties over a broad range as well as specific properties at those resonant frequency points.

The work presented in both Chapter 4 and Chapter 5 resulted from the initial analysis done during the design of the In-SIW sensor that is illustrated in

Chapter 3. The In-SIW sensor worked well in simulation but showed how difficult characterisation of liquids gets when done using the propagating wave rather than the evanescent modes and near fields.

The overall achievement of this work is seen in the reduction of the required liquid volume (microlitre to nanolitre volume) to achieve accurate liquid characterisation. This was made possible by ensuring that sensing was done using the evanescent and near fields that do not propagate and can as a result measure very small liquid volumes.

6.2 Contributions

One key contribution of this work has been in the development of a microfluidic sensor using an SIW slot antenna that exploited the near fields perturbation by the measured liquid dielectric. The sensor offered several important advantages, such as offering uncomplicated fabrication (no clean room process required), being cheap, potentially re-usable with only the replacement of the microfluidic subsystem and only requiring $7 \mu\text{l}$ liquid volume.

Another key contribution of this work is in the design and development of a multifunctional sensor for sub-terahertz solid substrate material characterisation. This part of the work presented for the first time a sensor that integrated in one device the frequency-reconfigurable technique at 98 and 100 GHz and 97 – 101 GHz modified broadband transmission technique. The design built on the developed knowledge previously by using the near fields to characterise various materials. In this case, however split

ring resonators were employed. The developed sensor offered advantages such as offering multiple characterisation techniques in a single device, ease of design and fabrication and cost effectiveness.

6.3 Advantages of designs in this thesis

- The adopted methods were noninvasive and contactless. All methods did not require any alterations of the SUT or additional markers in the case of liquids.
- Adopted methods furthermore, offered effective measurements for both the microwave part and the mathematical analysis part.
- The developed methods demonstrated the characterisation of very small volume of liquids without requiring expensive microfluidic channels and not requiring the clean room environment.
- The work underlined how simple transmission lines can be exploited to develop interesting sensing devices cheaply.

6.4 Prospects for further research

There have been potentially two main ways of extending this research that have developed:

1. To consider practical characterisation and specifically quantification of biological mixtures using some of the developed devices in this work. These could in the initial stages be cell solutions that could come from the cell culture labs within the University. Some of the researchers currently doing cell culture experiments have the difficult of counting cells using visual viewing. Microwave methods as studied in this

research and similar other variants could come in handy in this regard. Most of the pointers for quantification have already been highlighted in Chapter 4 and are re-emphasised here as follows:

- Measure (to obtain either resonance frequency or relative permittivity) known volumes of both constituents on their own if possible. If not possible measure known mixture volumes.
- Measure known mixture volumes of the two constituent materials.
- From the first two steps establish the boundary of the characterisation.
- Using mathematical analysis create a relationship between the constituent materials and the measured quantity.
- Use the developed mathematical relationship to analyse any subsequent measurements that are done within the established operation bounds.

The major work however will be in establishing what form the sensor will be in for the measurements to adequately analyse the cell solution or whatever biological solution to be characterised.

2. To consider extending the development of sensing using evanescent modes from an antenna to between 220 – 300 GHz. Depending on how successful this will be, further extension can be considered. The design at this frequency will however need to consider the fabrication limitations of the workshop as the devices become reduced in size and hence making the resonator even much smaller in size.

List of Publications

- A Microfluidic-Integrated SIW Lab-on-Substrate Sensor for Microliter Liquid Characterization, *IEEE Sensors Journal*, vol. 16, no. 21, pp. 7628-7635, 2016.
- Microwave microlitre lab-on-substrate liquid characterisation based on SIW slot antenna, In *Microwave Conference (EuMC), 2016 46th European* (pp. 261-264) pp. 261-264
- Integrated Multi-Functional Instrument for Dielectric-Material Characterization at Millimeter-Wave and Sub-THz Frequencies. [Under review – IEEE Transaction on Instrumentation and Measurement].

List of References

- [1] J. Cho, J. Yoon, S. Cho *et al.*, "In-vivo measurements of the dielectric properties of breast carcinoma xenografted on nude mice," *International Journal of Cancer*, vol. 119, no. 3, pp. 593-598, 2006.
- [2] G. Facer, D. Notterman, and L. Sohn, "Dielectric spectroscopy for bioanalysis: From 40 Hz to 26.5 GHz in a microfabricated wave guide," *Applied Physics Letters*, vol. 78, no. 7, pp. 996-998, 2001.
- [3] L.-F. Chen, C. Ong, C. Neo *et al.*, *Microwave electronics: measurement and materials characterization*: John Wiley & Sons, 2004.
- [4] A. A. Note, "Agilent Basics of Measuring the Dielectric Properties of Materials," *Agilent Literature*, 2006.
- [5] N. Saber, Y. Ju, H.-Y. Hsu *et al.*, "A feasibility study on the application of microwaves for online biofilm monitoring in the pipelines," *International Journal of Pressure Vessels and Piping*, vol. 111, pp. 99-105, 2013.
- [6] D. Faktorová, A. Savin, and R. Grimberg, "Enhancement of waveguide sensor for biological tissues dielectric properties investigation with metamaterials." *Telecommunications and Signal Processing (TSP), 35th International Conference*, pp. 544-548 2012.
- [7] K. Grenier, D. Dubuc, M. Poupot *et al.*, "Microwave signatures of alive B-lymphoma cells suspensions." *IEEE Topical Conference on Biomedical Wireless Technologies, Networks, and Sensing Systems, 2011*, pp. 95-98.
- [8] A. R. von Hippel, and S. Morgan, "Dielectric materials and applications," *Journal of The Electrochemical Society*, vol. 102, no. 3, pp. 68C-68C, 1955.
- [9] J. Baker-Jarvis, R. G. Geyer, C. A. Grosvenor *et al.*, "Measuring the permittivity and permeability of lossy materials: Solids, liquids, metals, building materials, and negative-index materials," *Technical note 1536, NIST*, 2005.
- [10] M. A. Stuchly, and S. S. Stuchly, "Coaxial line reflection methods for measuring dielectric properties of biological substances at radio and microwave frequencies-A review," *IEEE Transactions on Instrumentation and Measurement*, vol. 29, no. 3, pp. 176-183, 1980.

- [11] R. Zajíček, and J. Vrba, *Broadband complex permittivity determination for biomedical applications: In Advanced Microwave Circuits and Systems. InTech*, 2010.
- [12] D. Berube, F. Ghannouchi, and P. Savard, "A comparative study of four open-ended coaxial probe models for permittivity measurements of lossy dielectric/biological materials at microwave frequencies," *IEEE Transactions on Microwave Theory and Techniques*, vol. 44, no. 10, pp. 1928-1934, 1996.
- [13] T. W. Athey, M. A. Stuchly, and S. S. Stuchly, "Measurement of radio frequency permittivity of biological tissues with an open-ended coaxial line: Part I," *IEEE Transactions on Microwave Theory and Techniques*, vol. 30, no. 1, pp. 82-86, 1982.
- [14] G. B. Gajda, and S. S. Stuchly, "Numerical analysis of open-ended coaxial lines," *IEEE Transactions on Microwave Theory and Techniques*, vol. 31, no. 5, pp. 380-384, 1983.
- [15] M. Brandy, S. Symons, and S. Stuchly, "Dielectric behavior of selected animal tissues in vitro at frequencies from 2 to 4 GHz," *IEEE Transactions on Biomedical Engineering*, no. 3, pp. 305-307, 1981.
- [16] J. Anderson, C. Sibbald, and S. Stuchly, "Dielectric measurements using a rational function model," *IEEE Transactions on Microwave Theory and Techniques*, vol. 42, no. 2, pp. 199-204, 1994.
- [17] F. M. Ghannouchi, and R. G. Bosisio, "Measurement of microwave permittivity using a six-port reflectometer with an open-ended coaxial line," *IEEE Transactions on Instrumentation and Measurement*, vol. 38, no. 2, pp. 505-508, 1989.
- [18] J. Baker-Jarvis, E. J. Vanzura, and W. A. Kissick, "Improved technique for determining complex permittivity with the transmission/reflection method," *IEEE Transactions on Microwave Theory and Techniques*, vol. 38, no. 8, pp. 1096-1103, 1990.
- [19] A. Nicolson, and G. Ross, "Measurement of the intrinsic properties of materials by time-domain techniques," *IEEE Transactions on Instrumentation and Measurement*, vol. 19, no. 4, pp. 377-382, 1970.
- [20] W. B. Weir, "Automatic measurement of complex dielectric constant and permeability at microwave frequencies," *Proceedings of the IEEE*, vol. 62, no. 1, pp. 33-36, 1974.

- [21] A.-H. Boughriet, C. Legrand, and A. Chapoton, "Noniterative stable transmission/reflection method for low-loss material complex permittivity determination," *IEEE Transactions on Microwave Theory and Techniques*, vol. 45, no. 1, pp. 52-57, 1997.
- [22] O. Ogunlade, R. D. Pollard, and I. C. Hunter, "A new method of obtaining the permittivity of liquids using in-waveguide technique," *IEEE Microwave and Wireless Components Letters*, vol. 16, no. 6, pp. 363-365, 2006.
- [23] J. Baker-Jarvis, M. D. Janezic, J. H. Grosvenor Jr *et al.*, "Transmission/reflection and short-circuit line methods for measuring permittivity and permeability," *NASA STI/Recon Technical Report N*, vol. 93, pp. 12084, 1992.
- [24] K. Saeed, R. D. Pollard, and I. C. Hunter, "Substrate integrated waveguide cavity resonators for complex permittivity characterization of materials," *IEEE Transactions on Microwave Theory and Techniques*, vol. 56, no. 10, pp. 2340-2347, 2008.
- [25] G. Gennarelli, S. Romeo, M. R. Scarfi *et al.*, "A microwave resonant sensor for concentration measurements of liquid solutions," *IEEE Sensors Journal*, vol. 13, no. 5, pp. 1857-1864, 2013.
- [26] T. Chretiennot, D. Dubuc, and K. Grenier, "A microwave and microfluidic planar resonator for efficient and accurate complex permittivity characterization of aqueous solutions," *IEEE Transactions on Microwave Theory and Techniques*, vol. 61, no. 2, pp. 972-978, 2013.
- [27] R. D. Hollinger, K. Jose, A. Tellakula *et al.*, "Microwave characterization of dielectric materials from 8 to 110 GHz using a free-space setup," *Microwave and Optical Technology Letters*, vol. 26, no. 2, pp. 100-105, 2000.
- [28] R. Clarke, A. Gregory, D. Cannell *et al.*, "A guide to the characterisation of dielectric materials at RF and microwave frequencies," *NPL Report*, 2003.
- [29] L. Jin, R. M. A. Lee, and I. Robertson, "Analysis and design of a novel low-loss hollow substrate integrated waveguide," *IEEE Transactions on Microwave Theory and Techniques*, vol. 62, no. 8, pp. 1616-1624, 2014.
- [30] M. N. Afsar, N. Suwanvisan, and Y. Wang, "Permittivity measurement of low and high loss liquids in the frequency range of 8 to 40 GHz using

waveguide transmission line technique," *Microwave and Optical Technology Letters*, vol. 48, no. 2, pp. 275-281, 2006.

[31] K. Grenier, D. Dubuc, P.-E. Poleni *et al.*, "Integrated broadband microwave and microfluidic sensor dedicated to bioengineering," *IEEE Transactions on Microwave Theory and Techniques*, vol. 57, no. 12, pp. 3246, 2009.

[32] S. Seo, T. Stintzing, I. Block *et al.*, "High frequency wideband permittivity measurements of biological substances using coplanar waveguides and application to cell suspensions." *IEEE MTT-S International Microwave Symposium Digest*, pp. 915-918, 2008.

[33] H. Ebara, T. Inoue, and O. Hashimoto, "Measurement method of complex permittivity and permeability for a powdered material using a waveguide in microwave band," *Science and Technology of Advanced Materials*, vol. 7, no. 1, pp. 77-83, 2006.

[34] K. Grenier, D. Dubuc, P.-E. Poleni *et al.*, "New broadband and contact less RF/microfluidic sensor dedicated to bioengineering." pp. 1329-1332.

[35] D. M. Pozar, "Microwave Engineering 3rd ed., MA John Wiley & Sons," Inc, 2005.

[36] L. Hogben, *Handbook of linear algebra*: CRC Press, 2006.

[37] K. Technologies, "Agilent 85070E Dielectric Probe Kit," July 2013.

[38] X. Cheng, D. Irimia, M. Dixon *et al.*, "A microfluidic device for practical label-free CD4+ T cell counting of HIV-infected subjects," *Lab on a Chip*, vol. 7, no. 2, pp. 170-178, 2007.

[39] E. Silavwe, N. Somjit, and I. D. Robertson, "A Microfluidic-Integrated SIW Lab-on-Substrate Sensor for Microliter Liquid Characterization," *IEEE Sensors Journal*, vol. 16, no. 21, pp. 7628-7635, 2016.

[40] E. Silavwe, N. Somjit, and I. D. Robertson, "Microwave microlitre lab-on-substrate liquid characterisation based on SIW slot antenna." *46th European Microwave Conference (EuMC)*, pp. 261-264, 2016.

[41] A. A. Abduljabar, X. Yang, D. A. Barrow *et al.*, "Modelling and measurements of the microwave dielectric properties of microspheres," *IEEE Transactions on Microwave Theory and Techniques*, vol. 63, no. 12, pp. 4492-4500, 2015.

[42] N. M. née Haase, G. Fuge, H. K. Trieu *et al.*, "Miniaturized Transmission-Line Sensor for Broadband Dielectric Characterization of

Biological Liquids and Cell Suspensions," *IEEE Transactions on Microwave Theory and Techniques*, vol. 63, no. 10, pp. 3026-3033, 2015.

[43] J. Leroy, C. Dalmay, A. Landoulsi *et al.*, "Microfluidic biosensors for microwave dielectric spectroscopy," *Sensors and Actuators A: Physical*, vol. 229, pp. 172-181, 2015.

[44] L. Y. Zhang, C. B. M. du Puch, C. Dalmay *et al.*, "Discrimination of colorectal cancer cell lines using microwave biosensors," *Sensors and Actuators A: Physical*, vol. 216, pp. 405-416, 2014.

[45] A. H. Sklavounos, and N. S. Barker, "Liquid-permittivity measurements using a rigorously modeled overmoded cavity resonator," *IEEE Transactions on Microwave Theory and Techniques*, vol. 62, no. 6, pp. 1363-1372, 2014.

[46] A. I. Gubin, A. A. Barannik, N. T. Cherpak *et al.*, "Whispering-gallery-mode resonator technique with microfluidic channel for permittivity measurement of liquids," *IEEE Transactions on Microwave Theory and Techniques*, vol. 63, no. 6, pp. 2003-2009, 2015.

[47] H. Lobato-Morales, A. Corona-Chavez, J. L. Olvera-Cervantes *et al.*, "Wireless sensing of complex dielectric permittivity of liquids based on the RFID," *IEEE Transactions on Microwave Theory and Techniques*, vol. 62, no. 9, pp. 2160-2167, 2014.

[48] H. Kawabata, H. Tanpo, and Y. Kobayashi, "A rigorous analysis of a TM₀₁₀ mode cylindrical cavity to measure accurate complex permittivity of liquid." 33rd European Microwave Conference, pp. 759-762, 2003.

[49] S. Liu, I. Ocket, D. Schreurs *et al.*, "A 60 GHz liquid sensing substrate integrated cavity in LTCC." pp. 613-615.

[50] S. Cheng, H. Yousef, and H. Kratz, "79 GHz slot antennas based on substrate integrated waveguides (SIW) in a flexible printed circuit board," *IEEE Transactions on Antennas and Propagation*, vol. 57, no. 1, pp. 64-71, 2009.

[51] M. Henry, C. Free, B. S. Izqueirido *et al.*, "Millimeter wave substrate integrated waveguide antennas: Design and fabrication analysis," *IEEE Transactions on Advanced Packaging*, vol. 32, no. 1, pp. 93-100, 2009.

[52] C. Liu, and F. Tong, "An SIW resonator sensor for liquid permittivity measurements at C band," *IEEE Microwave and Wireless Components Letters*, vol. 25, no. 11, pp. 751-753, 2015.

- [53] R. S. Elliot, *Antenna theory and design*: John Wiley & Sons, 2006.
- [54] D. Deslandes, and K. Wu, "Single-substrate integration technique of planar circuits and waveguide filters," *IEEE Transactions on Microwave Theory and Techniques*, vol. 51, no. 2, pp. 593-596, 2003.
- [55] S. Silver, "Microwave antenna theory and design," *Institution of Engineering and Technology; Reprint edition*, 1984.
- [56] R. C. Johnson, "Antenna engineering handbook," *Antenna engineering handbook/Richard C. Johnson, editor. 3rd ed. New York: McGraw-Hill*, 1993.
- [57] A. Farrall, and P. R. Young, "Integrated waveguide slot antennas," *Electronics Letters*, vol. 40, no. 16, pp. 1, 2004.
- [58] D. Deslandes, "Design equations for tapered microstrip-to-substrate integrated waveguide transitions." pp. 704-707.
- [59] P. B. Katehi, "Dielectric-covered waveguide longitudinal slots with finite wall thickness," *IEEE Transactions on Antennas and Propagation*, vol. 38, no. 7, pp. 1039-1045, 1990.
- [60] N. Amiri, and K. Forooghi, "Analysis of a dielectric-covered waveguide slot antenna using the spectrum of two-dimensional solutions," *IEEE Transactions on Antennas and Propagation*, vol. 62, no. 7, pp. 3818-3823, 2014.
- [61] L. Jylhä, and A. Sihvola, "Equation for the effective permittivity of particle-filled composites for material design applications," *Journal of Physics D: Applied Physics*, vol. 40, no. 16, pp. 4966, 2007.
- [62] U. C. Hasar, J. J. Barroso, Y. Kaya *et al.*, "Reference-plane invariant transmission-reflection method for measurement of constitutive parameters of liquid materials," *Sensors and Actuators A: Physical*, vol. 203, pp. 346-354, 2013.
- [63] U. C. Hasar, "A microwave method for noniterative constitutive parameters determination of thin low-loss or lossy materials," *IEEE Transactions on Microwave Theory and Techniques*, vol. 57, no. 6, pp. 1595-1601, 2009.
- [64] W. Ellison, "Permittivity of pure water, at standard atmospheric pressure, over the frequency range 0–25 THz and the temperature range 0–100 C," *Journal of Physical and Chemical Reference Data*, vol. 36, no. 1, pp. 1-18, 2007.

- [65] J. D. Baena, J. Bonache, F. Martin *et al.*, "Equivalent-circuit models for split-ring resonators and complementary split-ring resonators coupled to planar transmission lines," *IEEE Transactions on Microwave Theory and Techniques*, vol. 53, no. 4, pp. 1451-1461, 2005.
- [66] Y. Dong, and T. Itoh, "Metamaterial-based antennas," *Proceedings of the IEEE*, vol. 100, no. 7, pp. 2271-2285, 2012.
- [67] M. Gil, J. Bonache, J. Selga *et al.*, "Broadband resonant-type metamaterial transmission lines," *IEEE Microwave and Wireless Components Letters*, vol. 17, no. 2, pp. 97-99, 2007.
- [68] A. Daliri, W. S. Rowe, and K. Ghorbani, "Split-ring slot in the broad-wall of a rectangular waveguide," *IEEE Antennas and Wireless Propagation Letters*, vol. 13, pp. 991-994, 2014.
- [69] M. Mehdizadeh, T. K. Ishii, J. S. Hyde *et al.*, "Loop-gap resonator: A lumped mode microwave resonant structure," *IEEE Transactions on Microwave Theory and Techniques*, vol. 31, no. 12, pp. 1059-1064, 1983.
- [70] M. Gil, J. Bonache, and F. Martin, "Metamaterial filters: A review," *Metamaterials*, vol. 2, no. 4, pp. 186-197, 2008.
- [71] J. Bonache, I. Gil, J. Garcia-Garcia *et al.*, "Novel microstrip bandpass filters based on complementary split-ring resonators," *IEEE Transactions on Microwave Theory and Techniques*, vol. 54, no. 1, pp. 265-271, 2006.
- [72] M. Gil, J. Bonache, and F. Martin, "Synthesis and applications of new left handed microstrip lines with complementary split-ring resonators etched on the signal strip," *IET Microwaves, Antennas & Propagation*, vol. 2, no. 4, pp. 324-330, 2008.
- [73] D. J. Rowe, S. Al-Malki, A. A. Abduljabar *et al.*, "Improved split-ring resonator for microfluidic sensing," *IEEE Transactions on Microwave Theory and Techniques*, vol. 62, no. 3, pp. 689-699, 2014.
- [74] A. Masood, O. Castell, D. Barrow *et al.*, "Split ring resonator technique for compositional analysis of solvents in microcapillary systems." *In The Proceedings of MicroTAS Conference, San Diego*, pp. 1636-1638, 2008.
- [75] H.-J. Lee, H.-S. Lee, K.-H. Yoo *et al.*, "DNA sensing based on single element planar double split-ring resonator." *IEEE MTT-S International Microwave Symposium Digest*, pp. 1685-1688, 2009.

- [76] H.-J. Lee, J.-H. Lee, H.-S. Moon *et al.*, "A planar split-ring resonator-based microwave biosensor for label-free detection of biomolecules," *Sensors and Actuators B: Chemical*, vol. 169, pp. 26-31, 2012.
- [77] J. R. Stanec, and N. S. Barker, "A Rectangular-Waveguide Contacting Sliding Short for Terahertz Frequency Applications," *IEEE Transactions on Microwave Theory and Techniques*, vol. 61, no. 4, pp. 1488-1495, 2013.

Appendix A

Matlab codes used in the extraction of material permittivity using the In-SIW transmission line sensor of chapter 3

A.1 Main Matlab code for complex permittivity extraction

```

clc
clear

%This code simulates for the LTCC implementation with no air space
at the
%input and output

global lambdaZ lambdaC ds c n TraMs;

disp('Liquid Permittivity Determination using Transmission and
Reflection Method')
disp('User needs to create m-file s2p & s3p with simulated or
measured s-parameters at the Plug interface')
disp(' ')

Zint=120*pi;
flower=33.35e9;
fupper=50.35e9;
step=1e8;
f=flower:step:fupper;
fc=26.35e9;
c=3e8;
v=15.932; %Total volume of middle layer
v1=0.0527; %Fractional volume of protruding substrate part into the
liquid
v2=0.9473; %Fractional volume of the Liquid
e1=7.1-i*0.001; %permittivity of the substrate

% Total S-Parameters from the plug plane
S11T=m1p(11);
S12T=m1p(12);
S21T=m1p(21);
S22T=m1p(22);
% Plug S-Parameters
S11p=c3p(11);
S12p=c3p(12);
S21p=c3p(21);
S22p=c3p(22);
%Enter debye relationship values
es=input('enter estimated static dielectric constant of MUT:');
einf=input('enter estimated optical dielectric constant of MUT:');
tau=input('enter estimated relaxation time of MUT: ');

% Make initial estimate of permittivity at start frequency

```

```

er_old=[real(einf+(es-einf)/(1+i*2*pi*flower*tau)) -imag(einf+(es-
einf)/(1+i*2*pi*flower*tau))];

N=length(f);
for n=1:N;
    Factor=sqrt(1-(fc/f(n))^2);
    Zo=Zint/Factor;
    lambdaz=c./f(n);
    lambdac=11.38e-3;
    ds=1.0e-3;

    %Workings for de-embedding the sample holder plugs to get s-
parameters due to sample follow

    detTot(n)=(S11T(1,n)*S22T(1,n)-(S12T(1,n)*S21T(1,n)));
    %Determinant of the Line simulation
    detThru(n)=(S11p(1,n)*S22p(1,n)-
(S12p(1,n)*S21p(1,n)));%Determinant of the Through simulation

    %Calculate Trace of the product of line simulation and the
inverse of
    %the through simulation
    TraMs(n)=(S11T(1,n)*S22p(1,n)+(S11p(1,n)*S22T(1,n))-
detThru(n)-detTot(n))/(S21T(1,n)*S12p(1,n));

    options = optimoptions('fsolve','Display','iter'); % Option to
display output
    [er_new,fval] = fsolve(@myfunctnw,er_old,options); % Call solver
    er_old=er_new;
    eeff(n)=er_new(1,1)-j*er_new(1,2);

end
er=exp((log(eeff)-v1*log(e1))/v2);
er
plot(f,real(er),f,abs(imag(er)))
xlabel('Frequency(Hz)')
ylabel('Relative permittivity & Loss factor values')
legend('Relative permittivity','Loss factor')

```

A.1.1 Matlab function called by the code in A.1

```

function F = myfunctnw(er)
    %This function is called by Fsolve in permit_solverltcc
    % Global Variables Declaration
    global lambdaz lambdac ds c S21s n TraMs;

    gams=(j*2*pi/lambdaz)*sqrt(er(1,1)-j*er(1,2)-(lambdaz/lambdac).^2);
    %propagation constant in sample filled waveguide portion
    TraFl(n)=2*cosh(gams*ds);% Trace of the fluidic part

    %define iteration equations where TraMs is the trace of the product
of line
    %simulation and the inverse of the through simulation
    F=[real(TraMs(1,n)-TraFl(n));imag(TraMs(1,n)-TraFl(n))];
end

```

Appendix B

Matlab codes used for the extraction of relative permittivity for the liquid in chapter 4

B.1 Main matlab code for permittivity extraction

```

clc
clear

global Yw gs S11r Zod h lambdo no Zo fr ko Lres Yod kw Cs Ls omega;

disp('Liquid Permittivity Determination using Slot Antenna Sensor')
disp('User needs to input the resonant frequency, either measured or
simulated')
disp(' ')

fd=10e9;
esub=2.2-i*0.00198; %Complex permittivity of the guide substrate
Lres=11.7e-3; %Slot length
w=0.5e-3; %Slot width
Arg=22.86e-3; %Guide width of hollow rectangular guide
a=15.4e-3; %SIW width
t=0.0175e-3; %Conductor thickness
x=1.85e-3; %Slot displacement from guide centre line
b=1.575e-3; %Guide height
Zo=50; %characteristic impedance of microstrip line
no=120*pi; %Intrinsic impedance of free space
c=3e8;
h=0.79e-3;%slot cover height

uo=1.2566e-6;
eo=8.854e-12;
Cs=(uo*Lres*w)/t;%Equivalent capacitance for the slot cavity
Ls=(eo*t*w)/Lres;%Equivalent inductance for the slot cavity
v2=0.957;%volume fraction occupied by substrate in the sample holder
v1=0.043; %volume fraction occupied by liquid in the sample holder
fc=c/(2*Arg);

fr=input('enter measured or simulated resonant frequency in Hz with
decimal points:');
S11r=input('enter measured or simulated S11 at resonant
frequency:');

% Make initial estimate of liquid permittivity at start frequency
%Use the permittivity of the dielectric material encapsulating the
liquid
eff_old=[real(esub) -imag(esub)];

lambdo=3e8/fr;
lambdrg=lambdo/(sqrt(1-(lambdo/(2*Arg))^2));
lambdg=lambdrg/sqrt(2.2);
%lambdg=(2)/sqrt((2.2*(2*fr)^2/(3e8)^2)-(1/Arg)^2);

```

```

ko=2*pi/lambdo;
B10=sqrt((2.2*ko^2)-(pi/a)^2);%Propagation constant in the SIW
g1=((2.09*a*lambdg)/(b*lambdo))*((cos((lambdo*pi)/(2*lambdg)))^2);
gs=g1*((sin(x*pi/a))^2); %normalised resonant conductance of the
slot
omega=2*pi*fr;
Betad=sqrt((2.2*ko^2)-(pi/Lres)^2);%Propagation constant in the
dielectric
Yod=Betad/(ko*no);%characteristic admittance in the dielectric cover
%Yod=sqrt(2.2)/no;
kw=(2*pi*sqrt(2.2))/lambdo; %propagation constant in the guide
Yow=Yod;
Yw=-j*Yow*cot(kw*b); %Input admittance looking into the guide from
the slot position
k=2*pi*sqrt(2.2)/lambdo;
Zod=1/Yod;
options = optimoptions('fsolve','Display','iter','MaxFunEvals',
3000,'MaxIter',1000); % Option to display output
[eff_new,fval,EXITFLAG] = fsolve(@myfunctSl,eff_old,options);%
Call solver
eff=eff_new;
eff=eff_new(1,1)+i*eff_new(1,2);

%Now use the Maxwell Garnett formula to find the relative
permittivity of
%the liquid
p=[2*(v2-1) (2*eff)-esub-(2*v2*esub)+(v2*esub) (1-v2)*esub*eff];
eliq=roots(p);
eliq = eliq(eliq>0);
eliq=real(eliq)

```

B.1.1 Matlab function called by the code in B.1

```

function F = myfunctSl(eff)
% Global Variables Declaration
global Yw gs S11r Zod h lambdo Gr no Zo fr ko Lres ZoSIW Yd S11c
S11i S21i;

kod=2*pi*sqrt(2.2)/lambdo;
Betaliq=sqrt((eff(1)*ko^2)-(pi/Lres)^2);
Zoliq=ko*no/Betaliq;
%Zoliq=no/sqrt(eff(1));
kliq=2*pi*sqrt(eff(1))/lambdo;
Zeq=Zoliq*(Zod+(i*Zoliq*tan(kliq*h)))/(Zoliq+(i*Zod*tan(kliq*h)));
Zd=Zod*(Zeq+(i*Zod*tan(kod*h)))/(Zod+(i*Zeq*tan(kod*h)));
Yd=1/Zd;

lg=5.93e-2;%transmission feed line length
flower=8e9;
fupper=12e9;
step=1e7;
f=flower:step:fupper;

% S-Parameters from the mstrip
S11M=j2p(11);
S12M=j2p(12);
S21M=j2p(21);
S22M=j2p(22);
% S-Parameters from tapered line
S11T=j3p(11);

```

```

S12T=j3p(12);
S21T=j3p(21);
S22T=j3p(22);
% S-Parameters from SIW portion
S11S=j4p(11);
S12S=j4p(12);
S21S=j4p(21);
S22S=j4p(22);

N=length(f);
for n=1:N;
    Zo=50;

    %Start with converting microstrip s-parameters to ABCD
parameters
    Tm11(n)=(1+S11M(1,n))*(1-
S22M(1,n)+(S12M(1,n)*S21M(1,n))/(2*S21M(1,n)));
    Tm12(n)=Zo*((1+S11M(1,n))*(1+S22M(1,n))-
(S12M(1,n)*S21M(1,n)))/(2*S21M(1,n));
    Tm21(n)=((1-S11M(1,n))*(1-S22M(1,n))-
(S12M(1,n)*S21M(1,n)))/(2*Zo*S21M(1,n));
    Tm22(n)=(1-
S11M(1,n)*(1+S22M(1,n)+(S12M(1,n)*S21M(1,n)))/(2*S21M(1,n)));
    % Convert the tapered microstrip s-parameters to ABCD parameters
    Tt11(n)=(1+S11T(1,n))*(1-
S22T(1,n)+(S12T(1,n)*S21T(1,n)))/(2*S21T(1,n));
    Tt12(n)=Zo*((1+S11T(1,n))*(1+S22T(1,n))-
(S12T(1,n)*S21T(1,n)))/(2*S21T(1,n));
    Tt21(n)=((1-S11T(1,n))*(1-S22T(1,n))-
(S12T(1,n)*S21T(1,n)))/(2*Zo*S21T(1,n));
    Tt22(n)=(1-
S11T(1,n)*(1+S22T(1,n)+(S12T(1,n)*S21T(1,n)))/(2*S21T(1,n)));

    % Convert the SIW s-parameters to ABCD parameters
    Ts11(n)=(1+S11S(1,n))*(1-
S22S(1,n)+(S12S(1,n)*S21S(1,n)))/(2*S21S(1,n));
    Ts12(n)=Zo*((1+S11S(1,n))*(1+S22S(1,n))-
(S12S(1,n)*S21S(1,n)))/(2*S21S(1,n));
    Ts21(n)=((1-S11S(1,n))*(1-S22S(1,n))-
(S12S(1,n)*S21S(1,n)))/(2*Zo*S21S(1,n));
    Ts22(n)=(1-
S11S(1,n)*(1+S22S(1,n)+(S12S(1,n)*S21S(1,n)))/(2*S21S(1,n)));

    Tm=[Tm11(n) Tm12(n);Tm21(n) Tm22(n)];
    Tt=[Tt11(n) Tt12(n);Tt21(n) Tt22(n)];
    Ts=[Ts11(n) Ts12(n);Ts21(n) Ts22(n)];
    % Calculate ABCD parameters for the input and output of the feed
    % cascade
    Ti=Tm*Tt*Ts;
    % S11 and S21 Parameters for feed cascade

    S11i(n)=((Ti(1,1)+(Ti(1,2)./Zo)-(Ti(2,1).*Zo)-Ti(2,2))./...
(Ti(1,1)+(Ti(1,2)./Zo)+(Ti(2,1).*Zo)+Ti(2,2)));
    S12i(n)=2*((Ti(1,1)*Ti(2,2))-
(Ti(1,2)*Ti(2,1)))./(Ti(1,1)+(Ti(1,2)./Zo)+(Ti(2,1)*Zo)+Ti(2,2));
    S21i(n)=2/(Ti(1,1)+(Ti(1,2)./Zo)+(Ti(2,1)*Zo)+Ti(2,2));
    S22i(n)=(-Ti(1,1)+(Ti(1,2)./Zo)-(Ti(2,1).*Zo)+Ti(2,2))./...
(Ti(1,1)+(Ti(1,2)./Zo)+(Ti(2,1).*Zo)+Ti(2,2));

```

```

        ZoSIW(n)=Zo*(sqrt(((1+S11i(n))^2-(S21i(n))^2)/((1-S11i(n))^2-
(S21i(n))^2)));

end
y=((fr-flower)/1e7)+1;
ZoSIW(y);
GoSIW(y)=1/ZoSIW(y);
%GoSIW=1/ZoSIW;
Gs=gs*GoSIW(y);
Gr=Yd+Yw+Gs;
S11c=(-Gr/GoSIW(y))/(2+(Gr/GoSIW(y)));
F=[real(S11r-S11c);imag(S11r-S11c)];
end

```